

Design and implementation of a tool to simulate collision avoidance using aerodynamic drag for the Flying Laptop

Entwurf und Implementierung eines Tools zur Simulation der
Kollisionsvermeidung mittels aerodynamischen Widerstands für den
Flying Laptop

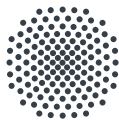
Master Thesis
cand. aer. Fabrizio Turco, B.Sc.
IRS-22-S-032

Responsible Professor:
Prof. Dr.-Ing. Sabine Klinkner

Supervisors:
Steffen Gaißer, M.Sc.
Constantin Traub, M.Sc.
Jonas Burgdorf, M.Sc.

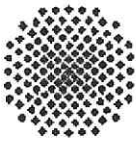


**Institut für
Raumfahrtsysteme**



Universität Stuttgart

Institute of Space Systems, University of Stuttgart



Master Thesis Work

of Mr. Fabrizio Turco

Entwurf und Implementierung eines Tools zur Simulation der Kollisionsvermeidung mittels
aerodynamischen Widerstands für den Flying Laptop

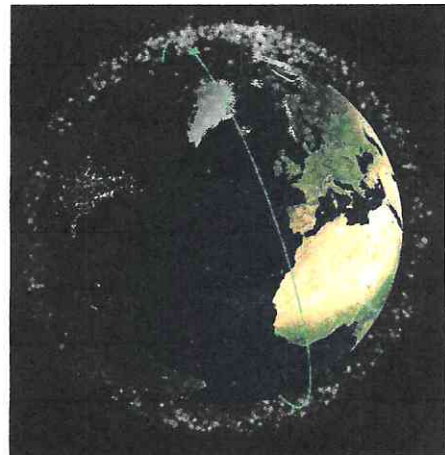
Design and implementation of a tool to simulate collision avoidance using aerodynamic drag for the
Flying Laptop

Motivation:

With the raising number of satellites launched into Low-Earth-Orbit, the number of close encounters of objects increases as well. Hence, the number of possible collisions is increasing accordingly. Today, for a small satellite in LEO this is equivalent to at least one warning per week.

The small satellite Flying Laptop of the University of Stuttgart is circling the earth in a 600 km orbit. Therefore, conjunction warnings are a reoccurring event. For a satellite without thrusters, the only option to increase the distance to another object is a change of its cross section facing in the orbit velocity direction. This changes its average ballistic coefficient. However, these changes are rather small but the impact on the orbital period can be enough to increase the distance at the closest encounter.

This Thesis should investigate methods to simulate the avoidance of collisions via aerodynamic drag. One method should be chosen and implemented in a tool. This tool should be able to predict which decision will result in the largest separation from the other object. The tool should be developed for the usage in nominal satellite operations. Therefore, it should be verified by comparing the data with experimental data from Flying Laptop gathered during the Thesis.



Task description of the Master thesis work:

- Literature research of different propagation methods for aerodynamic drag simulation
- Implementation of one method
- Verification of the implementation
- Integration of the tool in the nominal satellite operations
- Documentation

Supervisor: S.Gaisser, C. Traub, J. Burgdorf

Starting date: 04.04.2022

Submission until: 03.10.2022

Acknowledgement of receipt:

I hereby confirm that I read and understood the task of the master thesis, the juridical regulations as well as the study- and exam regulations.

20.4.22 S. Klinkner

Date

Prof. Dr.-Ing. Sabine Klinkner
(Responsible Professor)

11.04.2022 F. Turco

Date

Signature of the student

Legal Restrictions: The Editor/s is/are principally not entitled to make any work and research results which he/she receives in process, accessible to third parties without the permission of the supervisor. Already achieved research results respect the Law on Copyright and related rights (Federal Law Gazette I / S. 1273, Copyright Protection Act of 09.09.1965). The Editor has the right to publish his/her findings unless no findings and benefits of the supervising institutions and companies have been incorporated. The rules issued by the branch of study for making the bachelor thesis and the exam regulations must be considered.

IRS Professors and Associate Professors:

Prof. Dr.-Ing. Stefanos Fasoulas (Managing Director) · Prof. Dr.-Ing. Sabine Klinkner (Deputy Director) ·
Hon.-Prof. Dr.-Ing. Jens Eickhoff · Prof. Dr. rer. nat. Reinhold Ewald · PD Dr.-Ing. Georg Herdrich · Prof. Dr. rer. nat. Alfred Krabbe ·
Hon.-Prof. Dr. Volker Liebig · Hon.-Prof. Dr. rer. nat. Christoph Nöldeke · Prof. Dr.-Ing. Stefan Schlechtriem · PD Dr.-Ing. Ralf Srama

Declaration

I, **Fabrizio Turco**, hereby certify that I have written this **Master thesis** independently with the support of the supervisor, and I did not use any resources apart from those specified. The thesis, or substantial components of it, has not been submitted as part of graded course work at this or any other educational institution.

I also declare that during the preparation of this thesis I have followed the appropriate regulations regarding copyright for the use of external content, according to the rules of good scientific and academic practice¹. I have included unambiguous references for any external content (such as images, drawings, text passages etc.), and in cases for which approval is required for the use of this material, I have obtained the approval of the owner for the use of this content in my thesis. I am aware that I am responsible in the case of conscious negligence of these responsibilities.

Stuttgart, 30.09.2022

F. Turco

Place, Date, Signature

I hereby agree that my **Master thesis** with the following title:

Design and implementation of a tool to simulate collision avoidance using aerodynamic drag for the Flying Laptop

is archived and publicly available in the library of the Institute of Space Systems of the University of Stuttgart **without blocking period** and that the thesis is available on the website of the institute as well as in the online catalogue of the library of the University of Stuttgart. The latter means that bibliographic data of the thesis (title, author, year of publication, etc.) is permanently and worldwide available.

After finishing the work I will, for this purpose, deliver a further copy of the thesis along with the examination copy, as well as a digital version.

I transfer the proprietary of these additional copies to the University of Stuttgart. I concede that the thesis and the results generated within the scope of this work can be used free of cost and of temporal and geographical restrictions for the purpose of research and teaching to the Institute of Space Systems. If there exist utilisation right agreements related to the thesis from the institute or third parties, then these agreements also apply for the results developed in the scope of this thesis.

Stuttgart, 30.09.2022

F. Turco

Place, Date, Signature

¹Stated in the DfG recommendations for "Assurance of Good Scientific Practice" or in the statute of the University of Stuttgart for "Ensuring the Integrity of Scientific Practice and the Handling of Misconduct in Science".

Abstract

Collision avoidance is a topic of growing importance for any satellite orbiting Earth. Especially those without thrusting capabilities face the problem of not being able to perform impulsive evasive manoeuvres. For satellites in LEO, though, perturbing accelerations due to aerodynamic drag may be used to influence their trajectories, thus offering a possibility to avoid collisions as well. Within this thesis, this manoeuvring option is investigated for the satellite *Flying Laptop*, which was developed and is now operated by the Institute of Space Systems at the University of Stuttgart. In a first step, the satellite is aerodynamically analysed making use of the tool ADBSat. By employing an analytic equation, achievable in-track separation distances can then be derived following a variation of the ballistic coefficient through a change in attitude. Based on this, a tool is developed to assess potential manoeuvres in the face of a predicted close encounter. Considering additional constraints for the attitude, e.g., charging phases, the influence of a manoeuvre on the conjunction geometry and the collision probability is examined. The tool's predicted relative trajectory is further evaluated using numerical propagations and in-flight data. While an in-orbit verification still poses problems due to the lack of sufficient orbit determination capabilities, the tool is able to determine separation distances accurately and in close accordance to numerical propagations. A further examination of achievable separation distances proves the feasibility of aerodynamic collision avoidance manoeuvres for the *Flying Laptop* for moderate and high solar and geomagnetic activity.

Kurzfassung

Kollisionsvermeidung ist ein Thema von immer größerer Relevanz für sämtliche Satelliten im Erdorbit. Besonders solche ohne Fähigkeit zur Schuberzeugung stehen vor dem Problem, keine impulsiven Ausweichmanöver durchführen zu können. Für Satelliten in niedrigen Erdbits stellen Störbeschleunigungen durch aerodynamischen Widerstand allerdings eine Möglichkeit dar, ihre Trajektorie zu beeinflussen und damit auch Kollisionen zu vermeiden. In der vorliegenden Arbeit werden solche Manöver für den Satelliten *Flying Laptop* untersucht, der am Institut für Raumfahrtssysteme der Universität Stuttgart entwickelt wurde und von diesem betrieben wird. In einem ersten Schritt wird der Satellit mithilfe des Tools ADBSat aerodynamisch analysiert. Mittels einer analytischen Gleichung werden daraufhin erreichbare Separationsdistanzen durch eine Variation des ballistischen Koeffizienten infolge einer Lageänderung abgeleitet. Ausgehend davon wird ein Tool entwickelt, welches potenzielle Manöver angesichts einer vorhergesagten Annäherung mit einem anderen Objekt bewerten kann. Unter Berücksichtigung weiterer Randbedingungen, wie beispielsweise Ladephasen, wird der Einfluss eines Manövers auf die Konjunktionsgeometrie und die Kollisionswahrscheinlichkeit berechnet. Die vom Tool prädierten Trajektorien werden weiterhin mit numerischen Propagationen und Flugdaten verglichen. Während eine In-Orbit-Verifikation bislang noch ein Problem darstellt, da es an ausreichenden Möglichkeiten zur Orbitbestimmung mangelt, kann das Tool Separationsdistanzen in guter Übereinstimmung mit den numerischen Propagationsergebnissen bestimmen. Eine weitere Untersuchung der erreichbaren Separationsdistanzen zeigt, dass aerodynamische Ausweichmanöver für den *Flying Laptop* bei moderaten bis hohen solaren und geomagnetischen Aktivitätsniveaus sinnvoll realisierbar sind.

Contents

Nomenclature	1
1 Introduction	3
1.1 The <i>Flying Laptop</i> satellite	4
1.2 Scope of this thesis	6
1.3 Notational remarks	6
2 Fundamentals	7
2.1 Coordinate systems	7
2.2 Orbital elements and state vector	9
2.3 Satellite aerodynamics	10
2.3.1 Sentman model	12
2.4 Atmosphere modelling	14
3 Basics of collision avoidance	17
3.1 Conjunctions	17
3.1.1 Conjunction Data Messages	17
3.1.2 Calculation of the collision probability	18
3.2 State-of-the-art collision avoidance	20
3.3 Analytic estimation of achievable separation distance	21
3.4 Previous collision warnings for the <i>Flying Laptop</i>	24
4 Practical considerations	27
4.1 Operational constraints	27
4.2 Covariance realism	29
5 Aerodynamic analysis of the <i>Flying Laptop</i>	31
5.1 Model of the <i>Flying Laptop</i>	31
5.2 ADBSat analysis	32
5.2.1 Accommodation coefficient	32
5.2.2 Results	34
6 Simulation of collision avoidance manoeuvres using aerodynamic drag	37
6.1 The manoeuvre	37
6.2 The tool	38
6.3 Example: Conjunction from 2022/04/07	43

6.4	Verification	44
7	Analyses	47
7.1	Comparison with flight data	47
7.2	Achievable separation distance	49
7.3	Influence of parameter uncertainties	52
7.4	Influence of relative in-track position at TCA	54
8	Discussion	59
8.1	Feasibility	59
8.2	Uncertainties in parameters	61
8.3	Manoeuvre strategies	62
9	Summary and outlook	65
9.1	Summary	65
9.2	Outlook	66
A	Exemplary Conjunction Data Message	69
B	Aerodynamic analysis results of the <i>Flying Laptop</i> in nadir-pointing	71
C	Digital appendix	73
	Bibliography	75

Nomenclature

Latin Symbols

a	Semi-major axis	m
A_{ref}	Reference area	m ²
\mathbf{C}	Position covariance matrix	m ²
C_D	Aerodynamic drag coefficient	-
C_B	Ballistic coefficient	m ² kg ⁻¹
e	Eccentricity	-
h	Altitude	m
i	Inclination	rad
k^2	Covariance scaling factor	-
M	Mean anomaly	rad
m	Satellite mass	kg
n	Mean motion	rad s ⁻¹
\mathbf{a}_{aero}	Perturbing acceleration due to aerodynamic forces	m s ⁻²
P_c	Probability of collision	-
$P_{c,max}$	Maximum probability of collision	-
\mathbf{r}	Satellite position vector	m
Δr_{tca}	Miss distance	m
t	Time	s
t_c	Time to closest approach, manoeuvring time	s
\mathbf{v}	Satellite velocity vector	m s ⁻¹
\mathbf{v}_{rel}	Satellite velocity relative to local atmosphere	m s ⁻¹
\mathbf{x}	Satellite state vector	m, m s ⁻¹
Δx	Separation distance	m

Greek Symbols

α_T	Accommodation coefficient	-
φ	Angular difference in mean anomalies of two trajectories	rad

ρ	Total atmospheric mass density	kg m^{-3}
σ^2	Covariance	-
Ω	Right ascension of ascending node	rad
ω	Argument of perigee	rad

Constants

μ_E	Earth's gravitational parameter	$398\,600\,441.8 \text{ m}^3 \text{ s}^{-1}$
ω_E	Earth's rotational velocity	$7.292\,115 \times 10^{-5} \text{ rad s}^{-1}$
R_E	Earth's equatorial radius	$6\,378\,137 \text{ m}$

Acronyms

CAM	Collision avoidance manoeuvre
COESA-76	Standard atmosphere as published by the U.S. Committee on Extension to the Standard Atmosphere in 1976
DCP	Direct consider parameter
ECEF	Earth-centered Earth-fixed coordinate system
ECI	Earth-centered inertial coordinate system
FLP	Future Low-Cost Platform, sometimes also used for <i>Flying Laptop</i>
GSOC	German Space Operations Center
JB-2008	Jacchia-Bowman atmosphere model from 2008
JSpOC	Joint Space Operations Center
LEO	Low Earth orbit
LTAN	Local time of ascending node
NRLMSISE-00	(US) Naval Research Laboratory mass spectrometer incoherent scatter (radar) atmosphere model from 2000
PEDM	Piecewise exponential density model
RAAN	Right ascension of ascending node
SRP	Solar radiation pressure

1 Introduction

On October 4, 1957, the first ever man-made satellite, *Sputnik 1*, was launched into orbit marking the beginning of the Space Age. It remained in space for three months before eventually re-entering Earth’s atmosphere. Since then the number of satellites orbiting Earth has steadily increased. Interest in the various use-cases of satellites is growing, both commercial and scientific. Especially the regime of low Earth orbits (LEO), i.e., altitudes below 1000 km, offers great possibilities for Earth observation, thermospheric investigations and the market of global connectivity. This draws the attention of private actors as well and recently the growth of mega-constellations, like *Starlink* or *OneWeb* has led to a sharp rise in satellite numbers. While the object density in LEO grows, close encounters between objects in orbit happen ever more often. *Kessler* predicted the first in-orbit collision to happen between 1989 and 1997 [1]. And in fact, French satellite *Cerise* collided with a debris object in 1996 [2]. Until today, further collisions and tests of anti-satellite weapons have increased the amount of debris. Fig. 1.1 shows the evolution of total number of objects in orbit around Earth. Drastic increases in the LEO regime due to a Chinese anti-satellite test in 2007 and a collision between two functional *Cosmos* and *Iridium* satellites in 2009 are clearly visible [3, 4].

Growing numbers of satellites and debris do not only pose a threat to functional satellites. Every collision produces a huge amount of debris objects, which in turn threaten other satellites. Analyses have shown that this could eventually end in an avalanche-like process, rendering the LEO regime useless for future generations [1, 5, 6]. This highlights the need to minimise collision risk. Besides active debris removal, the best option for functional satellites is the implementation of collision avoidance manoeuvres in case of a predicted close encounter with another object. Typically, such manoeuvres are performed with impulsive thrusters to deflect the satellite trajectory. Satellites without thrusting capabilities need other strategies, though, to evade potential collisions. In LEO, aerodynamic drag and lift due to the remaining atmosphere represent significant natural perturbing forces. Using them to control and manoeuvre asymmetrically-shaped satellites has been widely researched. Although achievable accelerations are magnitudes smaller than what is possible with chemical thrusters, given enough time satellite orbits can be measurably altered. This allows for the implementation of collision avoidance manoeuvres, as well. Satellites without thrusters can, therefore, greatly benefit from collision avoidance manoeuvres using aerodynamic drag. The *Flying Laptop* is such a satellite and will be introduced in the next section.

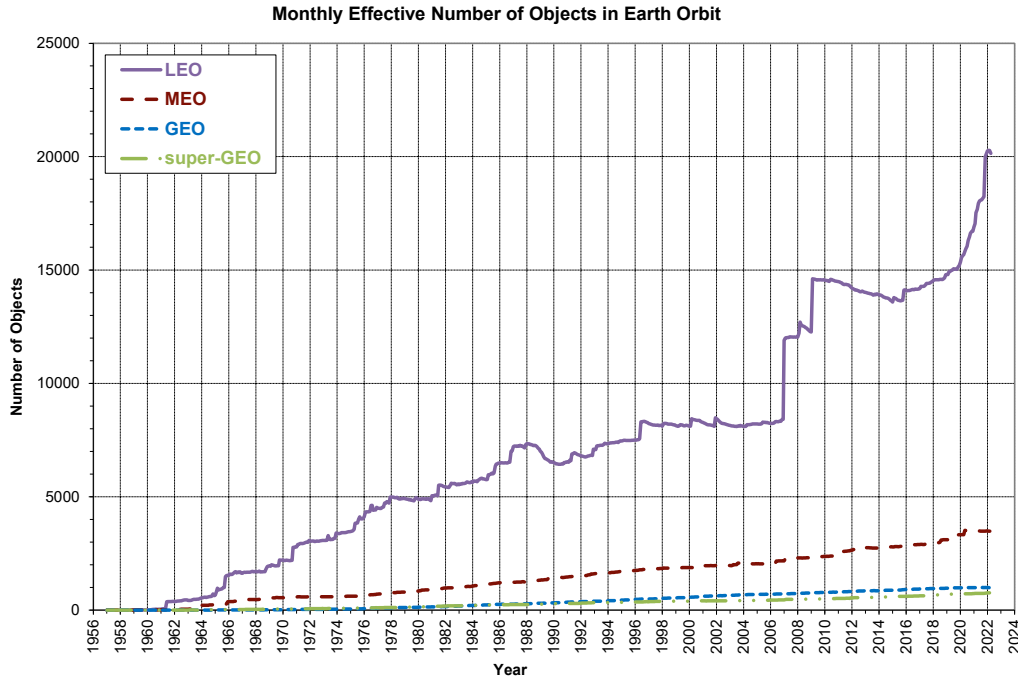


Figure 1.1 – Effective number of objects in orbit around Earth officially catalogued by the U.S. Space Surveillance Network [7].

1.1 The *Flying Laptop* satellite

The *Flying Laptop* is the first satellite of the small satellite program of the Institute of Space Systems (IRS) at the University of Stuttgart. It was designed, manufactured and is operated by the IRS in cooperation with partners from industry as the first prototype of the “Future Low-Cost Platform” (FLP). It has a volume of 0.357 m^3 in launch configuration (i.e., with contracted solar panels) and a mass of slightly more than 100 kg. It features GPS receivers, star trackers, magnetometers, gyros, and sun sensors for attitude determination and is 3-axes stabilised with magnetorquers and reaction wheels. The necessary power is generated by three solar panels, of which two are deployable [8, 9]. These can be seen in Fig. 1.2. On July 14, 2017, it was launched into a nearly circular polar orbit with an altitude of $\sim 600 \text{ km}$. Table 1.1 shows the orbit of the *Flying Laptop* as of April 1, 2022.

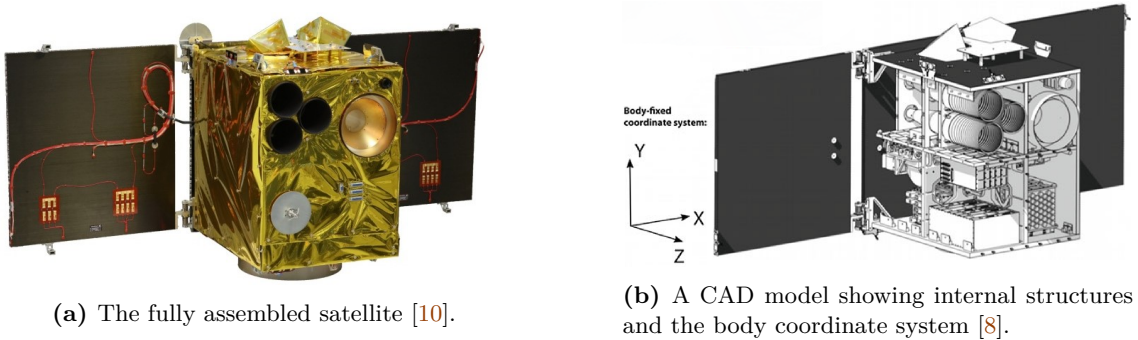


Figure 1.2 – The *Flying Laptop* satellite of the Institute of Space Systems, University of Stuttgart.

As a university satellite, the *Flying Laptop* is used primarily for teaching and research

Table 1.1 – The *Flying Laptop*’s orbit as of April 1, 2022 (mean elements from a TLE retrieved from space-track.org).

Semi-major axis	a	6971 km
Eccentricity	e	0.001 228
Inclination	i	97.43°
Right ascension of ascending node	Ω	310.2°
Argument of perigee	ω	266.0°

purposes. Further mission goals include technology demonstration and scientific Earth observation. The payloads are a multi-spectral imaging camera system (MICS), a panoramic camera (PAMCAM) and an AIS (automatic identification system) receiver for detection of signals transmitted by ships. An experimental optical communication link can further be established for research purposes [9, 10].

From its launch in 2017 until September 2022, the *Flying Laptop*’s operators received over 5000 warnings for over 150 close encounters from the Joint Space Operations Center (JSpOC). The highest probability of collision yielded $7.076 \times 10^{-1} \%$ and the lowest miss distance was predicted to be 29 m. Since the *Flying Laptop* does not possess any thrusters, it has no possibility for performing impulsive collision avoidance manoeuvres. Thus, the operators had to remain actionless so far upon reception of a collision warning. As previously pointed out, though, the orbital altitude and the asymmetric shape of the satellite, in principle, allow a control via aerodynamic drag. How this could be used for avoiding collisions will be investigated in this work.

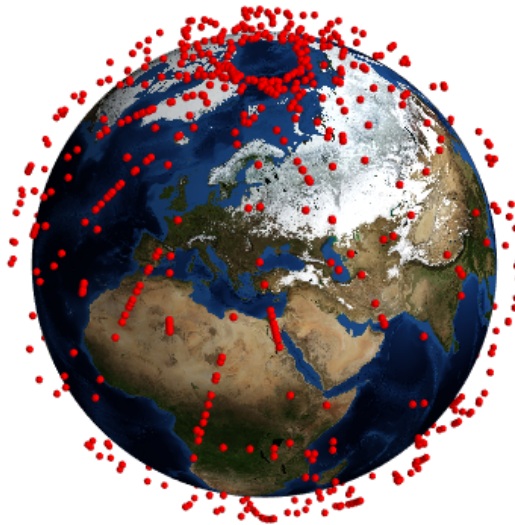


Figure 1.3 – Conjunction warnings for the *Flying Laptop* from launch until September 2022, as issued by the JSpOC.

1.2 Scope of this thesis

This thesis deals with collision avoidance manoeuvres involving aerodynamic drag for the university satellite *Flying Laptop* in practice. Its goal is the development of a tool to simulate collision avoidance manoeuvres. To achieve this, the satellite is aerodynamically studied and an analytic equation is utilised to calculate the effect of changes in the ballistic coefficient on the trajectory. In the context of a predicted close encounter, this allows for the estimation of achievable increases in the miss distance and the determination of associated collision probabilities.

In the first chapter of this work, the fundamental concepts and theories are introduced. After that, Chapter 3 covers basics of collision avoidance assessment and the state-of-the-art manoeuvres before dealing with avoidance manoeuvres involving aerodynamic drag. Further, previous collision warnings received for the *Flying Laptop* are reviewed. Chapter 4 covers challenges when applying collision avoidance using aerodynamic drag in practice. In Chapter 5, the aerodynamic properties of the *Flying Laptop* are examined before the developed tool is presented and verified in Chapter 6. Further analyses with the tool and flight tests are evaluated in Chapter 7 and the obtained results are then discussed in Chapter 8. Lastly, the work is summarised and future research topics are pointed out in Chapter 9.

1.3 Notational remarks

Throughout this thesis, vectors and matrices will be written in bold. Vector norms, like any scalar, will be written in italic. Time derivatives are marked with a dot over the respective variable. Regarding close encounters between objects in space, the term “time of closest approach” (TCA) is often used. To differentiate, TCA refers to an actual point in time (most often given in UTC) here, while t_c denotes a time to closest approach, i.e., a duration measured from a specified point in time until TCA, and is thus used as a potential manoeuvring time.

2 Fundamentals

The following chapter introduces the fundamental concepts and models used in this work. Coordinate systems will be defined as well as the relevant variables to describe satellite motion in space. A brief introduction in satellite aerodynamics lays the foundation for the determination of satellite drag and ballistic coefficients. Finally, different methods to estimate atmospheric densities are presented.

2.1 Coordinate systems

To describe the positions of satellites and other objects orbiting Earth, different coordinate systems can be utilised. All coordinate systems covered here have in common that they are orthonormal and right-handed systems.

Earth-centred inertial system (ECI)

A geocentric equatorial coordinate system has its origin in the centre of Earth. The principal direction, i.e., the direction of the first axis, is the direction of vernal equinox (cf. Fig. 2.1). The second axis points towards the North Pole and the third axis complements the right-handed system lying in the equatorial plane. Differential equations for satellite motion can be solved within this inertial frame.

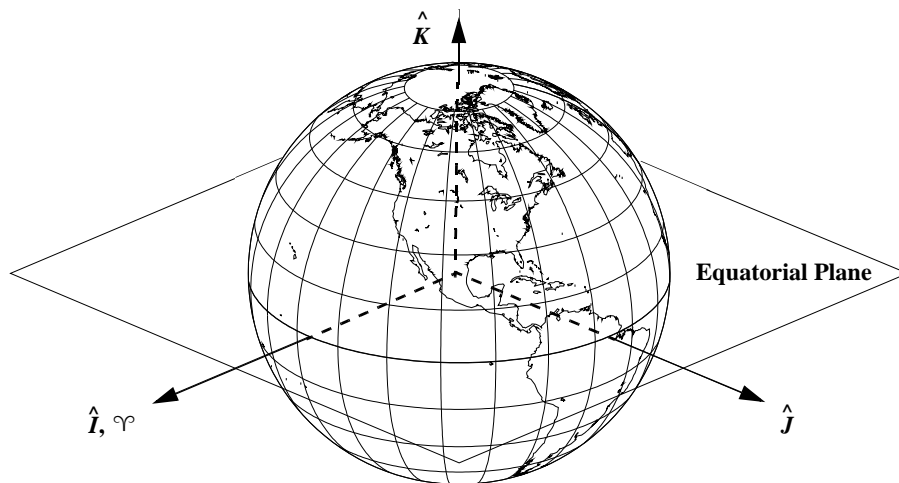


Figure 2.1 – The ECI coordinate system with its axes pointing towards vernal equinox (\hat{I}), 90° east to that in the equatorial plane (\hat{J}) and through the North Pole (\hat{K}) [11].

Earth-centred Earth-fixed system (ECEF)

While also originating from Earth's centre, the Earth-centred Earth-fixed (ECEF) rotates with the Earth, thus not being an inertial system. One such system is the *International Terrestrial Reference Frame* (ITRF). Its first axis points towards 0° longitude, while the second and third axes point towards 90° longitude and towards the North Pole, respectively [11]. In this work, the (ITRF) is used for representing ECEF positions in cartesian coordinates. The system's rotation with respect to the inertial space may be represented as a vector of angular velocity [12, 13]:

$$\boldsymbol{\omega}_E = \begin{pmatrix} 0 \\ 0 \\ 7.292\,115 \times 10^{-5} \text{ rad s}^{-1} \end{pmatrix} \quad (2.1)$$

The *World Geodetic System 1984* (WGS-84) is another ECEF system defined through GPS positions of several points on Earth's surface. Its axes are in close alignment with the ITRF. Further, the WGS-84 also includes a reference ellipsoid approximating the Earth's shape [14]. The system is used for calculating a satellite's altitude above the ellipsoidal Earth.

Local-vertical local-horizontal system

The local-vertical local-horizontal system (LVLH or RTN) is satellite-centered, i.e., its origin is fixed in the satellite's center of mass. The RTN system's first axis (R) is parallel the satellite's position vector pointing away from the Earth. The second axis (T) lies within the orbital plane and points along the direction of flight but is orthogonal to the first axis (transverse direction). Finally, the N axis is normal to the orbital plane and complements the right-handed system (cf. Fig. 2.2) [11, 15]. This system is sometimes also referred to as RSW system. Furthermore, the RTN system is not to be confused with the *Frenet system* (or NTW). This is defined similar but with the second axis pointing parallel to the satellite's velocity vector and the first axis normal to that in the orbital plane and pointing away from Earth. At apoapsis, periapsis, or for a circular orbit, the two systems coincide [15].

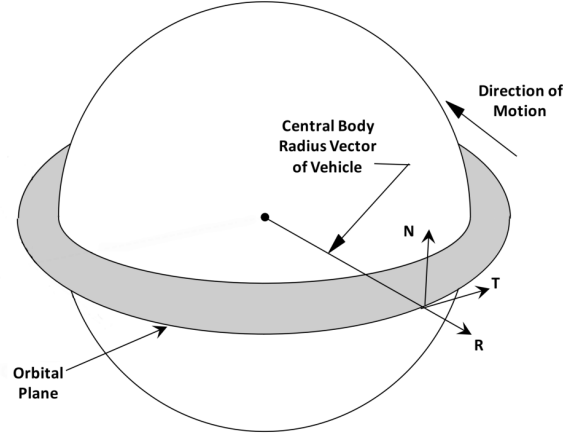


Figure 2.2 – The RTN coordinate system (adapted from [15]).

2.2 Orbital elements and state vector

The position \mathbf{r} and velocity \mathbf{v} of a satellite in a given coordinate system can be combined into what is referred to as the state vector \mathbf{x} [11]:

$$\mathbf{x} = \begin{pmatrix} \mathbf{r} \\ \mathbf{v} \end{pmatrix} \quad (2.2)$$

$$\text{with: } \mathbf{r} = \begin{pmatrix} r_1 & r_2 & r_3 \end{pmatrix}^T, \mathbf{v} = \begin{pmatrix} v_1 & v_2 & v_3 \end{pmatrix}^T \quad (2.3)$$

Here, r_1, r_2, r_3 and v_1, v_2, v_3 denote the position and velocity components into the directions of the underlying coordinate system's base vectors. Equally, six other variables are sufficient to describe a Keplerian orbit, i.e., an orbit in the two-body problem. The Keplerian elements are a set of six parameters and presented in Fig. 2.3: The semi-major axis a and the eccentricity e describe the size and shape of the orbit. The inclination i , the right ascension of the ascending node (RAAN) Ω and the argument of perigee ω identify the orientation of the orbit in space. The sixth parameter is needed to further specify the satellite's position on its orbit. The true anomaly ν defines the satellite's position as an angle measured from perigee, whereas the mean anomaly M is set as the ratio between the time that has passed since the body was last in perigee and the orbital period, expressed as an angle.¹ When a given position and velocity are converted into Keplerian elements, the elements define a Keplerian orbit with the exact position and velocity at that point in time neglecting any potential perturbations on the real orbit and are referred to as osculating elements. [11, 16]

In space object catalogues, satellite orbits are often described by so-called Two-Line Elements (TLEs). TLEs are a data format for exchange of orbital parameters, as shown in Table 2.1. The parameters are obtained from an orbit determination employing the

¹To be precise, the true and mean anomaly are not defined for circular orbits just like RAAN is not defined for equatorial orbits. For these cases, substitute parameters can be derived.

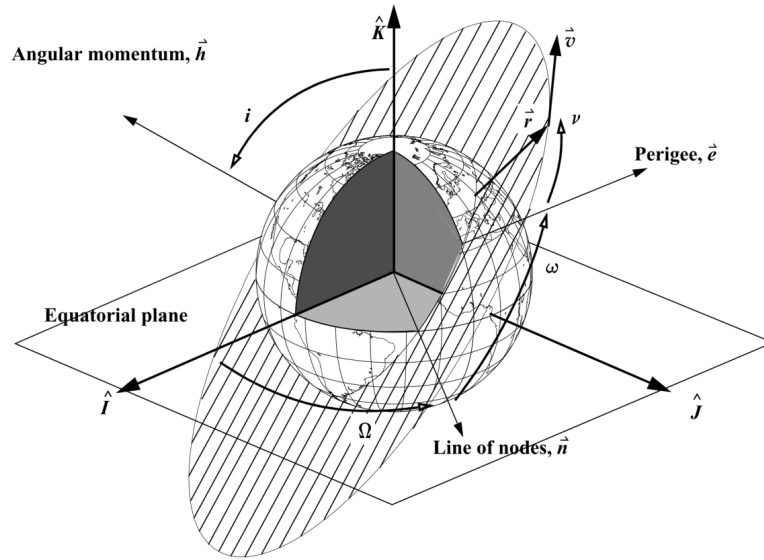


Figure 2.3 – Visualisation of the Keplerian elements [11].

simplified general perturbation theory 4 (sgp4) and are meant to be used for propagation within this theory. They are, therefore, fitted Keplerian elements and not to be confused with osculating Keplerian elements [17]. TLEs for several satellites are publicly available, e.g., at space-track.org/.

Table 2.1 – Parameters included in a Two-Line Element (TLE).

Line 1	Line 2
Satellite number and class	Satellite number
International designator	Inclination i
Epoch	RAAN Ω
First derivative of mean motion \dot{n}	Eccentricity e
Second derivative of mean motion \ddot{n}	Argument of perigee ω
Drag term B^*	Mean anomaly M
Element number	Mean motion n
	Revolution number

2.3 Satellite aerodynamics

Although the total density of the atmosphere decreases exponentially with height, satellites in LEO are still subject to a measurable perturbing acceleration due to the remaining particles. These effects are reinforced by the high velocities at which satellites orbit Earth [18]. Superimposed on the satellite velocity is the local velocity of the atmosphere. The velocity of a satellite relative to the local atmosphere is referred to as \mathbf{v}_{rel} . With the

rotational velocity of the Earth $\boldsymbol{\omega}_E$ and an additional wind velocity \boldsymbol{v}_{wind} , the relative velocity is [18]

$$\boldsymbol{v}_{rel} = \boldsymbol{v} - (\boldsymbol{\omega}_E \times \boldsymbol{r}) - \boldsymbol{v}_{wind} \quad (2.4)$$

Similarly to aircraft aerodynamics, the aerodynamic forces acting on a satellite can be separated into a lift acceleration \boldsymbol{a}_L and a drag acceleration \boldsymbol{a}_D (cf. Fig. 2.4):

$$\boldsymbol{a}_A = \boldsymbol{a}_L + \boldsymbol{a}_D \quad (2.5)$$

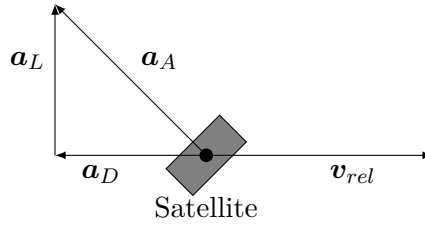


Figure 2.4 – The aerodynamic acceleration \boldsymbol{a}_A of a satellite is separated into a lift component \boldsymbol{a}_L and a drag component \boldsymbol{a}_D .

Drag is defined as the aerodynamic force component acting anti-parallel to the relative velocity vector, whereas lift acts in perpendicular direction to that. The acceleration due to aerodynamic drag depends on the satellite's dimensionless aerodynamic drag coefficient C_D , the reference area A_{ref} , the satellite mass m , the atmospheric density ρ and the satellite's velocity relative to the local atmosphere \boldsymbol{v}_{rel} :

$$\boldsymbol{a}_D = -\frac{1}{2}\rho C_D \frac{A_{ref}}{m} v_{rel}^2 \frac{\boldsymbol{v}_{rel}}{v_{rel}} \quad (2.6)$$

The choice of reference area is rather arbitrary, it can be any area as long as the drag coefficient is scaled accordingly. In this thesis, the projected satellite area in the direction of flight is chosen as reference area (effective cross-section). The ballistic coefficient C_B is a dimensional coefficient measuring to which extent a satellite is affected by aerodynamic drag. Satellites with high ballistic coefficients experience higher drag accelerations than such with low ballistic coefficients. It is defined as² [18]

$$C_B = \frac{C_D A_{ref}}{m} \quad (2.7)$$

In Eq. (2.6), most parameters are fixed. Atmospheric density and winds are given by nature, the satellite velocity is depending on its orbit and the satellite mass is constant (except for potential losses due to thrusters for some satellites). If a satellite is, however, asymmetrically shaped, control authority lies in the variation of the ballistic coefficient. By changing its attitude and thereby changing the effective cross-section, the experienced drag acceleration can be regulated.

Lift coefficients are usually considerably smaller than the respective drag coefficients. Al-

²It is to note, that the ballistic coefficient is sometimes defined inversely.

though aerodynamic lift can be used for satellite control under the right conditions [19, 20, 21], perturbing accelerations due to lift are not further pursued here.

2.3.1 Sentman model

For an aircraft, the surrounding air through which it moves can be considered a continuum. The density is so high that particles will collide with each other very often. In low Earth orbits (LEOs), the residual atmosphere is so thin, however, that a particle can move freely for a while until colliding with another. The mean way a particle travels between two collisions is called the mean free path λ . For a given characteristic scale length L , the *Knudsen* number can be defined as:

$$Kn = \frac{\lambda}{L} \quad (2.8)$$

Conditions in LEO typically lead to Knudsen numbers $Kn > 10$. This regime is called free-molecular flow. Aerodynamic interactions are here driven by collisions between the atmospheric particles and the spacecraft, as collisions between particles are rare. Complex phenomena take place during the interaction of the particles with the satellite's surface. To describe them, several gas-surface interaction models have been developed [22]. Most widely used for drag estimations at comparatively low altitudes is the Sentman model [23, 24, 25]. This model will also be used during this work and will, hence, be introduced.

When a particle hits the satellite's surface, its reflection can happen in two extreme ways depending on the interactions: Either, it can be rejected under the same angle as it hit the surface, which is called specular reflection - very much like light is reflected by a mirror. Or it can be re-emitted independently from its incident angle during the other extreme case of diffuse reflection. The direction and velocity of the rejection is distributed in a probabilistic way depending on the wall temperature (cf. Fig. 2.5).

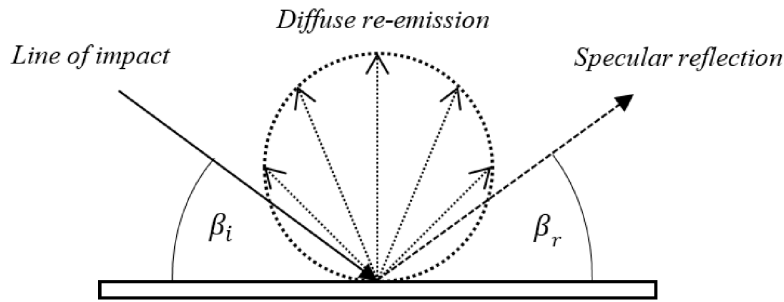


Figure 2.5 – Specular reflection vs. diffuse re-emission [19]. The angle of incidence is β_i , the angle of reflection is β_r .

Further, the Sentman model makes use of an accommodation coefficient α_T to describe energy transfer from particles to the wall:

$$\alpha_T = \frac{E_i - E_r}{E_i - E_w} = \frac{T_{k,i} - T_{k,r}}{T_{k,i} - T_w} \quad (2.9)$$

It is defined as the quotient of the differences in energy between the incoming particles E_i and reflected particles E_R and between the incoming particles and the wall E_w . This can be equally described by a quotient of temperature differences. *Sentman* further defined momentum accommodation coefficients. They specify the ratio of the difference in momentum between the incoming (“i”) and reflected particles (“i”) and between the incoming particles and the wall (“i”)³. They are defined for tangential momentum τ and normal momentum p :

$$\sigma_t = \frac{\tau_i - \tau_r}{\tau_i - \tau_w} = \frac{\tau_i - \tau_r}{\tau_i} \quad (2.10)$$

$$\sigma_n = \frac{p_i - p_r}{p_i - p_w} \quad (2.11)$$

Following the previous explanations, for specular reflection without thermal accommodation $\sigma_t = \sigma_n = 0$. In case of completely diffuse reflection and full thermal accommodation, the particles reach thermal equilibrium with the surface and $\sigma_t = \sigma_n = 1$. The *Sentman* model assumes diffuse reflection and a variable thermal accommodation coefficient [19]. Therefore, $\sigma_t = 1$ and σ_n depends on the degree of thermal accommodation.

Taking into account the thermal motion of the particles as well as the angle of incidence, the wall temperature and the temperature of the incoming particles, the *Sentman* model allows the calculation of a drag and lift coefficient for a surface in free molecular flow. For a flat plate of area A with one side exposed to the flow, the drag coefficient is given by [24, 25]

$$C_D = \left[\frac{P}{\sqrt{\pi}} + \gamma Q Z + \frac{\gamma}{2} \frac{v_r}{v_i} (\gamma \sqrt{\pi} Z + P) \right] \frac{A}{A_{ref}} \quad (2.12)$$

$$\text{with: } \gamma = \cos(\theta), \quad P = \frac{1}{s_\infty} \exp(-\gamma^2 s_\infty^2), \quad Q = 1 + \frac{1}{2s_\infty^2},$$

$$Z = 1 + \operatorname{erf}(\gamma s_\infty), \quad \operatorname{erf}(x) = \frac{2}{\sqrt{\pi}} \int_0^x \exp(-y^2) dy$$

Here, θ is the angle between the flow direction and the surface normal vector and s_∞ is the molecular speed ratio between the macroscopic gas velocity and the most probable thermal velocity of the molecules (following a *Maxwell-Boltzmann* distribution). The accommodation coefficient influences the ratio of the most probable velocity of the reflected particles and the incident velocity $\frac{v_r}{v_i}$ [24]:

$$\frac{v_r}{v_i} = \sqrt{\frac{2}{3} \left[1 + \alpha_E \left(\frac{T_w}{T_i} - 1 \right) \right]} \quad (2.13)$$

with the wall temperature T_w and the temperature of the incident particles T_i . The model has been implemented in the ADBSat tool developed by *Sinpetru, Crisp* et al., which calculates a satellite’s drag coefficient using a CAD model as input. The satellite geometry is divided into different panels, i.e., flat plates, and the drag coefficient is evaluated for each of them. The individual panels’ contributions are added to form the total drag coefficient,

³Per definition of diffuse reflection $\tau_w = 0$ [25].

considering potential shading of some panels [23, 26].

2.4 Atmosphere modelling

The Earth's atmosphere is a highly complex environment. For space applications, the atmospheric density, its temperature and its chemical composition at certain points are of interest to accurately model the aerodynamic forces on a satellite. Several atmospheric models are available for different applications. Static models are independent of time, examples are the piecewise exponential density model (PEDM) [11] or the standard atmosphere of the *U.S. Committee on Extension to the Standard Atmosphere* (COESA) [27]. Both provide atmospheric parameters in tabular form depending on altitude. The more complex time-varying models do consider time-dependent variations. Such variations in atmospheric density are caused by several mechanisms. Temperature differences between the day and the night side result in diurnal variations. There are also seasonal variations caused by the tilted rotational axis of the Earth. Semi-annual variations have their maxima around the solstices. On top of that, the solar and geomagnetic activity influence atmospheric density significantly [18].

The *US Naval Research Laboratory* (NRL) developed an empirical atmosphere model based on mass spectrometer and incoherent scatter radar (MSIS) [11, 18, 28]. The model from 2000 makes use of satellite accelerometer data, observations using incoherent scatter radar and molecular oxygen number densities. Further, it includes an anomalous oxygen component in its equations, being especially important to high-altitude density estimations. To consider solar activity and the strength of solar extreme ultraviolet (EUV) radiation, the model uses the observed 10.7 cm solar radio flux as an input. Values have to be provided for the previous day ($F_{10.7}$) and an 81-day time-centered average ($\bar{F}_{10.7}$). Regarding geomagnetic activity, the 3-hourly planetary equivalent amplitude values a_p or its daily average A_p are employed [28].

Jacchia developed several empirical models for atmospheric density. Making use of analytic expressions for the exospheric temperature depending on location as well as solar and geomagnetic activity, density values can be derived through empirical temperature profiles and/or the diffusion equation. The newer models also include satellite mass spectrometer data [11]. In 2006, *Bowman et al.* developed an upgraded version of the *Jacchia* model and published another improved version in 2008 [29]. It includes semi-annual density variations and utilises further proxies for solar activity. Besides the observed solar radio flux at 10.7 cm ($F_{10.7}$), proxies have to be provided for 26 nm to 34 nm solar EUV emission (S_{10}), for solar middle ultraviolet (MUV) radiation at 280 nm (M_{10}) and for the X-ray emission of the sun (Y_{10}). The disturbance storm time (Dst) is used as an index for geomagnetic activity. [29]

The *International Organization for Standardization* has defined different levels of solar and geomagnetic activity by specifying values for the various parameters, which can be

useful to compare different scenarios of solar and geomagnetic activity. The respective indices can be found in Table 2.2.

Table 2.2 – Levels of solar and geomagnetic activity as defined in ISO1422 [30]. Each value is given in the respective index unit and is to be applied for the average index value as well. A further high short-term level is given in the norm, which is not included here.

Activity level	$F_{10.7}$	S_{10}	M_{10}	Y_{10}	A_p	Dst
Low	65	60	60	60	0	-15
Moderate	140	125	125	125	15	-15
High	250	220	220	220	45	-100

3 Basics of collision avoidance

This chapter deals with collision avoidance involving aerodynamic drag. First, the processes behind conjunction detection and assessment are presented. An introduction to state-of-the-art collision avoidance manoeuvres leads over to the usage of aerodynamic drag as means of control in avoidance manoeuvres. For this a method to assess the influence of a change in a satellite's ballistic coefficient on its trajectory is outlined. Eventually, previous collision warnings for the *Flying Laptop* are analysed to gain a deeper understanding of the practical environment.

3.1 Conjunctions

A conjunction is a close encounter between a satellite and another object (a defunct or working satellite or debris object). Such conjunctions pose an inherent threat because of the risk of a potential collision, which almost certainly results in a loss of the satellite. Moreover, collisions produce a high amount of debris particles, which themselves increase the collision risk for other operating satellites. This section describes how conjunction warnings are issued and how collision probabilities can be calculated.

3.1.1 Conjunction Data Messages

The *Joint Space Operations Centre* (JSpOC) provides services for satellite operators regarding conjunction events [31, 32].¹ A proprietary catalogue of satellites and debris objects is continuously screened for close encounters with a miss distance below a defined threshold. When a close encounter is identified, more thorough analyses are performed including high-fidelity orbit determination and propagation as well as uncertainty estimations. The available information regarding a conjunction are then summarised in a *Conjunction Data Message* (CDM), which is sent to the satellite operators. The CDM's format and content are standardised [15]. Each CDM contains information about the two objects involved in the encounter, including (if applicable) name, type, operator name, whether they are manoeuvrable or not and their considered radius. The predicted time of closest approach t_{ca} and the predicted positions and velocities of both objects are presented, accompanied by an estimate of the position covariance matrices. The observation time intervals and the used models for orbit determination and subsequent propagation

¹The *German Space Operations Centre* (GSOC) releases conjunction warnings as well, either upon reception of a JSpOC warning or when identifying a close encounter in a TLE catalogue [33].

are stated as well as the ballistic and solar radiation coefficients used for propagation. The stated ballistic coefficient is to be highlighted because it will be used as a reference value later on. Lastly, orbital information about the objects are given, including apogee and perigee heights, eccentricity, and inclination. An example CDM for a close encounter on April 7, 2022, is included in Appendix A.

3.1.2 Calculation of the collision probability

Naturally, predictions about conjunctions are fraught with uncertainties. Therefore, a probability of collision associated with a close encounter is used as a main metric for risk assessment. Foster developed a method to calculate a collision probability for a given conjunction geometry by reducing the three-dimensional problem to a 2-dimensional one [34]. Many different implementations based on this original method have been derived since then [31, 34, 35, 36] and the JSpOC uses the method as well [37, 38]. The FOSTER-1992 method makes the following assumptions:

- Both objects move at such high (relative) velocities, that the encounter duration can be considered short and their motion can be assumed rectilinear, i.e., with constant velocity and along a straight line, during the encounter.
- The uncertainties in the position components each follow a Gaussian distribution.
- Velocity uncertainties are neglected.
- The uncertainties are constant during the encounter, their values are the predicted values at t_{ca} .
- The uncertainties in the primary and secondary object positions are uncorrelated and can thus be joint into the combined covariance by simple addition.
- Each object is represented by a sphere fully enclosing the satellite. Its radius is called the hard body radius.

Fig. 3.1 depicts the geometry during a close encounter. The norm of the relative position vector between both objects at time of closest approach $\Delta \mathbf{r}_{tca} = \mathbf{r}_2 - \mathbf{r}_1$ is referred to as the miss distance. The plane containing the relative position vector and being normal to the relative velocity vector is called the conjunction plane, or *B*-plane. The relative position vector further defines the *x*-axis of the conjunction frame.

As mentioned before, the uncertainties in the satellite's and secondary object's positions are typically specified as covariance matrices in the respective RTN frames $\mathbf{C}_{i,RTN}$. Such a covariance matrix is symmetric and describes a 3-dimensional ellipsoid indicating the 1σ environment of the position. The elements on the main diagonal represent the covariances $\sigma_R^2, \sigma_T^2, \sigma_N^2$, i.e., the respective radial, transversal and out-of-plane components of the position uncertainty. The principle axes of the 1σ -ellipsoid are defined by the eigenvectors of the covariance matrix and might deviate from the RTN axes due to off-diagonal elements not being equal to zero.

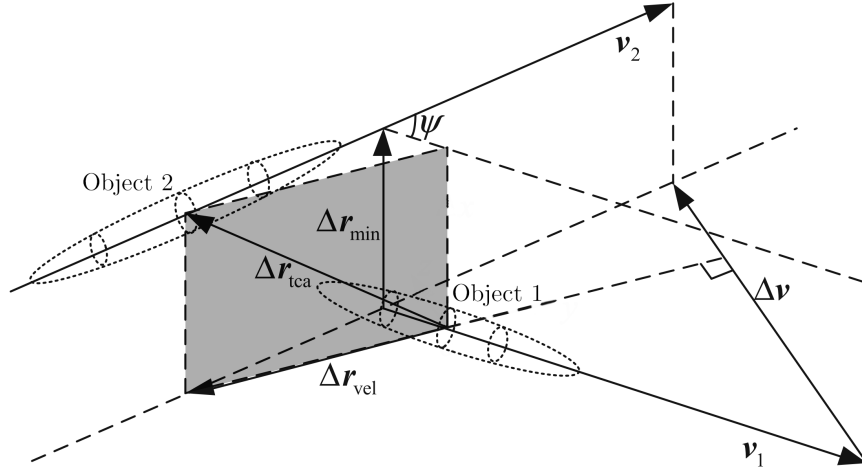


Figure 3.1 – Illustration of the conjunction geometry with the conjunction plane in grey (adapted from [39]).

Klinkrad gives a transformation matrix for the transformation from the ECI frame to an object RTN frame [35]. Considering the rotation of the ECEF frame with respect to the inertial space, the transformation from ECEF to RTN may be written as the transformation matrix

$$\mathbf{R}_{RTN,ECEF} = \begin{bmatrix} \mathbf{U} \\ \mathbf{V} \\ \mathbf{W} \end{bmatrix} \quad (3.1)$$

with

$$\begin{aligned} \mathbf{U} &= \frac{\mathbf{r}_{ECEF}}{|\mathbf{r}_{ECEF}|} \\ \mathbf{V} &= \mathbf{W} \times \mathbf{U} \\ \mathbf{W} &= \frac{\mathbf{r}_{ECEF} \times (\mathbf{v}_{ECEF} + \boldsymbol{\omega}_E \times \mathbf{r}_{ECEF})}{|\mathbf{r}_{ECEF} \times (\mathbf{v}_{ECEF} + \boldsymbol{\omega}_E \times \mathbf{r}_{ECEF})|} \end{aligned}$$

Here $(\mathbf{v}_{ECEF} + \boldsymbol{\omega}_E \times \mathbf{r}_{ECEF})$ yields the velocity in inertial space [13]. Covariance matrices given in object RTN-frames can be, hence, transformed to the ECEF frame with a transformation matrix $\mathbf{R}_{RTN,ECEF}^T$ by

$$\mathbf{C}_{ECEF} = \mathbf{R}_{RTN,ECEF}^T \mathbf{C}_{RTN} \mathbf{R}_{RTN,ECEF} \quad (3.2)$$

Foster's approach is to combine the two objects' covariances into one combined covariance

$$\mathbf{C}_{tot,ECEF} = \mathbf{C}_{1,ECEF} + \mathbf{C}_{2,ECEF} \quad (3.3)$$

which is assigned to the secondary object. On the other hand, the two objects' hard body radii are added as well and assigned to the primary object, yielding the collision sphere with radius R_C . Therefore, a collision occurs if the distance between both objects at t_{ca} is smaller than the radius of the collision sphere, i.e., the collision sphere is intersected.

Due to the assumption of rectilinear motion, it is possible to convert the three-dimensional problem to a two-dimensional one by projecting the combined covariance ellipsoid and the collision sphere onto the conjunction plane (cf. Fig. 3.2). The resulting covariance ellipse on the conjunction plane is characterised by the projected combined covariance matrix:

$$\mathbf{C}_{tot,B} = \mathbf{R}_{B,ECEF} \mathbf{C}_{tot,ECEF} \mathbf{R}_{B,ECEF}^T \quad (3.4)$$

The projected covariance $\mathbf{C}_{tot,B}$ represents a Gaussian probability distribution in the B -plane. By integrating the probability density function over the collision area A_C (i.e., the projected collision sphere), a probability of collision can be estimated:

$$P_c = \frac{1}{2\pi\sqrt{\det(\mathbf{C}_{tot,B})}} \int_{-R_C}^{R_C} \int_{-\sqrt{R_C^2-x_B^2}}^{\sqrt{R_C^2-x_B^2}} \exp(-A_B) dy_B dx_B \quad (3.5)$$

$$\text{with: } A_B = \frac{1}{2} \Delta \mathbf{r}_B^T \mathbf{C}_{tot,B}^{-1} \Delta \mathbf{r}_B$$

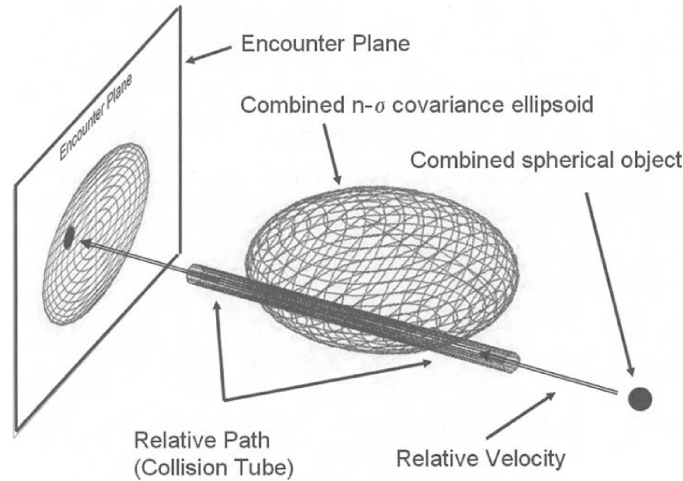


Figure 3.2 – Projection of the combined covariance ellipsoid on the conjunction plane [40].

JSpOC uses to integrate the probability density over a square area, which fully contains the circular collision area. In this case, the boundaries of the inner integral have to be modified to be $(-R_C, R_C)$ as well. This method typically leads to slightly higher collision probabilities due to the greater area of integration.

3.2 State-of-the-art collision avoidance

Upon reception of a collision warning indicating a close encounter with another object at a predicted time, a satellite can alter its orbit to increase the miss distance and reduce the risk of a collision. Collision warnings are typically issued a few days in advance to the conjunction, which is the available time for the planning and execution of a collision avoidance manoeuvre (CAM). Satellites with the ability to perform impulsive thrust ma-

manoeuvres can increase the miss distance by applying a Δv . Two strategies are often used depending on the exact conjunction geometry and available time. Around half an orbital revolution before the encounter, a thrust applied parallel to the velocity vector increases the radial miss distance at the time of closest approach. This is especially useful for conjunction in which both objects approach each other head-on. Another possibility, which is used in lateral conjunctions, is to perform such a burn several orbits before the close encounter leading to an increase of the in-track component of the miss distance [41]. A third option are out-of-plane forces to enlarge the cross-track miss distance but they are very propellant-intensive and rarely used [42]. Another impulsive manoeuvre might be necessary afterwards to restore the initial orbit [33]. All these manoeuvres cost propellant and potentially mission time. So eventually, it comes down to a trade-off between these costs and an accepted risk of collision.

CAMs making use of natural perturbations like aerodynamic drag and solar radiation pressure (SRP) have been studied in literature [43, 44, 45]. By attaining a specific flight attitude for a certain interval and thus applying an in-plane force, a separation distance can be created through a change in semi-major axis. This makes them especially useful for non-maneuvrable satellites, which otherwise would have no possibility to perform CAMs, at all. The only requirement is for the satellite to have an asymmetric shape in order to vary experienced perturbing accelerations. However, due to the accelerations being magnitudes smaller than those created by chemical thrusters, the savings in propellant come with a greater manoeuvre duration in order to achieve a desired miss distance.

Mishne and *Edlerman* compared the perturbing accelerations due to atmospheric drag and SRP and concluded, that their magnitudes are comparable at 500 km to 800 km. At lower altitudes, drag is the major perturbing force, whereas SRP becomes dominant at higher altitudes. Both forces have in common that their direction is fixed: Drag acts parallel to the relative velocity of the surrounding atmosphere and SRP acts parallel to the Sun vector. Drag is, therefore, independent of the orbital orientation in space. Neglecting atmospheric winds and rotation, it always acts as an in-plane force. The in-plane component of SRP, on the other side, is greatly depending on the orbit's orientation with respect to the Sun. *Mishne* and *Edlerman* showed that the effectiveness of SRP for CAMs is the highest for sun-synchronous orbits with a local time of ascending node (LTAN) between 10:00 and 14:00. For inclined, non-sun-synchronous orbits, the effectiveness varies strongly over the course of a year [44].

3.3 Analytic estimation of achievable separation distance

As seen in Section 2.3, atmospheric drag induces a perturbing acceleration on a satellite. Due to its nature of being anti-parallel to the velocity, two satellites with equal initial states but different ballistic coefficients build up an in-track position distance over time. *Omar* and *Bevilacqua* have derived an analytic expression to study the effects of changes

in drag force and proposed its use for collision avoidance manoeuvres, which will be revised here [43]. The assumptions include a circular orbit over a spherical Earth, a non-rotating atmosphere and a negligible change in the semi-major axis during the manoeuvre.

Consider a satellite in an original, or reference, orbit around Earth denoted with the index r . A new, or perturbed, orbit, indexed with n , can be achieved by altering the ballistic coefficient, e.g., through a change in attitude. Let M_r and M_n denote the respective mean anomalies of the orbits and $\varphi = M_r - M_n$ their difference. The difference is zero initially, since both trajectories share the same initial conditions but will then change. The mean motion n of a satellite equals the time derivative of its mean anomaly, which results from the gravitational parameter of Earth μ_E and the semi-major axis. It follows that

$$\dot{\varphi}_{rn} = n_r - n_n = \sqrt{\frac{\mu_E}{a_r^3}} - \sqrt{\frac{\mu_E}{a_n^3}} \quad (3.6)$$

With the difference in semi-major axes $\delta = a_r - a_n$, this can be written as

$$\dot{\varphi}_{rn} = \sqrt{\mu_E} \left(a_r^{-\frac{3}{2}} - (a_n + \delta)^{-\frac{3}{2}} \right) \quad (3.7)$$

Under the assumption that the change in semi-major axis during the manoeuvre is small compared to the original semi-major axis ($\delta \ll a_r$), the latter term can be linearised using the binomial expansion theorem [46]:

$$(a_r + \delta)^{-\frac{3}{2}} = a_r^{-\frac{3}{2}} \left(1 + \frac{\delta}{a_r} \right)^{-\frac{3}{2}} \approx a_r^{-\frac{5}{2}} \left(a_r - \frac{3\delta}{2} \right)^{-\frac{3}{2}} \quad (3.8)$$

This is substituted in Eq. (3.7) yielding the first and second derivatives of the change in mean anomaly:

$$\dot{\varphi}_{rn} = \frac{3\delta\sqrt{\mu_E}}{2a_r^{\frac{5}{2}}} \quad (3.9)$$

$$\ddot{\varphi}_{rn} = \frac{3\sqrt{\mu_E}}{2a_r^{\frac{5}{2}}} \dot{\delta} \quad (3.10)$$

Omar and *Bevilacqua* further calculate the orbital energy E and its time derivative. The latter is directly linked to the magnitude of the acceleration due to aerodynamic drag and the satellite velocity via the work energy theorem:

$$E = -\frac{\mu_E}{2a} \quad (3.11)$$

$$\dot{E} = \frac{\mu_E}{2a^2} \dot{a} = p_{aero} v = -\frac{1}{2} C_B \rho v^3 \quad (3.12)$$

Since the atmosphere is assumed to be non-rotating, the relative velocity equals the orbital velocity and the vectors can be substituted by their norms. The orbital velocity is given by

$$v = \sqrt{\frac{\mu_E}{a}} \quad (3.13)$$

Combining Eqs. (3.12) and (3.13) gives the time derivative of the semi-major axis as

$$\dot{a} = -C_B \rho \sqrt{\mu E a} \quad (3.14)$$

Finally, this leads to the time derivative of the change in semi-major axis:

$$\dot{\delta} = \dot{a}_n - \dot{a}_r = -\rho \sqrt{\mu E a} (C_{B,n} - C_{B,r}) \quad (3.15)$$

Since δ is small compared to the original semi-major axis, the semi-major axes can be assumed to be approximately equal $a_r \approx a_n \approx a_0$. Further, the density is assumed constant. This yields an analytic expression for the second temporal derivative of φ_{rn} :

$$\ddot{\varphi}_{rn} = -\frac{3\rho\mu_E}{2a_0^2} (C_{B,n} - C_{B,r}) = -\frac{3\rho\mu_E}{2a_0^2} \Delta C_B \quad (3.16)$$

By integration over time, one can deduce the built-up angular difference after holding the off-nominal attitude for time Δt :

$$\Delta\varphi_{rn} = \frac{1}{2}\ddot{\varphi}\Delta t^2 + \dot{\varphi}_{rn,0}\Delta t \quad (3.17)$$

with $\dot{\varphi}_{rn,0}$ being the first derivative of φ_{rn} at the start of the observed interval. The collision avoidance manoeuvre proposed by *Omar* and *Bevilacqua* involves maintaining a specified off-nominal attitude for a duration t_s before taking the nominal attitude again for the remaining time $t_c - t_s$. One can deduce the built-up angular difference after the manoeuvre, i.e., at t_c :

$$\Delta\varphi_{rn} = \frac{1}{2}\ddot{\varphi}t_s^2 + \ddot{\varphi}t_s(t_c - t_s) = -\frac{3\rho\mu_E}{2a_0^2}\Delta C_B \left(\frac{1}{2}t_s^2 + t_s(t_c - t_s) \right) \quad (3.18)$$

Here, $\bar{\rho}$ denotes the average density over the manoeuvre duration. Alternatively, the difference can be expressed from the perspective of the reference trajectory as

$$\Delta\varphi = \frac{3\rho\mu_E}{2a_0^2}\Delta C_B \left(\frac{1}{2}t_s^2 + t_s(t_c - t_s) \right) \quad (3.19)$$

This angular separation can be converted into an in-track separation distance Δx :

$$\Delta x = \Delta\varphi \cdot a_0 = -\frac{1}{2}\ddot{\varphi}t_s^2 = \frac{3\rho\mu_E}{2a_0}\Delta C_B \left(\frac{1}{2}t_s^2 + t_s(t_c - t_s) \right) \quad (3.20)$$

Hence, an increase in ballistic coefficient for a certain time leads to the satellite advancing ahead in direction of flight from its original trajectory. This is schematically shown in Fig. 3.3. At some point in time t_c , both satellite positions are marked. The satellites have established a positive (in the direction of flight) separation distance of Δx due to the satellite having hold an off-nominal attitude with an increased ballistic coefficient for time t_s . Vice-versa, for a manoeuvre involving an attitude with a smaller-than-nominal ballistic coefficient the separation distance is negative. Obviously, such a manoeuvre is suitable to be used in case of a predicted close encounter. By attaining a commanded

attitude a satellite can achieve an in-track separation relative to a reference trajectory.

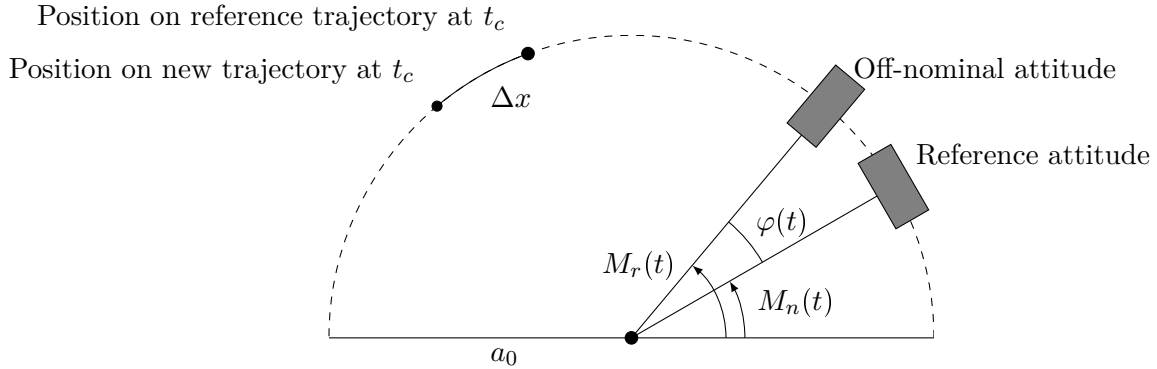


Figure 3.3 – Concept of the collision avoidance manoeuvre using aerodynamic drag. The off-nominal attitude has an increased ballistic coefficient, leading to a positive in-track separation distance to the reference trajectory. It is to note, that the satellites started from equal initial conditions and the separation distance builds up over time.

3.4 Previous collision warnings for the *Flying Laptop*

In this section, the conjunction warnings from JSpOC since the *Flying Laptop*'s launch in 2017 will be reviewed². In total, the *Flying Laptop* operators received 5114 collision warnings from JSpOC. 4136 of them showed a collision probability of $P_c = 0$ and will be dropped in the following. This is due to many close encounters fulfilling the report conditions described in Section 3.1.1 but leading to negligible collision probabilities. The 978 warnings with $P_c > 0$ were issued for 177 close encounters in total, leading to an average of 5.53 CDMs per close encounter. The CDMs are typically updated regularly until the time of closest approach. Of the 177 close encounters, 167 showed a collision probability $\geq 1 \times 10^{-4}$ in at least one of the issued CDMs, which is the typical threshold for the application of a CAM. On average, such a close encounter occurs every 11.32 days for the *Flying Laptop*.

As can be seen in Fig. 3.4, in more than 60 % of the close encounters the secondary object was identified as debris. In approximately a quarter of the cases, the *Flying Laptop* encountered objects of unknown type and only 12.43 % close encounters took place between the *Flying Laptop* and another payload. Of these payloads, 63.64 % were reported to be manoeuvrable. All in all, only 7.910 % of the secondary objects were proven to be manoeuvrable making conjunctions with objects which are themselves not capable of performing avoidance manoeuvres the regular case.

For every individual close encounter, the time from creation of the first CDM until the predicted time of closest approach was determined. The CDMs are received shortly after creation. Therefore, the mentioned time interval is a measure for the available time to plan and implement CAMs. The resulting distribution is plotted in Fig. 3.5. Only in 13.00 %

²CDMs received until September 21, 2022, are included.

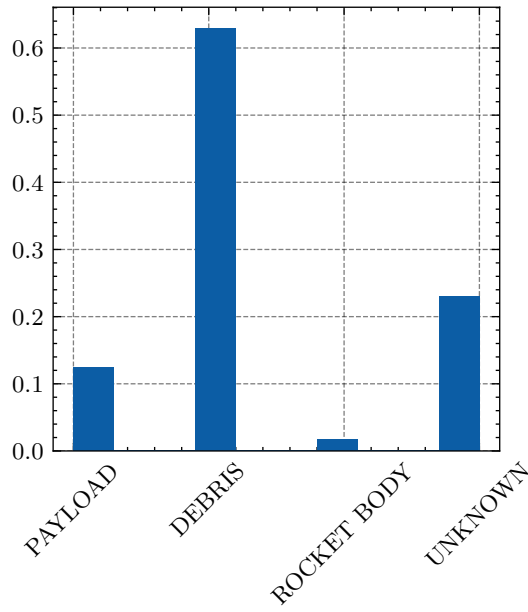


Figure 3.4 – Types of the secondary objects in close encounter with the *Flying Laptop*.

of the examined cases, the available time is ≤ 48 h, in 29.40 % it is ≤ 72 h. On average, there is an interval of 103.64 h between the first CDM and t_{ca} . For 50 % of the encounters, the available time is ≥ 110.69 h. Most encounters are first discovered 110 h to 120 h before the time of closest approach.

Lastly, the reference ballistic coefficient published in the CDMs is examined, Fig. 3.6 shows its evolution. Its maximum is reached in July, 2019, with a value of $C_{B,ref} = 0.02930 \text{ m}^2 \text{ kg}^{-1}$. The minimum is $0.01284 \text{ m}^2 \text{ kg}^{-1}$ in November, 2020. The overall average is $0.02238 \text{ m}^2 \text{ kg}^{-1}$. Beginning with the start of 2021, the reference ballistic coefficient starts to decrease steadily until today. Considering only CDMs since April, 2022, the reference ballistic coefficient shows an average of $0.01794 \text{ m}^2 \text{ kg}^{-1}$.

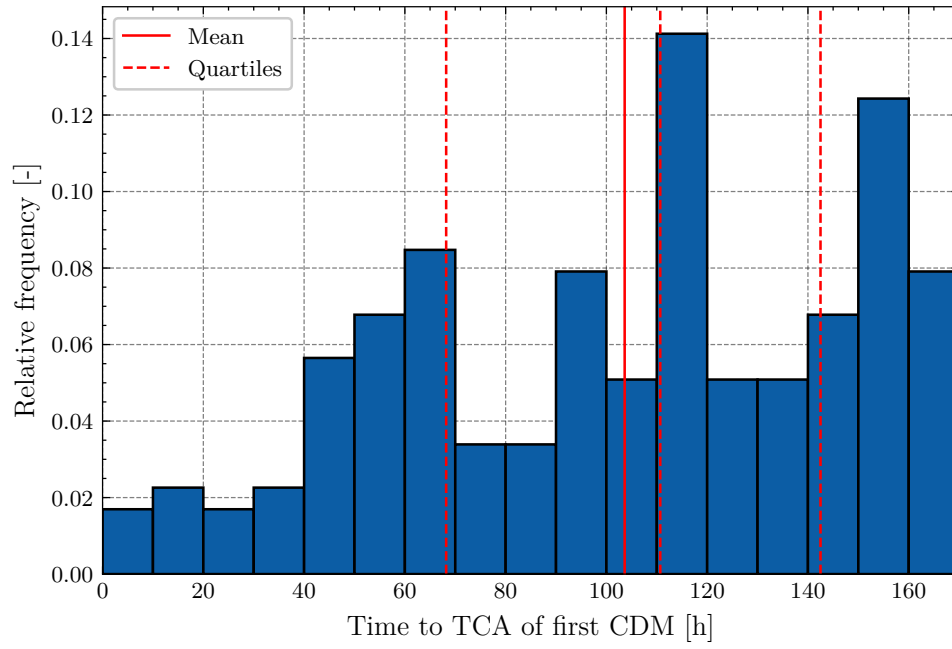


Figure 3.5 – Histogram of the time between creation of the first CDM and TCA for close encounters between the *Flying Laptop* and a secondary object.

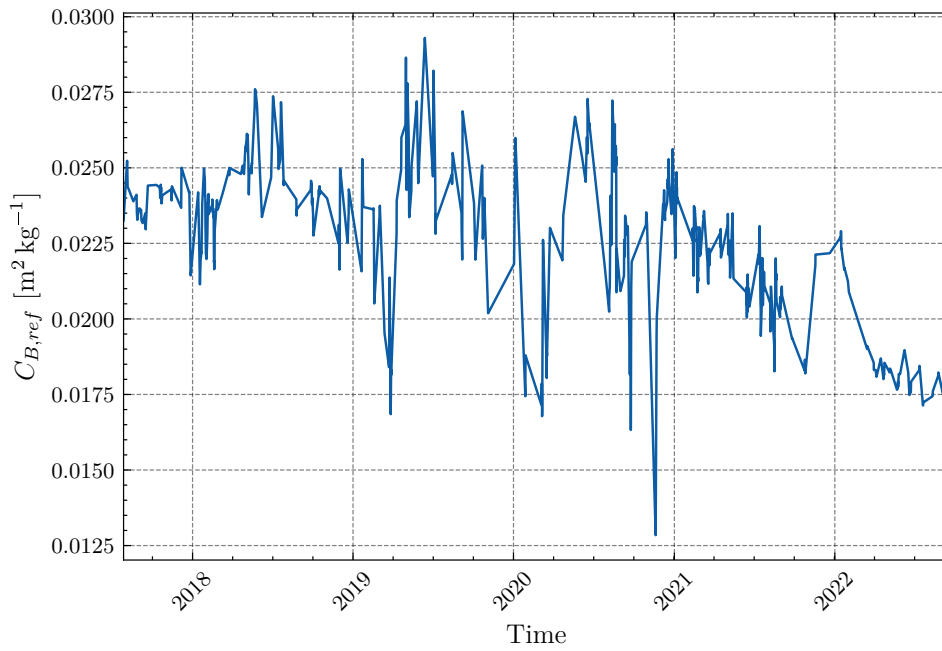


Figure 3.6 – The ballistic coefficient as stated in JSpOC CDMs over time.

4 Practical considerations

The following chapter describes practical challenges and general considerations when implementing collision avoidance manoeuvres using aerodynamic drag in practice. Operational constraints, resulting from different requirements for the *Flying Laptop* are covered at first. The second section deals with covariance realism and aims to explain the role of covariance estimations in the context of conjunction assessments.

4.1 Operational constraints

It has been explained before that collision avoidance on the basis of aerodynamic drag involves the adoption of specified attitudes. This may interfere with other mission goals and requirements, which has to be considered when planning CAMs. The flow profile around a satellite is symmetric around the relative velocity vector, though, allowing for one rotational degree of freedom when commanding attitudes with a desired ballistic coefficient. To some extent, this allows for the consideration of constraints.

Satellites in orbit are typically powered by solar energy. This requires solar panels to be oriented in a way allowing them to convert solar energy effectively. In practice, a satellite operator would like to maximise the effective area of the solar arrays with regards to the direction of the Sun, i.e., pointing their surface normal towards the Sun. Often, e.g., for the *Flying Laptop* (cf. Fig. 1.2), the solar panels represent the biggest surfaces of a satellite. This makes aligning their surface normal with the direction of flight suitable for maximising the effective cross-section and hence maximising the ballistic coefficient. Vice-versa, pointing them orthogonal to the flight direction leads to a minimised ballistic coefficient. This can lead to conflicts between a potential CAM and the need for generating power. For the *Flying Laptop*, the current orientation of its orbital plane (cf. Fig. 4.1) is close to perpendicular to the Sun vector. Thus, pointing the solar arrays towards the flight direction results in a very small effectiveness in power generation. This has to be met by including phases in a planned manoeuvre with an attitude allowing for the solar panels to recharge the satellite batteries, if the planned manoeuvre duration is so long that a discharge might be possible. Of course, that reduces the achievable separation distance. In case the manoeuvre involves a flight with the solar arrays oriented perpendicular to the direction of flight (as in minimum drag configuration, cf Chapter 5), they can be pointed roughly towards the Sun continuously.

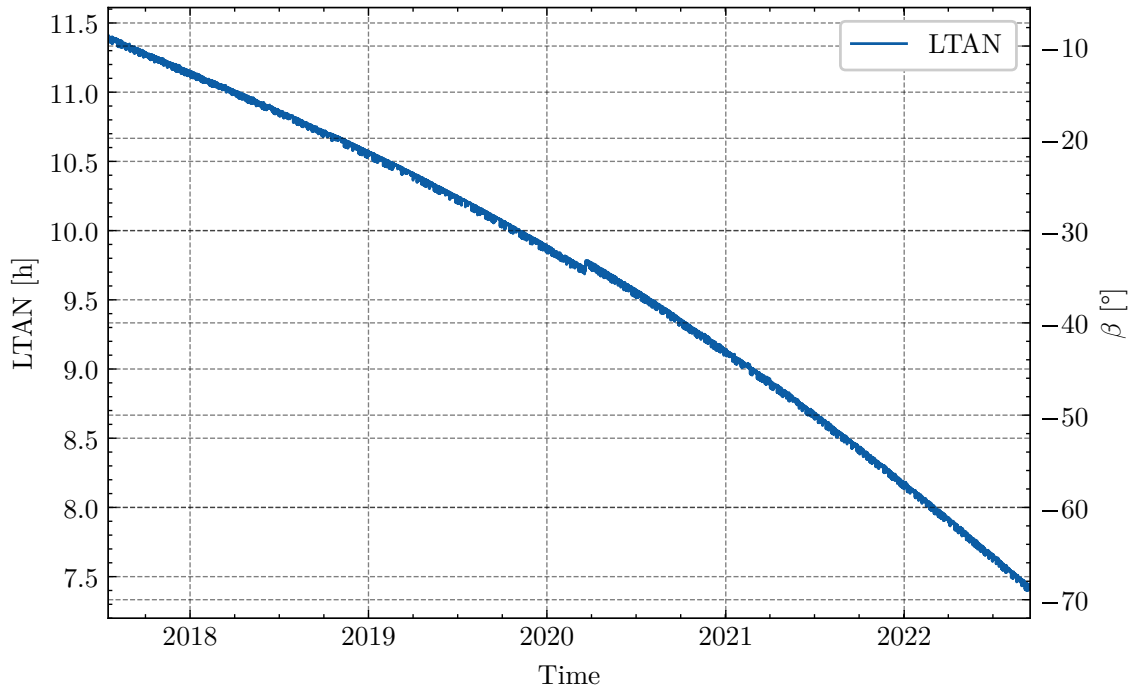


Figure 4.1 – The *Flying Laptop*’s local time of ascending node and the angle β between the orbital plane and the Sun vector over the course of its mission.

Further constraints are rooted in the mission goals. Passes over ground stations are essential for commanding the satellite and downlinking data. The satellite must establish a connection by pointing its antennas towards those of the ground station. Besides the payload data, especially telemetry data are important during a CAM, since they allow for the supervision of the correct implementation and observation of the manoeuvre’s effectiveness. Given that passes only happen a few times per day, their effect on an CAM with a duration of several days is negligible. Similarly, mission pointing requirements for measurements or observations may be considered during a CAM, provided that they are short.

The pointing accuracy of a satellite must be taken into account as well, with its quality depending on the satellite attitude control system and the used sensors. Inaccuracies in pointing manifest themselves in deviations of the actual from the assumed effective cross-section. When designing CAMs, such inaccuracies must be accounted for, since they affect the achievable separation distance. The *Flying Laptop* makes use of two star trackers, whose reliability decreased slightly during their lifetime. Commanded pointings are only able to be implemented, when the star trackers deliver valid signals. This highlights again the importance of supervising a CAM and gathering data meanwhile.

4.2 Covariance realism

The covariance matrices of the objects' position uncertainties play an important role in the process of collision probability calculation and therefore need to be modelled carefully. Research has been conducted on how the projected combined covariance \mathbf{C}_B affects the probability of collision [38], which can be summarised as follows:

Combined covariance size For a fixed miss distance, the collision probability depends on the form of the probability density distribution specified by the 1σ -environment of the uncertainty. The covariance is directly linked to the magnitude of P_c :

- For very small covariances, P_c is low, since the collision area is in the tail region of the probability density function, where it is low as well.
- For growing covariances, P_c grows until it reaches a maximum.
- For high covariances, P_c is low again due to the probability density function being highly stretched and therefore flat.

Combined covariance orientation P_c is higher the smaller the angle between the first principal axis of the covariance ellipse and the miss distance vector. Increasing eccentricity of the combined covariance ellipse increases this effect.

Combined covariance shape It is questionable, how well a Gaussian distribution function models uncertainties in orbital motion, which follows curvilinear paths. However, it was shown that the shape of the covariance has little impact on P_c compared to size and orientation. Gaussian distribution functions may be used.

To realistically model position uncertainties, the JSpOC utilises two methods to scale the individual covariances obtained from its orbit determination and propagation algorithms. First, a consider parameter (DCP) is calculated, accounting for atmospheric density mis-modelling and uncertainties in the object's ballistic coefficient. Second, the whole covariance is scaled with the weighted Root Mean Square error of the least-squares orbit determination if it is greater than unity [37, 38]. Both the DCP and the RMS are given in CDMs.

At this point in time, the author is not aware of any publication on how the JSpOC implemented covariance scaling with the DCP. While the implemented method for calculating P_c has been verified using exemplary conjunctions given by *Klinkrad*, *Chen* and NASA [35, 39, 47], the probabilities of collision given in CDMs could not be recreated. To deal with this, two methods for calculating maximum collision probabilities independent of the covariance size are introduced.

Klinkrad presented a way to determine a maximum collision probability for an uncertainty of given shape and orientation. Let k be a scaling factor for the 1σ -dispersion of the combined uncertainty:

$$\mathbf{C}_{tot,B}^* = k^2 \mathbf{C}_{tot,B} \quad (4.1)$$

For a fixed miss distance, there is a scaling factor k_{max} for which the resulting probability of collision is maximum. This maximum collision probability is given by [35]:

$$P_{c,max} = \frac{R_C^2}{\sqrt{\det(\mathbf{C}_B)} \Delta \mathbf{r}_B^T \mathbf{C}_{tot,B}^{-1} \Delta \mathbf{r}_B} \quad (4.2)$$

The dependency of the collision probability on the scaling factor can be interpreted in the following way: For a very small uncertainty the probability of collision is low, since the objects' positions are fairly certain. If the miss distance is greater than zero, they are unlikely to collide. For growing position uncertainties the collision probability grows until it reaches a maximum. Higher position uncertainties cause it to decrease again, for the respective probability density distributions are increasingly flattened.

Alfano developed another method to determine the maximum collision probability based on the aspect ratio $AR = \frac{\sigma_{B,1}}{\sigma_{B,2}}$ between the semi-major and semi-minor axes of the projected covariance ellipse [44, 40]. The maximum collision probability results from

$$P_{c,max,alf} = \frac{R_C^2}{2AR\sigma^2} \exp \left\{ \left(-\frac{1}{2} \left(\frac{\Delta r_{tca}}{AR\sigma} \right)^2 \right) \right\} \quad (4.3)$$

with $\sigma = \frac{\Delta r_{tca}}{\sqrt{2AR}}$. This metric includes information about the eccentricity of the combined covariance matrix. An infinite aspect ratio is the worst case with a probability of collision of

$$P_{c,max,alf,inf} = \frac{1}{2} \left[\operatorname{erf} \left(\frac{r_{sd} + 1}{2\sqrt{r_{sd}}} \sqrt{-\ln \left(\frac{1 - r_{sd}}{1 + r_{sd}} \right)} \right) + \operatorname{erf} \left(\frac{r_{sd} - 1}{2\sqrt{r_{sd}}} \sqrt{-\ln \left(\frac{1 - r_{sd}}{1 + r_{sd}} \right)} \right) \right] \quad (4.4)$$

where $r_{sd} = \frac{R_C}{\Delta r_{tca}}$. This maximum collision probability does not include any information about the covariance size or orientation and is thus an upper bound for the collision probability.

5 Aerodynamic analysis of the *Flying Laptop*

To estimate the influence of changes in attitude on the *Flying Laptop*'s trajectory, the satellite is analysed with regards to its aerodynamic properties. For this, an available software tool is used. The methodology and results are presented in this chapter.

5.1 Model of the *Flying Laptop*

The geometry of the *Flying Laptop* will be analysed using the panel method: Every surface is modelled individually and its contribution to the total aerodynamic forces is calculated. Therefore, the computational costs increase with the number of surfaces in the satellite model. To meet this, the original CAD model of the *Flying Laptop* is simplified, leading to a drastic decrease of individual surfaces while still representing the satellite's geometry. A comparison of the original and the simplified model is shown in Fig. 5.1. The major surfaces are accounted for in the simplified model, while the instruments are removed. The main body of the satellite bus measures approximately $530 \times 670 \times 660 \text{ mm}^3$ ($x \times y \times z$), while the solar panels have a span of about 1922 mm. The weight is 108.8 kg.

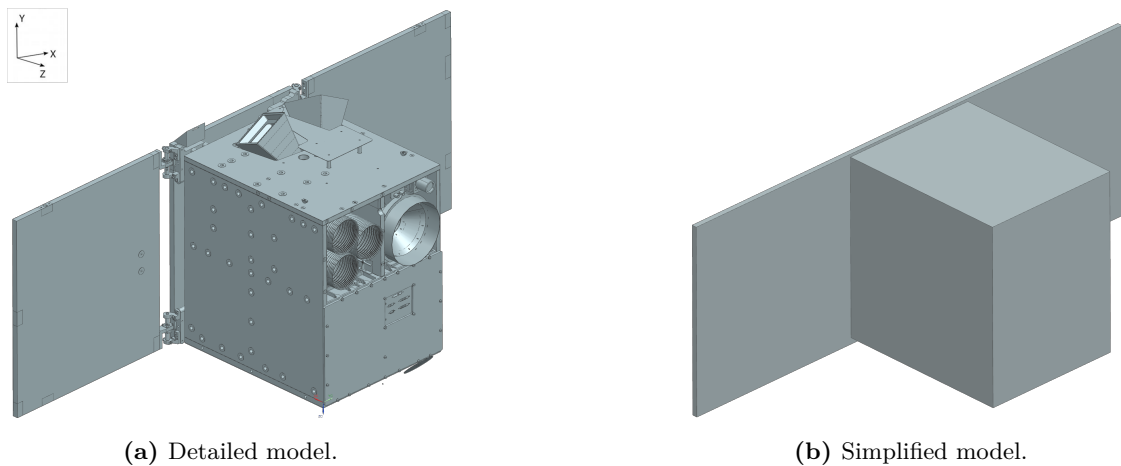


Figure 5.1 – Comparison of the detailed CAD model and the simplified model used for the aerodynamic analysis. The body coordinate system is defined as in Fig. 1.2b

The ballistic coefficient of the *Flying Laptop* can be maximised by maximising the area perpendicular to the relative velocity¹. This corresponds to a flight with maximum drag. Vice versa, the minimisation of this area leads to a minimum ballistic coefficient. The

¹Since no atmospheric wind is assumed, the relative velocity is parallel to the direction of flight.

respective maximum and minimum drag attitude are defined by having either the body z -axis (maximum drag) or y -axis (minimum drag) point parallel to the direction of flight. To protect the payload cameras and the star trackers from atmospheric particles, the negative z or y -axes are pointed towards flight direction. The nadir-pointing attitude is defined by having the z -axis pointing towards the centre of Earth and the x -axis in the direction of flight. The different attitudes are shown in Fig. 5.2.

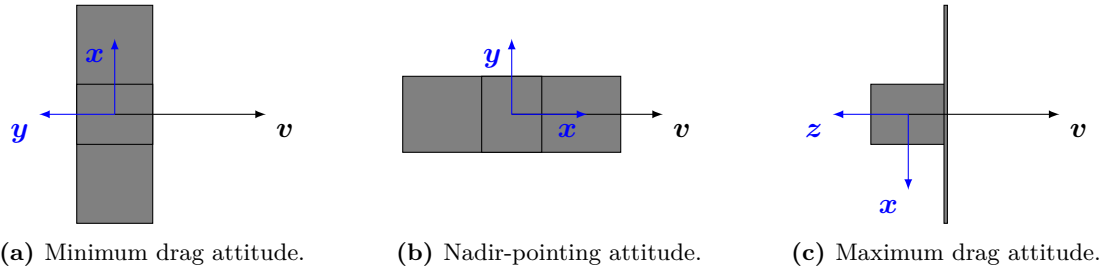


Figure 5.2 – Schematic illustrations of the different specified attitudes of the *Flying Laptop* with the body coordinate system. All attitudes can be rotated around the direction of flight without changing the flow field.

5.2 ADBSat analysis

Sinpetru, Crisp et al. developed the software tool ADBSat for the determination of aerodynamic coefficients [23, 26]. It offers the possibility to analyse a satellite geometry with regards to its aerodynamic properties. Besides the CAD model of the satellite, a position (latitude, longitude and altitude), time and the respective indices for solar and geomagnetic activity for the NRLMSISE-00 atmosphere model are needed as inputs. The NRLMSISE-00 model is used to derive the atmospheric composition and temperature at the position and time. Based on this, the gas-surface interactions are modelled using the Sentman model². Finally, the aerodynamic force on every surface panel is calculated. The individual panels' contributions are added to form the total aerodynamic forces and coefficients. Since the ballistic coefficient is, therefore, dependent on atmospheric composition and temperature, it will be analysed for varying solar and geomagnetic activity levels.

As outlined in Section 2.3.1, different parameters are needed as input for the Sentman model. The wall temperature is set to be 300 K, as it is often assumed in literature [18, 48]. The accommodation coefficient requires closer examination.

5.2.1 Accommodation coefficient

Satellite aerodynamics and gas-surface interaction have been studied intensively for very low Earth Orbits (VLEO)³ including the development of several models. Still, less is known about altitude regimes above 500 km and the applicability of the aforementioned

²Other GSIMs are available as well but will not be used here.

³Very low Earth Orbits are orbits below 450 km.

models has to be checked carefully. Regarding the introduced Sentman model, this especially concerns the accommodation coefficient. In literature, the Semi-Empirical Satellite Accommodation Model (SESAM) is often used for estimating the accommodation coefficient depending on number density of atomic oxygen n_O and atmospheric temperature T [48]:

$$\alpha_T = \frac{7.5 \cdot 10^{-17} \cdot n_O T}{1 + 7.5 \cdot 10^{-17} \cdot n_O T} \quad (5.1)$$

It is estimated to be valid for $0.85 \leq \alpha \leq 1^4$ and to be used with the NRLMSISE-00 model to obtain the number density of atomic oxygen and the atmospheric temperature [48, 49, 24]. In Fig. 5.3, the accommodation coefficient as estimated by SESAM is plotted over altitude. It becomes obvious that for the altitude regimes of the *Flying Laptop* the accommodation coefficients as calculated by SESAM can only be considered valid for high solar and geomagnetic activity. In general, accommodation tends to decrease with increasing altitudes due to less adsorption of molecules at the surface [24]. This shows in a shift to specular reflection leading to higher aerodynamic coefficients.

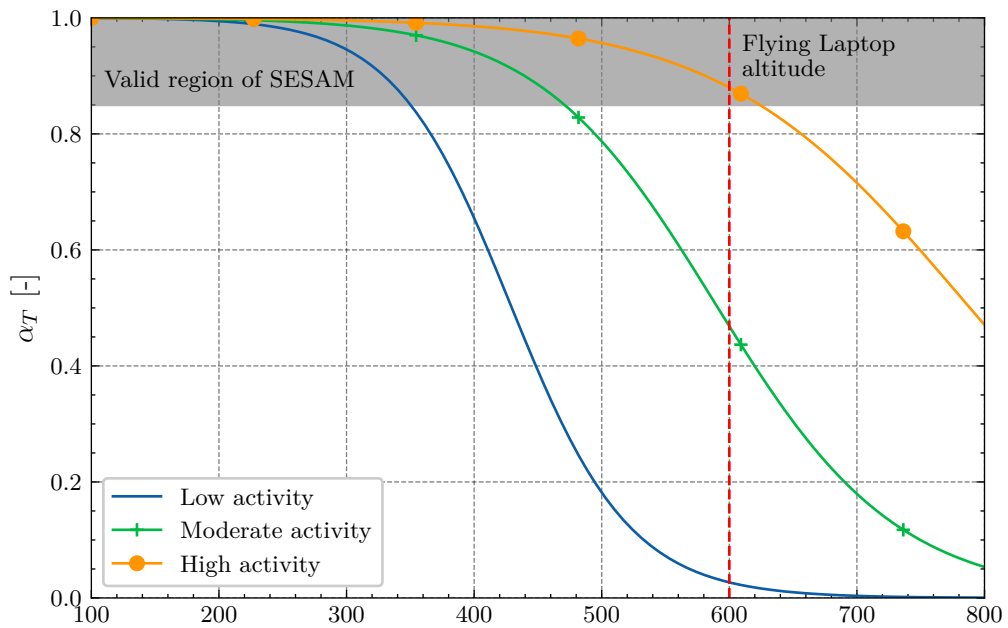


Figure 5.3 – The accommodation coefficient according to SESAM as function of altitude over $0^\circ\text{N}, 0^\circ\text{E}$ for different levels of solar and geomagnetic activity on April 1, 2022, 12:00 UTC. Atmospheric composition and temperature were determined using the NRLMSISE-00 model.

In the absence of better estimates, the accommodation coefficient is here obtained using the SESAM model. The output is, however, restricted to be minimum 0.85 and thus valid in the sense of the model. For the maximum drag configuration, this corresponds to a conservative approach. The calculated drag coefficient is expected to be a lower bound on the actual value, since aerodynamic drag increases with decreasing accommodation levels. For the minimum drag configuration, however, this needs to be considered.

⁴Alternatively, a valid altitude range of 100 km to 500 km is given. This is approximately the region, in which the model's output accommodation coefficient typically satisfies $0.85 \leq \alpha \leq 1$.

5.2.2 Results

The three different attitudes (cf. Fig. 5.2) are analysed with the ADBSat tool. Atmospheric conditions are heavily depending on the geocentric position. Therefore, an approximated circular orbit of the *Flying Laptop* is assumed with an inclination of 97.4° and an LTAN of 06:00 h. The ADBSat tool is employed to determine the drag coefficient of the satellite in the respective attitudes at 100 points on this orbit and the results are then averaged over these evaluation points. The averaging tends to cancel out variations due to the *Flying Laptop*'s changing orbit as well. Using Eq. (2.7), the drag coefficients can be translated into corresponding ballistic coefficients. ADBSat uses the largest surface, i.e., the solar panels, as a reference area in each attitude. Fig. 5.4 shows the the analysis visualisations in ADBSat for minimum and maximum drag attitude. The areas exposed to the flow are the ones which mainly contribute to aerodynamic drag.

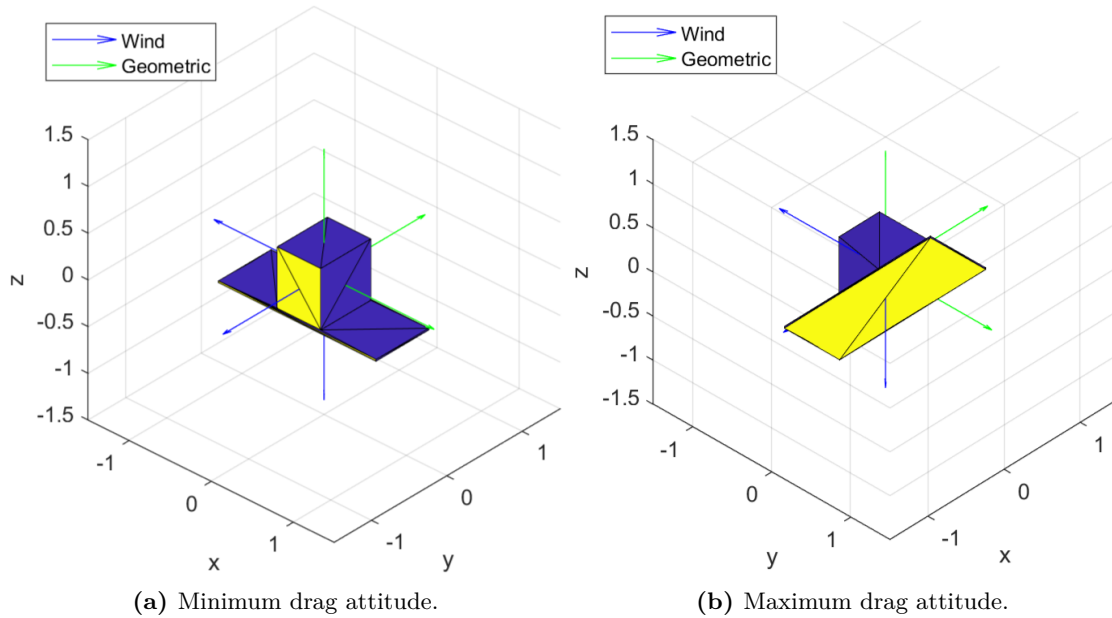


Figure 5.4 – The visualisations from the ADBSat tool for minimum and maximum drag attitude for moderate solar activity at 600 km altitude over $0^\circ\text{N}, 9^\circ\text{E}$ on April 1, 2022, 12:00 UTC. Yellow areas correspond to areas contributing to aerodynamic drag.

The ballistic coefficients are evaluated for the following values of the solar flux and geomagnetic activity:

$$F_{10.7} = \begin{bmatrix} 30 & 50 & 70 & \dots & 230 & 250 \end{bmatrix} \quad (5.2)$$

$$\bar{F}_{10.7} = \begin{bmatrix} 30 & 50 & 70 & \dots & 230 & 250 \end{bmatrix} \quad (5.3)$$

$$A_p = \begin{bmatrix} 0 & 5 & 10 & \dots & 40 & 45 \end{bmatrix} \quad (5.4)$$

For use in the simulation tool, the resulting ballistic coefficients are stored in 3-dimensional look-up tables, allowing a determination of the ballistic coefficient of an attitude via linear interpolation given specific values of the activity. Table 5.1 provides the resulting ballistic

coefficients for the previously defined activity levels (cf. Table 2.2). It becomes clear that the ballistic coefficient is significantly lower in minimum drag attitude, indicating a lower drag force acting on the satellite. In minimum drag attitude and nadir-pointing, the ballistic coefficients show a minimum for moderate activity and slightly higher but comparable values for high activity. The ballistic coefficients for moderate activity amount to 87.77 % and 89.81 % of the value for low activity, respectively. In maximum drag attitude, the ballistic coefficient is less dependent of the activity level, showing a difference of only 3.393 % between low and high activity.

Table 5.1 – Ballistic coefficients for different flight configurations and levels of solar and geomagnetic activity.

Flight configuration	Low activity C_B [m ² kg ⁻¹]	Moderate activity C_B [m ² kg ⁻¹]	High activity C_B [m ² kg ⁻¹]
Minimum drag attitude	1.384×10^{-2}	1.214×10^{-2}	1.220×10^{-2}
Nadir-pointing	1.475×10^{-2}	1.324×10^{-2}	1.328×10^{-2}
Maximum drag attitude	3.377×10^{-2}	3.262×10^{-2}	3.258×10^{-2}

Fig. 5.5 visualises the analysis results of the *Flying Laptop* in minimum and maximum drag attitude. It can be detected that the solar flux and its 81-day mean show a comparable influence on the ballistic coefficient. The ballistic coefficient tends to decrease with increasing solar and geomagnetic activity. The results for the nadir-pointing attitude are provided in Appendix B.

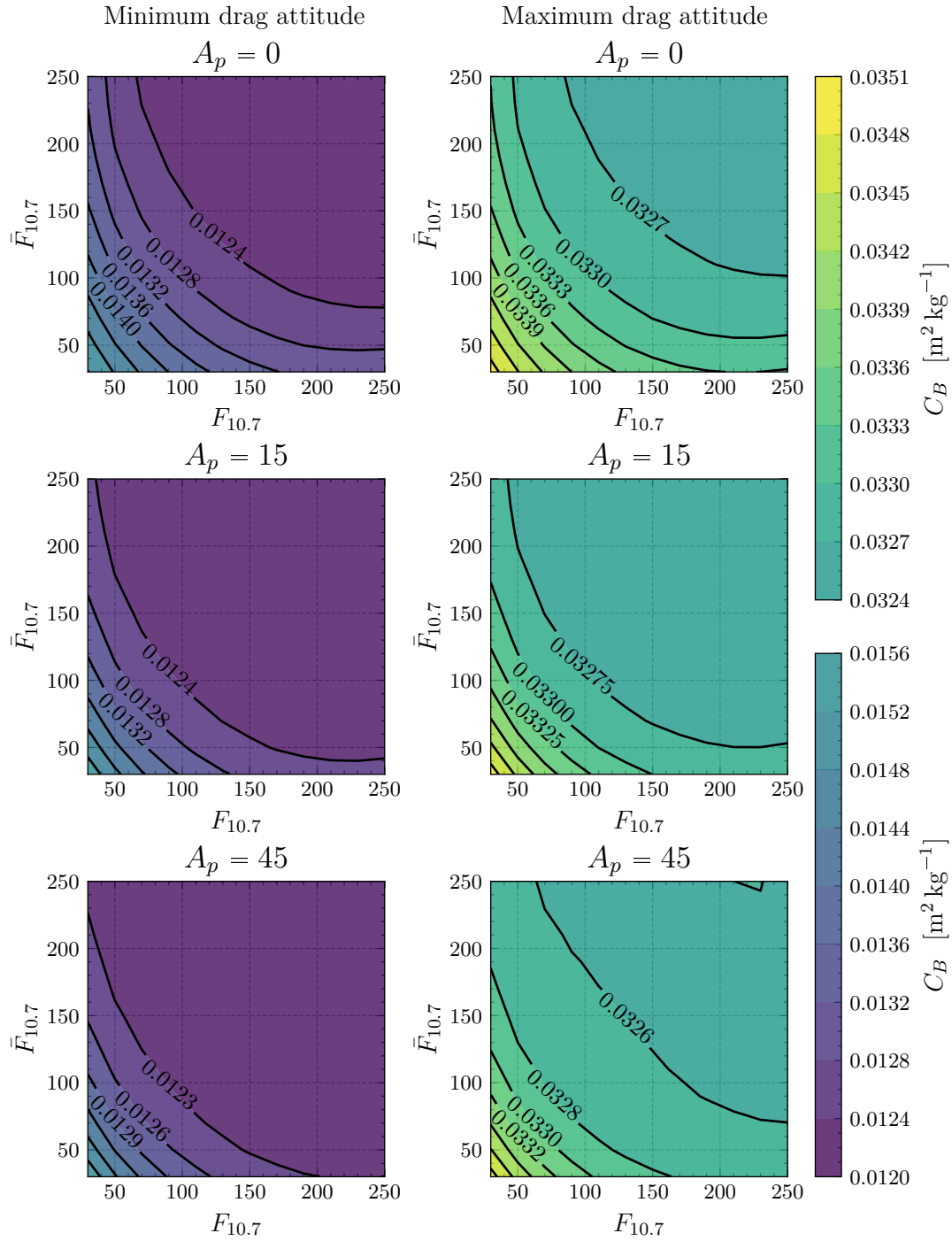


Figure 5.5 – Ballistic coefficient of the *Flying Laptop* in minimum and maximum drag attitude.

6 Simulation of collision avoidance manoeuvres using aerodynamic drag

In the following chapter the methodology behind the simulation tool for collision avoidance using aerodynamic drag is explained. Based on the previous chapters, the manoeuvre, relevant calculations and algorithms are revealed. After that, an example will be used to illustrate the usage of the tool and its separation distance predictions are compared to a numerical orbit propagation.

6.1 The manoeuvre

In Section 3.3, an analytic equation was presented, which allows the calculation of a relative in-track separation distance by the variation of a satellite's ballistic coefficient. Since the mass is constant, the ballistic coefficient can effectively be changed only by altering the satellite's attitude. Therefore, the ballistic coefficients of the *Flying Laptop* for a flight in minimum and maximum drag attitude were analysed in Section 5.2.

Typically, the *Flying Laptop*'s flight attitude is continuously changing due to different pointing requirements for Earth observations or the need to point the solar arrays towards the Sun. During conjunction screening and the orbit determination process, the JSpOC determines a mean ballistic coefficient from observations, which is used for propagation as well as conjunction analysis. Hence, it will be considered the reference value. By deliberately taking an (off-nominal) attitude with a ballistic coefficient different to the reference value (i.e., the one used for the propagation by JSpOC), a separation distance can be built up relative to JSpOC's reference trajectory. It is to note, that such a manoeuvre can, in principle, be performed by taking any specified attitude. Here, only the minimum and maximum drag attitudes are looked at, since they maximise the difference in ballistic coefficient compared to the reference value thus also maximising the achievable separation distance.

Following *Omar*'s and *Bevilacqua*'s manoeuvring strategy a CAM is performed by either attaining the minimum or maximum drag attitude (corresponding to $C_{B,max}$ and $C_{B,min}$, respectively) and holding it for time t_s . After that, the satellite returns to the nominal attitude. Here, in order to maximise the achievable separation distance the manoeuvring attitude will be held until TCA, i.e., $t_s = t_c$ and there will be no return to the nominal

attitude before TCA. In order to consider constraints, as outlined in Section 4.1, the manoeuvring phase is divided into sections. Each consists of two parts of specified durations t_1 and t_2 . During the first part, the commanded attitude is taken. During the second part, a predefined attitude is implemented to charge the batteries. Fig. 6.1 shows an exemplary timeline of such a manoeuvre with a commanded ballistic coefficient higher than the reference value. During the charging phases, the ballistic coefficient is $C_{B,2} < C_{B,ref}$, here. Since the second derivative of the angular separation between the reference and the perturbed trajectories' mean anomaly $\ddot{\varphi}$ is directly proportional to the change in ballistic coefficient, a negative value causes the first derivative of the angular separation to decrease. φ itself still increases, as long as $\dot{\varphi} > 0$ ¹. The respective courses vary depending on the actual ballistic coefficients in the different phases.

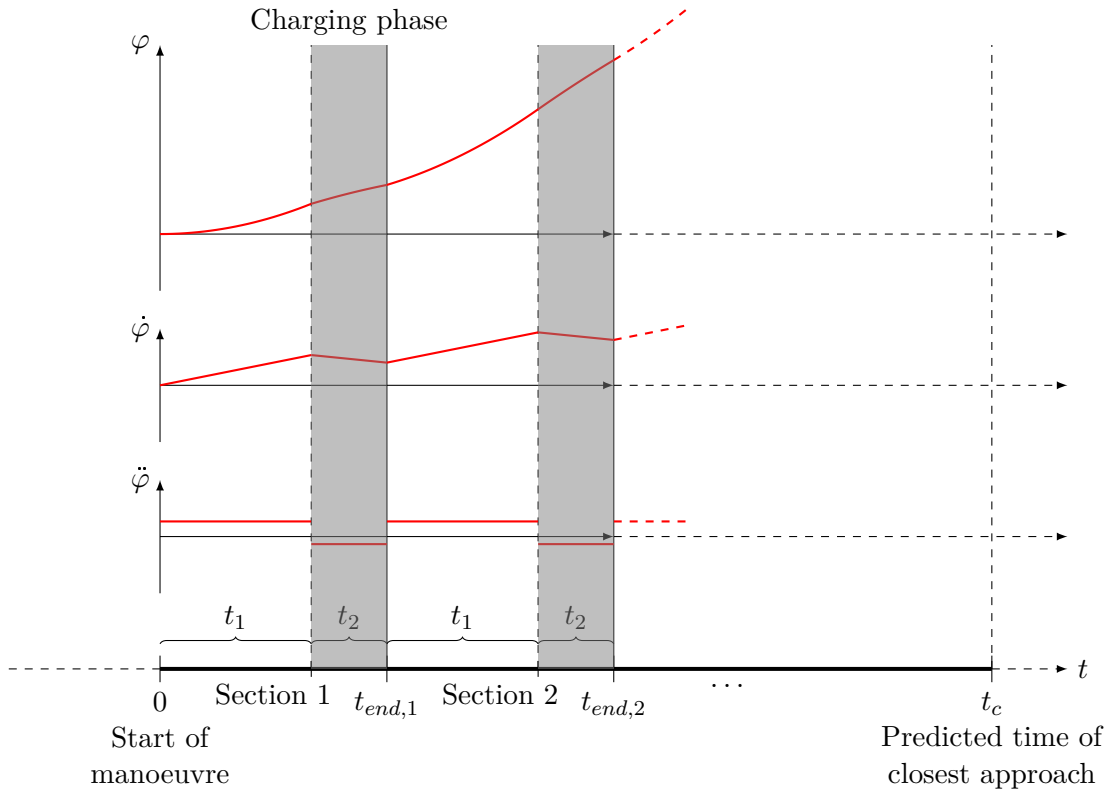


Figure 6.1 – Exemplary consideration of operational constraints on the *Flying Laptop*'s attitude. Considered is a manoeuvre with a commanded ballistic coefficient $> C_{B,ref}$ and additional phases, where pointing requirements dictate a flight with $< C_{B,ref}$. The respective evolutions of the angular separation φ between the reference and the perturbed trajectory as well as its derivatives are shown to show the influence of these phases.

6.2 The tool

The tool developed during this thesis is based upon Eq. (3.19) from *Omar and Bevilacqua* for analytically estimating an achievable in-track separation distance through a change in ballistic coefficient. Fig. 6.2 shows the tool's basic concept. Using only a CDM and

¹It is to note that the separation distance is directly proportional to φ .

pointing constraints as user inputs, the average density the satellite encounters until the predicted point of closest approach is estimated based on an obtained TLE. After that, the achievable separation distance with the analytic equation can be calculated as a function of the manoeuvring time and attitude. This leads to a new conjunction geometry and a probability of collision can thus be calculated for different possible manoeuvres. Upon evaluation of the conjunction and manoeuvre analysis, the selected manoeuvre can be converted into a command stack containing the commanded attitudes and timestamps, which can be uploaded to the *Flying Laptop*. The tool is programmed in `python` as is the operational software of the *Flying Laptop*, allowing for easier integration. It can be operated via the command line or via a Jupyter Notebook. The tool makes use of the `pyatmos` package for atmosphere modelling [50], which has been slightly adapted. Sgp4-propagation algorithms are implemented with a package developed at IRS, which itself is based on the `skyfield` package [51].

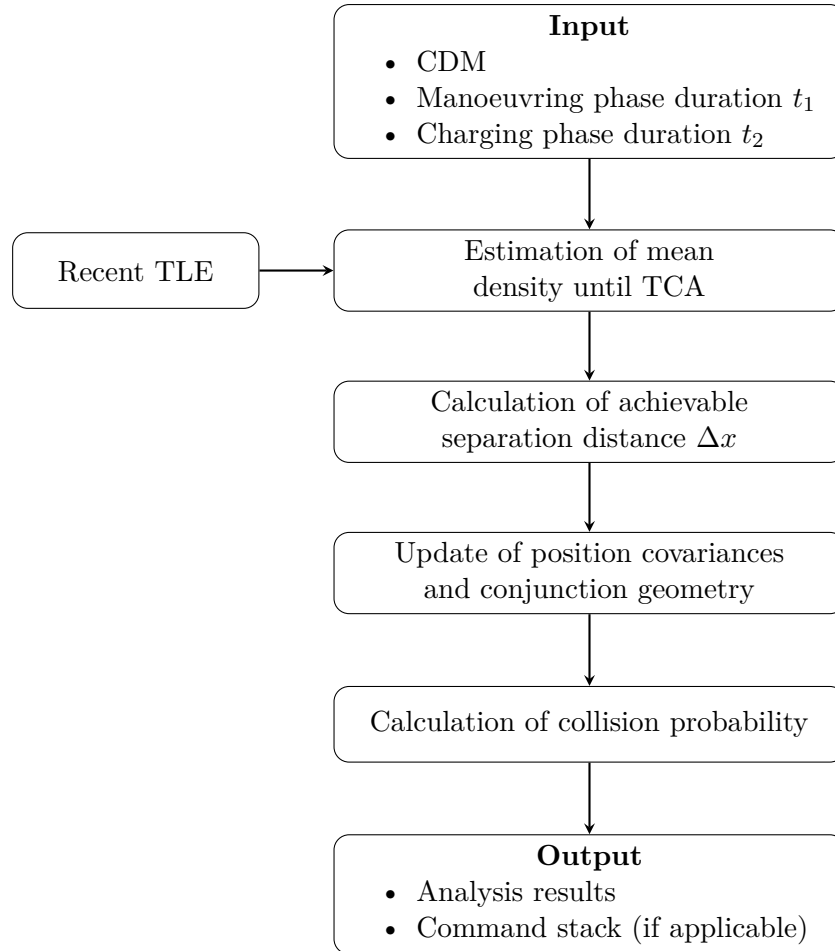


Figure 6.2 – Flowchart of the developed tool.

Loading input data

As described in Section 3.1.1, a CDM contains all the necessary information about a conjunction event and is issued when one is detected. The CDM obtained by the JSpOC

serves as primary input for the tool. Besides the predicted conjunction geometry and the associated uncertainties, especially the *Flying Laptop*'s reference ballistic coefficient $C_{B,ref}$ is of interest to examine a potential avoidance manoeuvre. Furthermore, the orbital data of both objects are also contained in the CDM of which the semi-major axis a_0 of the *Flying Laptop* is needed. Since a rough propagation of the *Flying Laptop* until t_{ca} is needed for further calculations, a current TLE is loaded from the *Flying Laptop* telemetry database as well. If desired, it can instead be loaded from space-track.org² as well.

Density estimation

The achievable separation distance during a specified interval depends on the average density the *Flying Laptop* will encounter. To estimate the average atmospheric density during the manoeuvre, an atmospheric model considering the current solar and geomagnetic activity is evaluated at a number of points along the *Flying Laptop*'s reference trajectory. A recent TLE is propagated for this using the sgp4-algorithm. The deviation in position due to the manoeuvre is considered negligible here, since it is small and only occurs in the horizontal plane and thus only minimally affects the density output (cf. Section 6.4).

The averaged density $\bar{\rho}$ then results from the evaluation of the chosen atmospheric model at n evenly-distributed time steps t_i :

$$\bar{\rho} = \frac{1}{n} \sum_{i=1}^n \rho(\mathbf{r}_i, t_i, \mathbf{K}_i) \quad (6.1)$$

where \mathbf{r}_i denotes the satellite's position and \mathbf{K}_i the space-weather indices for the atmosphere model at time step t_i .

The density models introduced in Section 2.4 are all implemented. As the JSpOC uses a version of the JB-2008 model, this model will be used unless specified otherwise. The implemented package `pyatmos` retrieves recent space-weather data from *Space Environment Technologies*'s website [52]. The indices for solar activity are updated on a daily basis, whereas the geomagnetic index is updated 3-hourly.

Calculation of achievable separation distance

Based on the look-up table created in Chapter 5 the ballistic coefficients for maximum drag, nadir-pointing, as well as minimum drag attitude are determined. For this, the solar and geomagnetic activity data obtained in the previous steps are used to gain the values of the ballistic coefficients via trilinear interpolation. The achievable separation distance is then calculated for a manoeuvre with maximum and minimum drag. For clarity, the manoeuvring ballistic coefficient will in the following be referred to as C_B . The respective calculations are performed for both manoeuvring attitudes.

²Here, the 18th Space Defense Squadron publishes TLEs obtained through own observations.

As mentioned before, the manoeuvre is divided into sections (cf. Fig. 6.1) with $\dot{\varphi}(t = 0) = \varphi(t = 0) = 0$. For a section i , the separation distance at the end of the phase can be calculated as follows. The second derivative $\ddot{\varphi}$ of the angular difference between the mean anomaly of the reference and manoeuvring trajectory is constant within each of the two parts of the section:

$$\ddot{\varphi}_{1,i} = \frac{3\bar{\rho}\mu_E}{2a_0^2} (C_B - C_{B,ref}) \quad (6.2)$$

$$\ddot{\varphi}_{2,i} = \frac{3\bar{\rho}\mu_E}{2a_0^2} (C_{B,nadir} - C_{B,ref}) \quad (6.3)$$

In the charging phases a flight in nadir-pointing is assumed. The first derivative $\dot{\varphi}$ is a piecewise linear function of gradient $\ddot{\varphi}$. It follows through integration over time:

$$\begin{aligned} \dot{\varphi}_{1,i}(t) &= \ddot{\varphi}_{1,i} \cdot [t - t_{end,i-1}] \\ &+ \dot{\varphi}_{2,i-1}(t_{end,i-1}) \end{aligned} \quad (6.4)$$

$$\begin{aligned} \dot{\varphi}_{2,i}(t) &= \ddot{\varphi}_{2,i} \cdot [t - (t_{end,i-1} + t_1)] \\ &+ \dot{\varphi}_{1,i}(t_{end,i-1} + t_1) \end{aligned} \quad (6.5)$$

Finally, the angular separation of the mean anomalies can be obtained via another integration over time, yielding

$$\begin{aligned} \varphi_{1,i}(t) &= \frac{1}{2} \ddot{\varphi}_{1,i} \cdot [t - t_{end,i-1}]^2 \\ &+ \dot{\varphi}_{2,i-1}(t_{end,i-1}) \cdot [t - t_{end,i-1}] \\ &+ \varphi_{2,i-1}(t_{end,i-1}) \end{aligned} \quad (6.6)$$

$$\begin{aligned} \varphi_{2,i}(t) &= \frac{1}{2} \ddot{\varphi}_{2,i} \cdot [t - (t_{end,i-1} + t_1)]^2 \\ &+ \dot{\varphi}_{1,i}(t_{end,i-1} + t_1) \cdot [t - (t_{end,i-1} + t_1)] \\ &+ \varphi_{1,i}(t_{end,i-1} + t_1) \end{aligned} \quad (6.7)$$

$\varphi_2(t_c)$ at the end of the last section then is the desired separation, which can be translated into a separation distance via Eq. (3.20).

If no charging phases are considered, the resulting separation distance follows as

$$\Delta x = -\frac{1}{2} \ddot{\varphi} t_s^2 = \frac{3\rho\mu_E}{4a_0} (C_B - C_{B,ref}) t_c^2 \quad (6.8)$$

The influence of uncertainties in the parameters of Eq. (6.8) can be evaluated by applying a Gaussian error propagation [53]. The standard deviations of the averaged density, the semi-major axis, the difference in ballistic coefficient and the manoeuvring time are denoted as $\sigma_{\bar{\rho}}$, σ_{a_0} , $\sigma_{\Delta C_B}$, and σ_{t_c} , respectively. The resulting standard deviation of the

separation distance can be calculated by

$$\sigma_{\Delta x} = \sqrt{\left(\frac{\partial \Delta x}{\partial \bar{\rho}} \sigma_{\bar{\rho}}\right)^2 + \left(\frac{\partial \Delta x}{\partial a_0} \sigma_{a_0}\right)^2 + \left(\frac{\partial \Delta x}{\partial \Delta C_B} \sigma_{\Delta C_B}\right)^2 + \left(\frac{\partial \Delta x}{\partial t_c} \sigma_{t_c}\right)^2} \quad (6.9)$$

where the partial derivatives with respect to one parameter are to be evaluated with the other parameters set to their nominal value. The uncertainty in separation distance leads to an additional uncertainty σ_T of the *Flying Laptop*'s position in the direction of flight. With the assumption that the additional uncertainty is uncorrelated to the uncertainty stated in the CDM $\sigma_{T,CDM}$ ³, they can be added:

$$\sigma'_T = \sigma_T + \sigma_{\Delta x} \quad (6.10)$$

σ_T is the updated transverse position uncertainty, which will be used to calculate the collision probability in the next step.

Calculation of collision probability

An avoidance manoeuvre changes the conjunction geometry. Therefore, a new point of closest approach has to be determined considering the perturbed trajectory of the *Flying Laptop*. Afterwards, the collision probability is calculated with the Foster-1992 method, as described in Section 3.1.2. All assumptions mentioned there apply.

Assuming linear satellite motion during the encounter, the position of the manoeuvring *Flying Laptop* at the original time of closest approach t_{ca} can be determined by regarding the built-up separation distance:

$$\mathbf{r}'_1(t_{ca,CDM}) = \mathbf{r}_1 + \Delta x \frac{\mathbf{v}_{1,tca}}{|\mathbf{v}_{1,tca}|} \quad (6.11)$$

Based on this, a new time of closest approach may be determined by finding the minimum distance between the objects over time:

$$t'_{ca} = t \Rightarrow |\Delta \mathbf{r}| = |\mathbf{r}_2 - \mathbf{r}'_1| = |\mathbf{r}_{2,tca} + t \cdot \mathbf{r}_{2,tca} - \mathbf{r}'_{1,tca} - t \cdot \mathbf{r}_{1,tca}| \text{ is minimum} \quad (6.12)$$

The elements of the covariance matrix describing the position uncertainty of the *Flying Laptop* is updated according to

$$C'_{RTN,1,i,j} = \begin{cases} \sigma'_T = (\sigma_T + \sigma_{\Delta x})^2 & , i = j = 1 \\ C_{RTN,1,i,j} & , \text{ else} \end{cases} \quad (6.13)$$

Together with the updated time and point of closest approach, a probability of collision may be calculated employing Eq. (3.5).

³Uncertainties in the CDM predicted position do affect the uncertainty of the semi-major axis. This is neglected here, since the uncertainties in radial and cross-track directions are usually small.

6.3 Example: Conjunction from 2022/04/07

As an example, a close conjunction of the *Flying Laptop* with an OneWeb satellite on April 7, 2022, will be examined. The full CDM is included in Appendix A. For simplicity, no additional uncertainties are included at this point.

In the observed time interval, the solar and geomagnetic activity were low to moderate. The resulting atmospheric density along the trajectory estimated with the JB-2008 model can be seen in Fig. 6.3. In a first step, the achievable separation distance for the *Flying Laptop* is determined depending on the manoeuvre duration t_c . As can be seen in Fig. 6.4, the achievable separation distance with a flight in maximum drag attitude turns out larger than with a flight in minimum drag attitude.

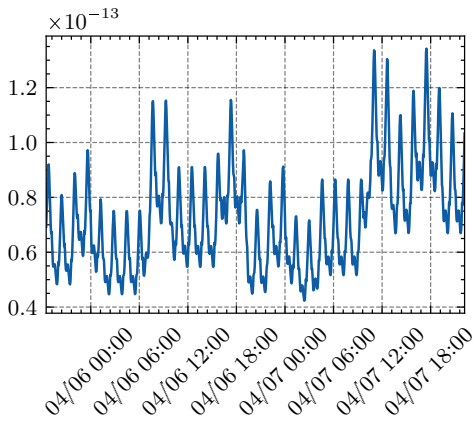


Figure 6.3 – Estimated density along the trajectory.

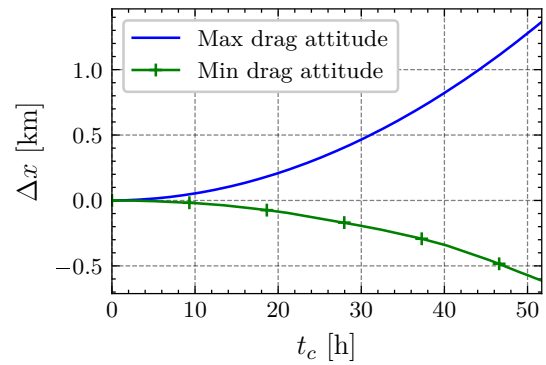


Figure 6.4 – Achievable separation distance depending on the available time to closest approach.

The miss distance resulting from a manoeuvre of duration t_c is presented in Fig. 6.5. A flight in maximum drag for 51.71 h attitude leads to a miss distance of 2318 m, which is an increase by 204.6 % compared to the JSpOC prediction without CAM. A flight in minimum drag attitude, however, causes the miss distance to shrink to 154 m for the longest possible manoeuvre duration. This settles down in the collision probability, shown in Fig. 6.6. For a manoeuvre involving flight with maximum drag, the collision probability can be reduced by a factor of 1.911. A minimum drag manoeuvre increases the probability of a collision.

Fig. 6.7 depicts the conjunction geometry in the collision plane for the different manoeuvres. Compared to the predicted situation without manoeuvre, a flight in maximum drag configuration for i.e., $t_s = 51.71$ h increases the miss distance so that the *Flying Laptop* is outside of the combined 1σ -covariance ellipsoid centred at the secondary object. On the other hand, a minimum drag manoeuvre decreases the miss distance, as previously outlined. Note that the orientation of the conjunction plane in space changes due to a manoeuvre. This leads to different projected covariance ellipses, although the 3-dimensional combined covariance ellipsoid does not change (no additional uncertainties were considered).

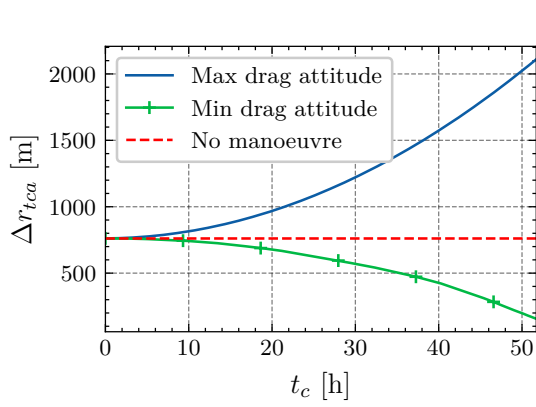


Figure 6.5 – Miss distance depending on the available time to closest approach.

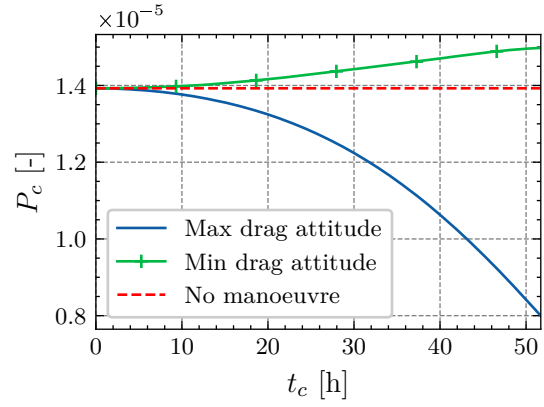
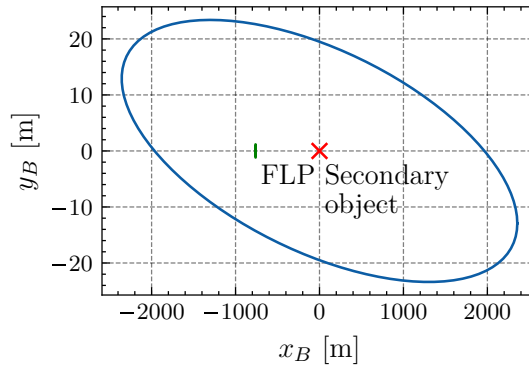
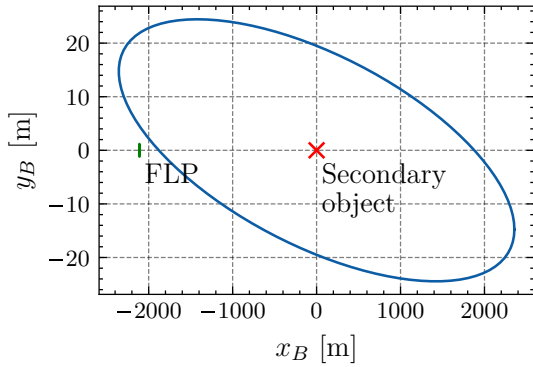


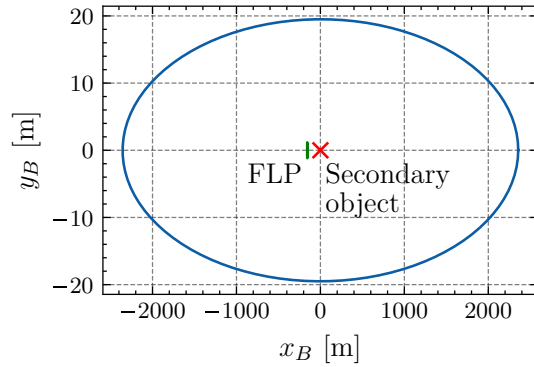
Figure 6.6 – Probability of collision depending on the available time to closest approach.



(a) No manoeuvre, predicted situation.



(b) Situation resulting from a flight in maximum drag configuration for $t_s = 51.71$ h.



(c) Situation resulting from a flight in minimum drag configuration for $t_s = 51.71$ h.

Figure 6.7 – Comparison of the conjunction geometry in the conjunction plane. The 1σ -covariance ellipsoid is shown in blue. The collision area is centred at the *Flying Laptop*'s position (FLP). It is to note that its circular shape is not recognizable due to axes scaling.

6.4 Verification

To assess the accuracy of the analytically predicted separation distance a high-fidelity numerical orbit propagation is performed using the commercial software ASTOS (AeroSpace

Trajectory Optimization Software) [54]. The obtained separation distances are then compared.

The initial values for both the numerical propagation as well as the estimation via the tool are taken from a TLE for the *Flying Laptop* of epoch April 4, 2022, 01:42 UTC:

```
1 42831U 17042G 22094.07142843 .00001451 00000-0 14962-3 0 9994
2 42831 97.4330 312.8212 0012442 255.6029 104.3838 14.91603896257005
```

Densities are obtained using the NRLMSISE-00 model at moderate solar and geomagnetic activity, both for the analytic calculation as well as in ASTOS. As reference trajectory a flight in minimum drag attitude is assumed with $C_{B,ref} = 1.214 \times 10^{-2} \text{ m}^2 \text{ kg}^{-1}$, whereas the satellite has a ballistic coefficient of $C_B = 3.262 \times 10^{-2} \text{ m}^2 \text{ kg}^{-1}$ in manoeuvring attitude with maximum drag. In ASTOS, perturbations of the Earth's gravitational field are considered via the zonal harmonics J_2 , J_3 , and J_4 . Both trajectories are simulated in ASTOS for 5 days. The resulting separation distance is calculated as the in-track component of the relative position vector between both trajectories in the RTN-system of the reference trajectory. Simultaneously, the analytic equation is used to calculate the achievable separation distance.

In Fig. 6.8, the results are compared. After 5 days the difference in separation distances is 0.3911 km, i.e., 1.406 %. This shows that the assumptions made in the derivation of the analytic equation do not lead to remarkable errors. Further, the functionality of the tool including density averaging and relative separation distance calculation is confirmed.

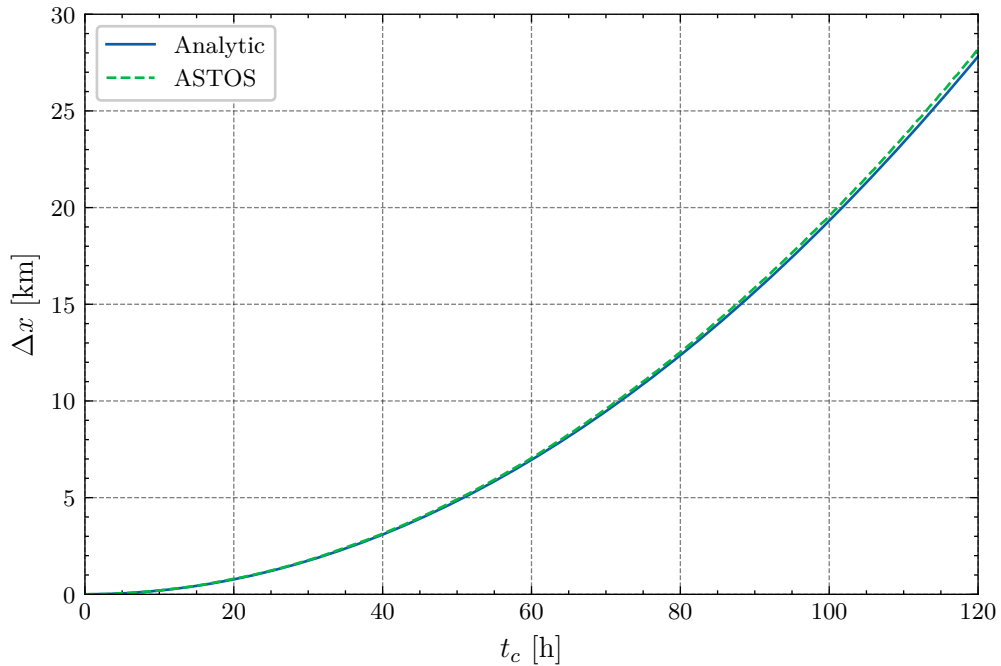


Figure 6.8 – Comparison of separation distances obtained via analytic equation and via a high-fidelity orbit propagation in ASTOS.

7 Analyses

This chapter presents the results of analyses performed with the previously presented tool. It aims to investigate collision avoidance using aerodynamic drag more closely on the example of the *Flying Laptop*. Therefore, the tool's predicted separation distances are compared to flight data. Afterwards, achievable separation distances are investigated and finally, the influence of parameter uncertainties on the collision probability is analysed.

7.1 Comparison with flight data

On October 29, 2017, the *Flying Laptop* performed a 24-hour nadir-pointing before going back to normal operation, i.e., no specified attitude for longer durations. Therefore, the change in attitude at the end of the nadir-pointing will lead to a separation distance compared to a reference trajectory of the satellite flying further in nadir-pointing. This separation distance will in the following be compared to the analytic estimation.

During the nadir-pointing, a TLE has been created by JSpOC with epoch October 29, 2017, 09:58:17 UTC. The propagated positions of this TLE will in the following be assumed as a reference trajectory to compare it with GPS data over a course of 7 days. The ballistic coefficient of the satellite in nadir-pointing attitude has been determined in Chapter 5. For the given interval (and considering solar and geomagnetic activity), it is $C_{B,ref} = 0.01418 \text{ m}^2 \text{ kg}^{-1}$. The ballistic coefficient of the flight phase after the nadir-pointing is taken from a CDM for a close encounter on November 13, 2017,¹ and set to be $C_B = 0.02373$. Based on these ballistic coefficients, the presented tool is used in order to estimate the achievable separation distance. Since the ballistic coefficient after the nadir-pointing is higher, a positive separation distance builds up. At the same time, GPS positions from the *Flying Laptop* are compared to the sgp4-propagated reference trajectory and their in-track separation is determined.

Fig. 7.1 shows the resulting separation distances building up after the end of the nadir-pointing. The graph of the separation between GPS positions and the propagated orbit of the TLE is noisy but a separation distance in positive direction can clearly be seen. It grows to almost 20 km in the observed 7 days. The analytically estimated separation making use of the NRLMSISE-00 atmosphere model is significantly smaller than the separation between GPS positions and sgp4-propagation, measuring only 3.453 km. It was,

¹The time interval used by JSpOC for orbit determination was 2017/11/06 00:26:57 to 2017/11/07 00:26:57.

however, found that the *Atmospheric Density Estimate for Drag Calculation* (ATMDEN) service forecasted a higher density for the observed period. The service employs a drag temperature model for estimating atmospheric densities and issues density estimates depending on height, as well as latitude and longitude. Using the obtained density values by ATMDEN for October 31, 2017, the separation distance estimated by the tool fits well to the observed separation between GPS positions and sgp4-propagation.

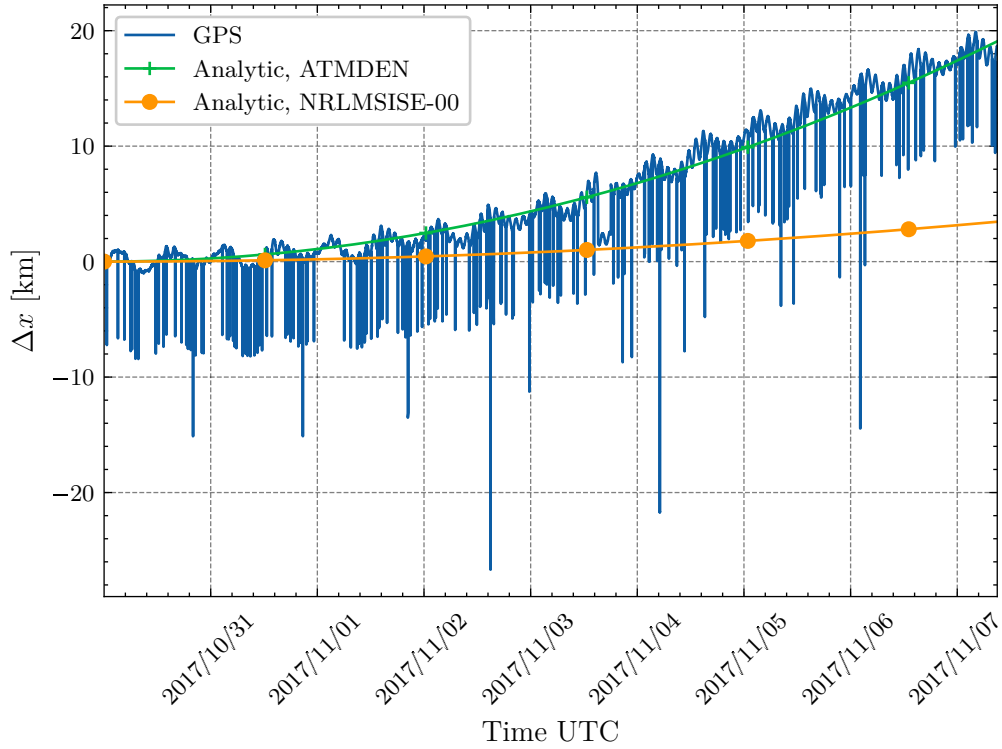


Figure 7.1 – Comparison of the separation distance relative to the reference trajectory obtained through GPS data and sgp4-propagation of a TLE and through the analytic equation for the flight test case in October, 2017.

Another flight test was conducted between noon of September 5 and noon of September 9, 2022. The *Flying Laptop* was commanded to take and hold a maximum drag attitude for the entire 4 days. Again, the propagation of a TLE was planned to be used as a reference trajectory and compared to the actual GPS positions. However, the *Flying Laptop* was not able to perform this manoeuvre due to the battery monitoring software prompting the satellite to turn into safe-mode. In a next attempt, the satellite was commanded to hold maximum drag attitude for 4 h and then re-charge its batteries by pointing the solar arrays to the Sun for 30 min. This was implemented and actually performed by the satellite starting on September 7, 2022, 20:00. Although the intermittent Sun-pointing clearly helped the satellite to generate more power, the batteries seemed to de-charge slowly until the satellite finally switched to safe-mode again on September 8, 2022, 15:00. The manoeuvring time was therefore very short with only 19 h.

The flight test may be examined similar to the previous analysis, though. A TLE from JSpOC with an epoch of September 8, 2022, 13:34:29 UTC is propagated for 5 days and

viewed as a reference trajectory. Again, in-track separation distances to the actual GPS positions are computed for every timestep. The reference ballistic coefficient is the value for the flight in maximum drag configuration $C_{B,ref} = 0.03371 \text{ m}^2 \text{ kg}^{-1}$. In the following phase, the ballistic coefficient is smaller with $C_B = 0.01773 \text{ m}^2 \text{ kg}^{-1}$ and taken from a CDM generated for a close encounter on September 19, 2022². With the tool, a separation distance is estimated based on the actual space weather data and using the NRLMSISE-00 model. Fig. 7.2 shows the results from this analysis. The expected negative separation distance due to a decrease in ballistic coefficient is observable in the GPS data when compared to the reference trajectory. With a separation of $\Delta x = -2.360 \text{ km}$ after 5 days it amounts to only 27.11 % of the estimated separation distance of -8.706 km .

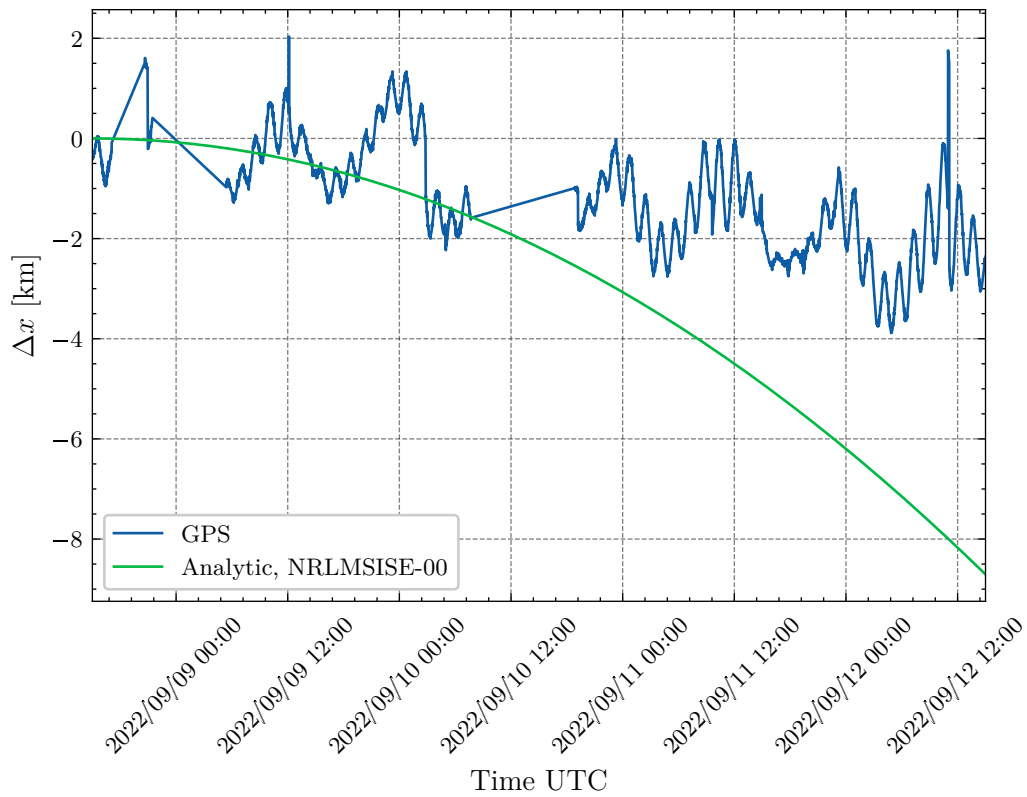


Figure 7.2 – Comparison of the separation distance relative to the reference trajectory obtained through GPS data and sgp4-propagation of a TLE and through the analytic equation for the flight test in September, 2022.

7.2 Achievable separation distance

In this section, the maximum separation distance of the *Flying Laptop* achievable via a change in ballistic coefficient is examined. The reference trajectory is based on a CDM received for a close encounter on 2022/04/07 (cf. Appendix A), while different levels of solar and geomagnetic activity are assumed. The reference ballistic coefficient is $C_{B,ref} = 0.01794 \text{ m}^2 \text{ kg}^{-1}$, which is the average of recent CDMs, as determined in Section 3.4. The

²The time interval used by JSpOC for orbit determination was 2022/09/17 14:38:48 - 2022/09/18 14:38:48.

ballistic coefficients of the minimum and maximum drag attitude are calculated by the tool as described in Section 6.2. Solar and geomagnetic data for the different activity levels are defined as in Table 2.2, the used atmosphere model is NRLMSISE-00. The density is evaluated and averaged over one orbital period of the reference orbit. The resulting values are $\bar{\rho} = 1.158 \times 10^{-14} \text{ kg m}^{-3}$ for low, $\bar{\rho} = 1.650 \times 10^{-13} \text{ kg m}^{-3}$ for moderate and $\bar{\rho} = 1.020 \times 10^{-12} \text{ kg m}^{-3}$ for high activity.

The tool is now used to analytically estimate the achievable separation distance for a given manoeuvring time. During the manoeuvre, no return to the nominal ballistic coefficient is assumed. This leads to an estimation of the maximum achievable miss distance in a given time. The results are presented in Fig. 7.3. The positive separation distances are established by a flight with increased ballistic coefficient. Consequently, a decreased ballistic coefficient allows for the build-up of negative separation distances. Further, the achievable separation distance grows linearly with increasing atmospheric density part from the influence of the density on the ballistic coefficient (cf. Eq. (3.20)). For low solar and geomagnetic activity, the resulting low density causes the separation distance turns out negligibly small at only 1.465 km for a flight in maximum drag attitude and even smaller for a flight with minimum drag. At moderate activity, the separation distances are noticeably higher at 19.35 km and -7.647 km , respectively. For a high level of activity, the separation distances grow up to 119.4 km and -46.81 km .

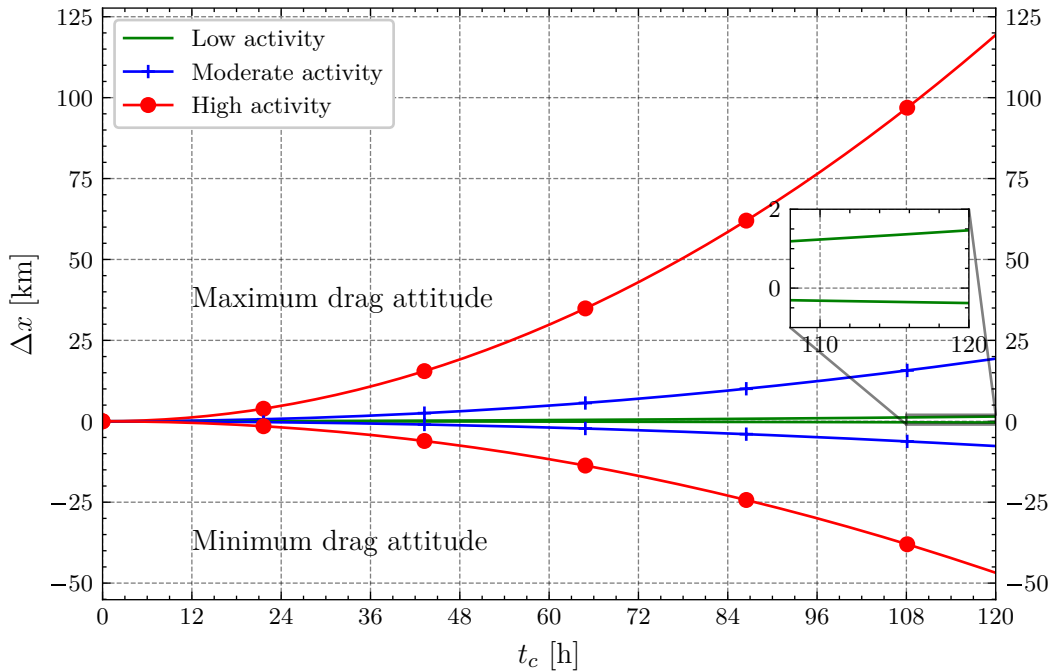


Figure 7.3 – Achievable separation distance of the *Flying Laptop* for different levels of solar and geomagnetic activity.

Next, the effect of additional constraints on the achievable separation distance shall be evaluated. The scenario is the flight in maximum drag attitude for the manoeuvre mentioned before at moderate solar and geomagnetic activity. Additionally, phases in which the *Flying Laptop* points to the Sun in order to re-charge are now taken into account.

Therefore, the manoeuvring time is divided into individual sections of 4 h duration consisting of two parts. In the first phase, the satellite takes the commanded attitude (for maximum drag, here), while in the second a nadir-pointing is performed³. The duration of each phase is varied adding up to 4 h. Fig. 7.4 shows the resulting achievable separation distances depending on the available time. If no charging phase is carried out (4 h/0 h), the separation distance is equal to the one for moderate activity and maximum drag in Fig. 7.3. For longer charging phases, the achievable separation distance decreases. It does, however, still develop monotonously. For a manoeuvre involving sections of 1 h flight in maximum drag attitude followed by 3 h of charging, the effects of both phases almost cancel out. If the charging phase is commanded even longer in relation to the first phase, the separation distance becomes negative, due to the ballistic coefficient in nadir-pointing being smaller than the reference ballistic coefficient. As can be seen in Fig. 7.5, the ratio between the separation distance for considered charging phases and the separation for no charging phases, levels off at fractions slightly smaller than the ratio between the maximum drag phase duration and the total section duration.

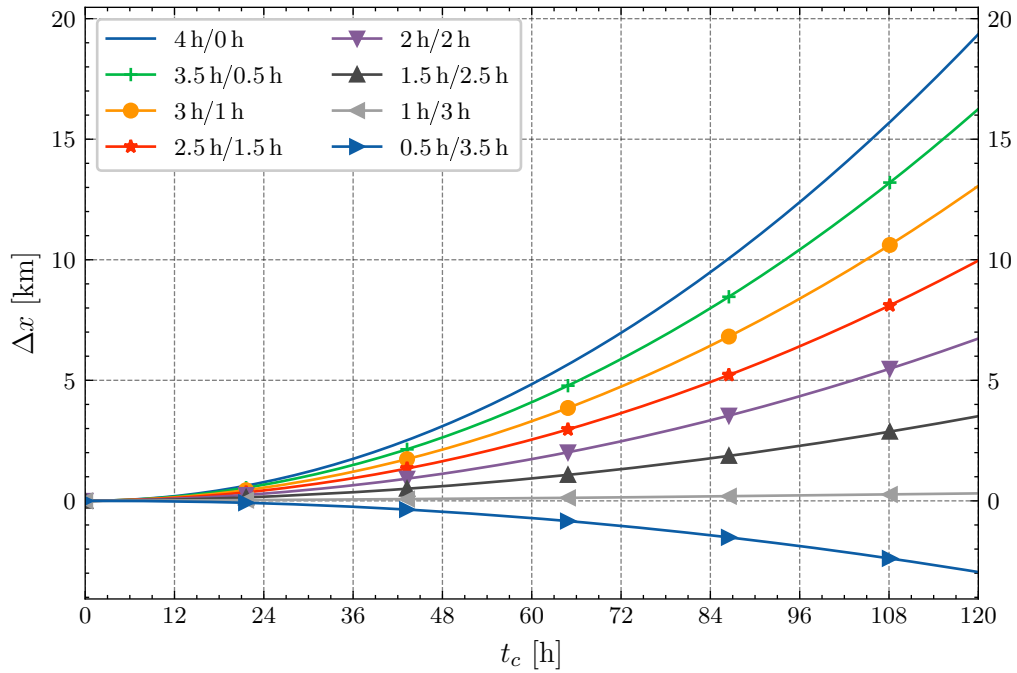


Figure 7.4 – Achievable separation distance of the *Flying Laptop* for different constraints and moderate solar and geomagnetic activity. The constraints consider a manoeuvring and charging phase of variable duration, e.g., 3 h/1 h is a flight in maximum drag attitude for 3 h, followed by a charging phase of 1 h.

³The nadir-pointing is currently used for re-charging the satellite batteries, since the absolute value of the angle between the Sun vector and the orbital plane is close to 90°.

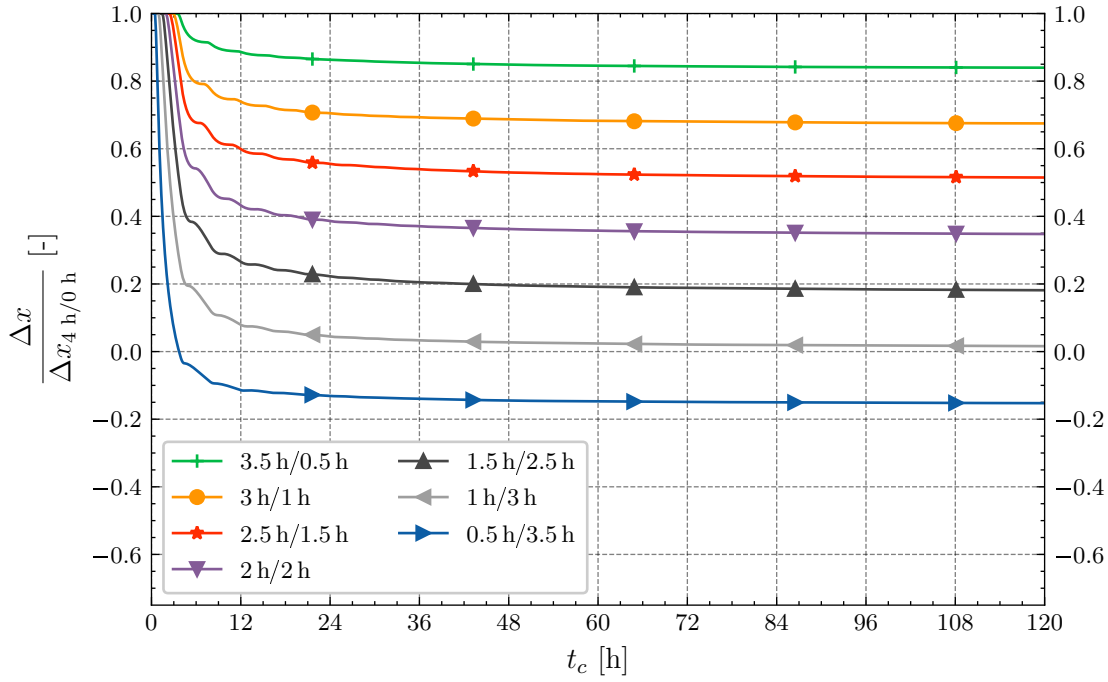


Figure 7.5 – Ratio of achievable separation distance of the *Flying Laptop* for different constraints compared to no constraints. Moderate solar and geomagnetic activity are assumed.

7.3 Influence of parameter uncertainties

Uncertainties in the parameters of the analytic equation for the achievable separation distance lead to additional in-track position uncertainties at the time of closest approach. The effect of these uncertainties on the collision probability will be examined based on the exemplary close encounter of the *Flying Laptop* on April 7, 2022. The reasonable CAM in this case is a flight in maximum drag configuration, therefore this manoeuvre will be chosen. The manoeuvring time t_c will be varied (10 h, 20 h, 30 h, 40 h, and 50 h). For simplicity, no further constraints on the manoeuvre will be considered.

The additional in-track uncertainty can be expressed as a scaling factor for the respective element of the covariance matrix of the *Flying Laptop* at t_{ca} . The updated covariance matrix follows as

$$\mathbf{C}'_{1,tca} = \begin{bmatrix} \sigma_{R,1}^2 & 0 & 0 \\ 0 & k^2 \cdot \sigma_{T,1}^2 & 0 \\ 0 & 0 & \sigma_{N,1}^2 \end{bmatrix} \quad (7.1)$$

$$\text{with: } k = \frac{\sigma_{T,1} + \sigma_{\Delta x}}{\sigma_{T,1}} \quad (7.2)$$

First, the influence of the scaling factor k on P_c will be quantified. Afterwards, it will be examined how uncertainties in the different parameters translate into k .

In Fig. 7.6, the resulting collision probability is plotted over k for different manoeuvring times. For $k = 1$, the collision probabilities are equal to the ones presented in Fig. 6.6,

since no scaling of the covariance matrix is performed. For a growing scaling factor, the collision probability tends to decrease monotonously for the manoeuvring times up to 40 h. The longest manoeuvre duration of 50 h, however, shows a maximum collision probability, which is reached for $k = 1.361$. This means that parameter uncertainties in the analytic equation, which cause the in-track covariance to grow by 36.1 %, in fact lead to an increased collision probability compared to when neglecting the parameter uncertainties. It becomes evident as well, though, that the resulting collision probability is still below the one without manoeuvre.

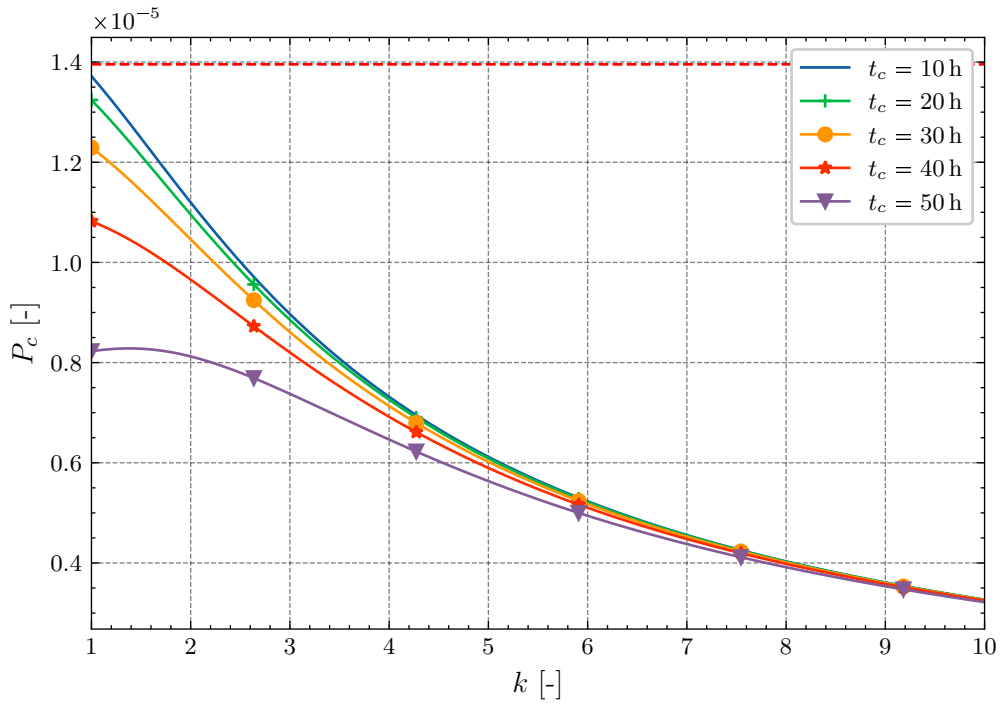


Figure 7.6 – Collision probability over in-track covariance scaling factor. In red and dashed is the collision probability for no manoeuvre.

Fig. 7.7 depicts the scaling factor depending on the uncertainties in the parameters $\bar{\rho}$, a_0 , ΔC_B or t_c for a manoeuvring time of $t_c = 50$ h. Due to the first three parameters all entering the analytic equation (Eq. (3.20)) linearly, they show the same influence. t_c shows an impact, which is stronger by a factor of 2. It can be concluded that an uncertainty in any one of the atmospheric density, the semi-major axis, or the ballistic coefficient difference of 10.10 % causes P_c to become maximum. For the uncertainty in the manoeuvring time t_c , this is the case at 5.051 %.

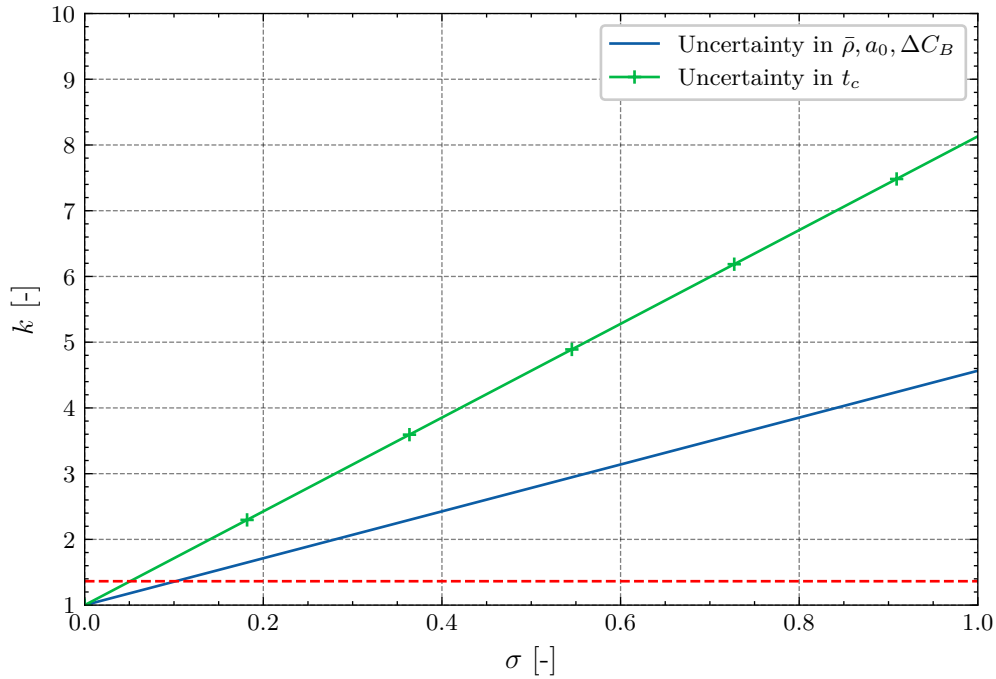


Figure 7.7 – In-track covariance scaling factor depending on uncertainty in the parameters of the analytic equation. The manoeuvring time is $t_c = 50$ h. The scaling factor, for which P_c becomes maximum, is marked in red and dashed.

7.4 Influence of relative in-track position at TCA

To study the effects of the predicted conjunction geometry on possible manoeuvres, two past close encounters are compared in the following section. The first is the close encounter on April 7, 2022, 22:11:49 UTC (cf. Appendix A), while the second is a close encounter on March 30, 2022, 15:56:03 UTC (ID 262608487). The two conjunctions differ with regards to the in-track component of the predicted relative position, which is negative for encounter 1 and positive for encounter 2. This can be seen in Fig. 7.8.

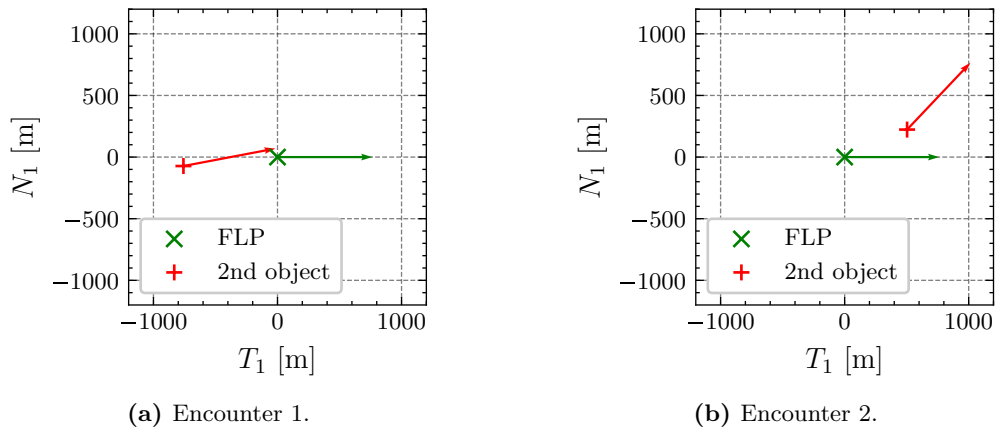


Figure 7.8 – Predicted conjunction geometries at TCA in the local horizontal plane of the *Flying Laptop*. Velocities are scaled by a factor of 0.1.

A maximum manoeuvring time for both scenarios is assumed to be 5 days. The resulting achievable separation distances are presented in Fig. 7.9. For both encounters, the achievable separation distance in maximum drag attitude is higher.

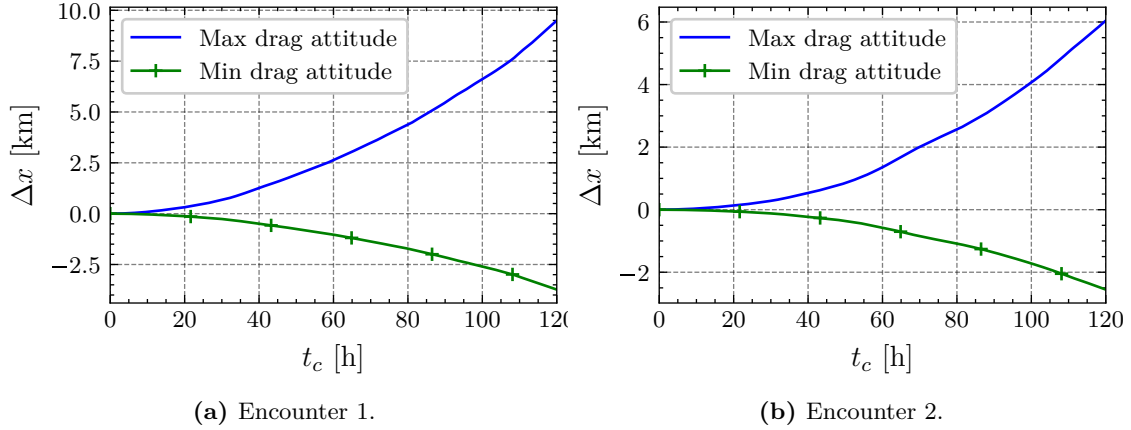


Figure 7.9 – Achievable separation distances for both encounters depending on manoeuvring time.

The miss distances at TCA shall be evaluated more carefully. For the first encounter a flight in maximum drag attitude increases the miss distance monotonously up to 13.30 times the predicted miss distance of 761.0 m. A minimum drag manoeuvre, however, leads to a shrinking miss distance for shorter manoeuvre times. Flying in minimum drag attitude for 50.69 h before TCA minimizes the miss distance to yield only 1.964 m. This is the result of an achieved separation distance which corresponds to the in-track relative position component in the predicted conjunction geometry (cf. Fig. 7.8). For longer manoeuvre durations and therefore higher absolute separation distances the minimum drag manoeuvre is able to increase the miss distance as well. For a minimum drag manoeuvre lasting the whole 5 days a miss distance of 2.924 km can be achieved, which is an increase by 283.9% compared to the original prediction. Looking at scenario 2, the situation is different. Here a minimum drag manoeuvre leads to a monotonously increasing miss distance of up to 2.868 km compared to the 554.1 m that were originally predicted. On the other hand, a flight in maximum drag attitude for 42.64 h minimizes the miss distance to only 61.72 m, i.e., 11.14% of the miss distance for no manoeuvre. However, for longer manoeuvre durations in maximum drag the miss distance increases and finally equals the achievable miss distance via minimum drag for a manoeuvring duration of 71.71 h. For even longer manoeuvres the miss distance is greater for a flight in maximum drag attitude.

In order to compare risk associated with the manoeuvres the maximum collision probability is calculated according to *Alfano's* method (cf. Eq. (4.3)), as visible in Figs. 7.12 and 7.13. The aforementioned findings settle down in the collision probability as well. The increasing miss distance for a maximum manoeuvre in case 1 leads to a decreasing collision probability, whereas the minimum drag manoeuvre causes $P_{c,max,alf}$ to show a maximum at exactly the manoeuvring time minimising the miss distance. For encounter 2

it is exactly the other way round. A maximum drag manoeuvre shorter than 57.50 h leads to a maximum collision probability higher than if no manoeuvre were to be performed, thus worsening the situation. However, the growing achievable miss distances eventually lead to the fact that a manoeuvre in maximum drag attitude causes a lower maximum collision probability than a minimum drag manoeuvre.

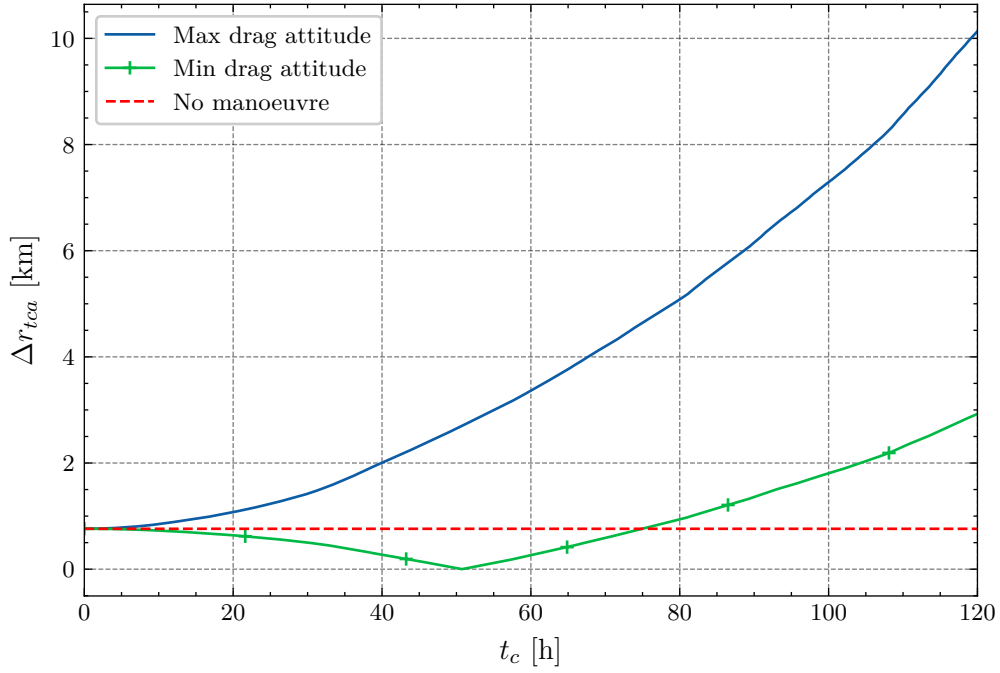


Figure 7.10 – Miss distance depending on manoeuvring time for encounter 1.

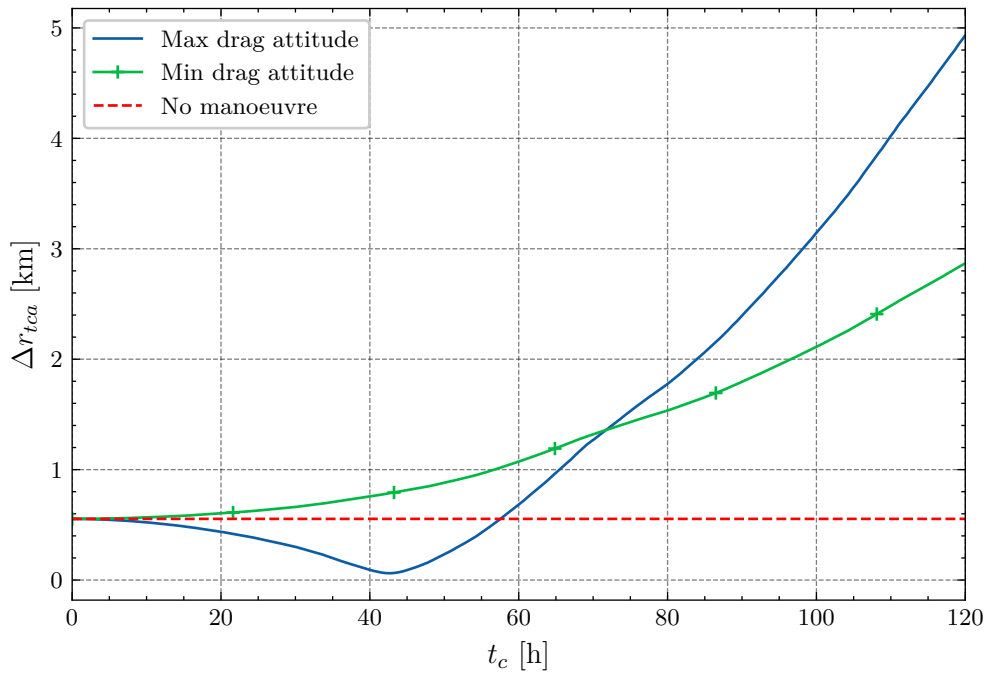


Figure 7.11 – Miss distance depending on manoeuvring time for encounter 2.

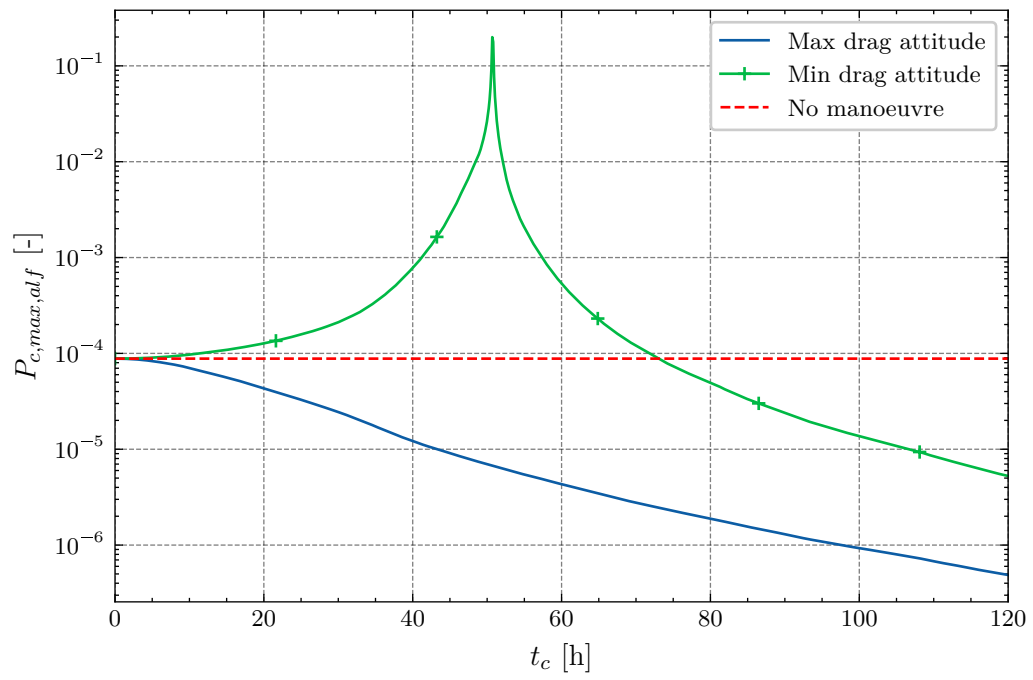


Figure 7.12 – Maximum probability of collision depending on manoeuvring time for encounter 1.

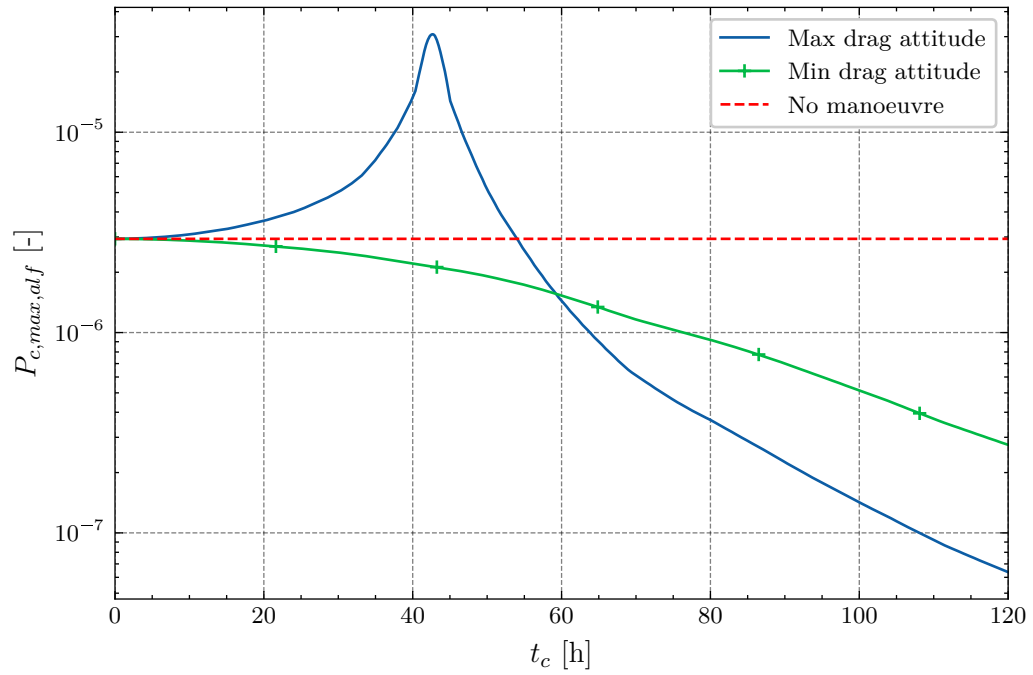


Figure 7.13 – Maximum probability of collision depending on manoeuvring time for encounter 2.

8 Discussion

In the following chapter the results of the previous analyses are discussed. At first, the feasibility of aerodynamic collision avoidance manoeuvres for the *Flying Laptop* is evaluated. After that, the effect of uncertainties is dealt with before possible manoeuvre strategies are discussed.

8.1 Feasibility

Atmospheric density is highly dependent on the activity of the Sun and Earth's geomagnetic activity. This already highlights the importance of considering current activity data when estimating effects of aerodynamic manoeuvres. By employing complex atmospheric models, recent and predicted values for the indices and proxies can be used to estimate the density on a given trajectory. In a first step, the possibility to perform CAMs depending on solar and geomagnetic activity was studied. As expected, the achievable separation distance in a given time is strongly influenced by the activity level, leading to separation distances which vary across two orders of magnitude. *Mishne* and *Edlerman* argued that for a reasonable collision avoidance manoeuvre, the achievable separation distance must be in the range of 900 m per three days in order for it to be greater than typical propagation uncertainties and thus useful [44]. It can be concluded that this separation distance can be achieved for moderate and high levels of solar and geomagnetic activity. Only for low activity, the resulting accelerations due to aerodynamic drag appear to be too low for creating significant separations. Solar activity follows approximately an 11-year cycle and the next maximum is expected for 2025 [55, 56]. Fig. 8.1 presents the course of the solar flux at 10.7 cm as proxy for the Sun's activity. This allows to make the assumption that a feasibility of aerodynamic CAMs will be feasible in the upcoming period until the next minimum in the solar cycle. During minimum phases, the feasibility may not be given when solar activity and consequently atmospheric density are low.

Considering constraints for Sun-pointing phases, i.e., charging phases, shows an influence on the achievable separation distance. It was observed, though, that even a manoeuvre, in which the *Flying Laptop* holds maximum drag attitude for 1.5 h followed by a charging phase of 2.5 h, the resulting separation distance fulfils the criterion mentioned before and can therefore be considered a useful manoeuvre. Such a constraint, however, is far beyond what is typically required for charging phases. In a performed flight test, a charging phase of 0.5 h every 4 h already allowed the *Flying Laptop* to perform a 19 h manoeuvre. It is

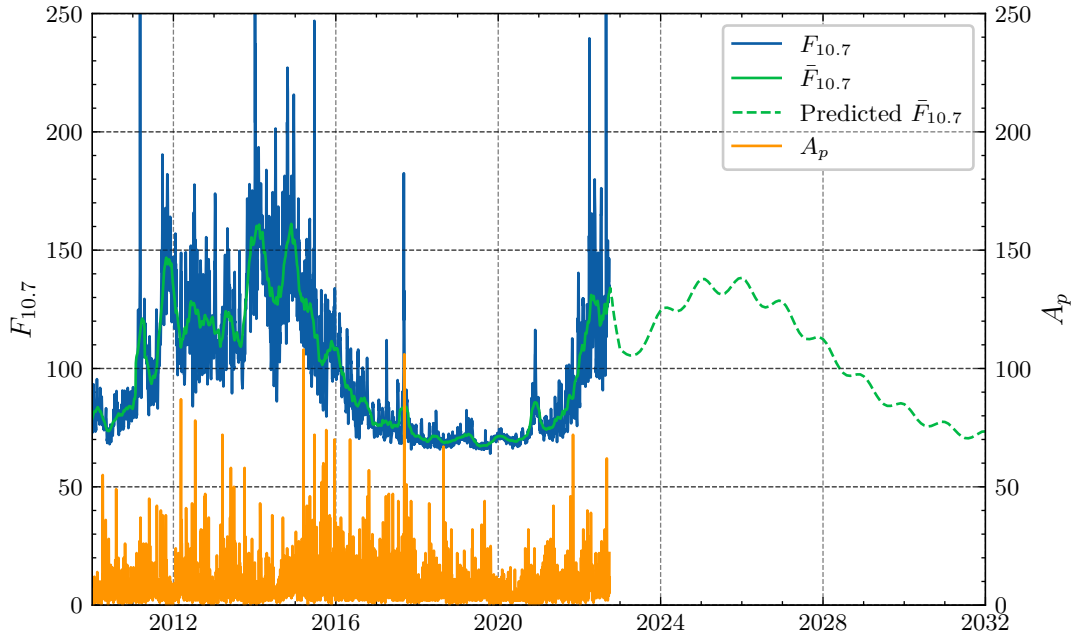


Figure 8.1 – Solar activity proxy $F_{10.7}$, its 81-day average $\bar{F}_{10.7}$ and geomagnetic activity index A_p over time. Historic and predicted data are obtained from [52].

expected that by increasing the ratio to 3.5 h flight in manoeuvring attitude and 0.5 h of charging will be sufficient for long-time manoeuvres in the current situation.

In the context of the *Flying Laptop*'s orbital evolution it is to note that the angle between the orbital plane and the Sun vector is continuously changing. The recent state demands charging phases as mentioned before when performing maximum drag manoeuvres. Minimum drag manoeuvres can be implemented without having to consider charging phases, since the satellite can be freely moved around the axis pointing to the direction of flight, such that the solar arrays can point to the Sun constantly. For a progressively decreasing local time of ascending node, this situation will change. For a LTAN around midnight (or noon, respectively), the orbital plane is oriented in a way allowing to point the solar arrays to the Sun during a maximum drag manoeuvre. In this case, charging phases were to be implemented during flights in minimum drag attitude. Looking at orbital plane orientations between these extreme cases, further tests will be necessary to determine whether enough power can be generated in the respective attitudes or whether charging phases are needed. Furthermore, tests should be performed in order to study the effects of uneven heating of the satellite structure, which may, in fact, deteriorate battery performance as well or lead to other negative effects. Still, this can be mitigated by making use of the remaining degree of freedom and commanding rotations around the direction of flight without worsening the manoeuvring performance.

Power could be saved by minimizing downlinks of the satellite, e.g., by not establishing connection to the ground station during a pass at all or by downlinking fewer data. In the flight test, it was, however, found that monitoring the satellite's telemetry data is an important point when performing collision avoidance manoeuvres. Problems with the

GPS receivers or the star trackers, for example, could potentially rob the satellite of its ability to take commanded attitudes. Since this could potentially worsen the situation at the time of closest approach, it is recommended to constantly monitor both telemetry as well as housekeeping data, like battery voltages, so that the satellite is able to perform the manoeuvre as desired.

8.2 Uncertainties in parameters

The effects of uncertainties in the parameters required for the equation to estimate the achievable separation distance were investigated on an exemplary close encounter. Uncertainties in the average density, the semi-major axis and the change in ballistic coefficient were covered. Using a linear error progression, it was calculated to which extent they affect the uncertainty in the separation distance. This uncertainty adds to the position covariance in the in-track direction as given in CDMs. For the exemplary encounter it was found that, depending on the manoeuvring time, uncertainties in the parameters affect the resulting collision probability differently. For shorter manoeuvres the collision probability strictly decreases for growing parameter uncertainties. On the other hand, the collision probability shows a maximum for a certain scaling factor of the in-track position covariance before strictly decreasing as well. The scaling factor to reach maximum collision probability translates into uncertainties of about 10 % for either averaged density, semi-major axis, or change in ballistic coefficient. Alternatively, a manoeuvring time with an uncertainty of about 5 % has the same effect. Taking into account, that these parameters are all fraught with uncertainties and that these uncertainties add up, the individual uncertainties must even be lower to maximise P_c . Looking at the individual parameters, these uncertainty levels may be assessed. Atmospheric models are typically assumed to estimate the density with an error of 20 %, thus being a major source of uncertainty in the equation. For the semi-major axis, an error of 10 % would translate into an altitude difference of several hundred kilometres, which is obviously oversized. The uncertainty in manoeuvring time may also be assumed negligible due to the fact that manoeuvring times are several hours, whereas the satellite is able to implement a commanded attitude within minutes (which, of course, must be monitored). Uncertainties in the ballistic coefficient difference are more difficult to determine, since they depend on the quality of the aerodynamic analyses and the reliability of the ballistic coefficient stated in the CDMs, which is so far not possible to assess. Additionally, pointing errors add to the uncertainty in the ballistic coefficient. Still, it becomes clear that, in the case at hand, for any additional uncertainty the collision probability is clearly lower than the one which was previously calculated in the case of not manoeuvring due to the positive impact of the increased miss distance.

The results further indicate the importance of estimating uncertainties in the parameters as realistically as possible to generate a trustworthy probability of collision. Under or over-estimating the uncertainties may lead to increased or decreased collision probabilities. For any close encounter that is to be assessed, such an analysis is recommended in order to gain

a deeper understanding of the dependencies. Still, it must be kept in mind that potential further scaling of the covariance matrices by JSpOC is another source for a variation of the collision probability. So far, the only possibility for assessing the overall risk of a close encounter is the calculation of a maximum collision probability, as e.g., given by *Alfano*, which is detached from the objects' covariances in its worst-case formulation

8.3 Manoeuvre strategies

When facing a predicted close encounter, the operators of the *Flying Laptop* so far have three options. They can either command a flight in maximum or in minimum drag attitude or do not implement any CAM. Depending on the predicted collision probability, performing a CAM and thus reducing the risk is desirable, however. In Section 7.4 it was found that for short manoeuvre durations either a minimum or a maximum drag manoeuvre lead to an increase in miss distance and thus reducing the maximum collision probability. A positive separation distance (corresponding to a flight in maximum drag attitude) is desirable if the predicted in-track component of the relative position at TCA is negative, i.e., at closest approach the secondary object is located against the *Flying Laptop*'s direction of flight. Vice versa, a negative separation distance is to be induced for a positive predicted in-track distance at TCA. For longer manoeuvre durations, though, it may be favourable to perform a contrary manoeuvre. Depending on the reference ballistic coefficient (and solar and geomagnetic activity, of course) it might be possible to implement a manoeuvre which would lead to a shrinking miss distance if performed shortly but to drastically growing miss distances for longer manoeuvring times, as was the case in encounter 2 in Section 7.4.

From this possible manoeuvring strategies might be deduced. For short-term manoeuvres with little time left until predicted TCA the attitude which monotonously increases the miss distance is to be commanded, representing a conservative. This results in a maximum drag attitude if the in-track component of the relative position of the secondary object with respect to the *Flying Laptop* is negative and a minimum drag attitude if it is positive. For long-term manoeuvres, the strategy might be inverted if an analysis of the achievable separation and miss distances indicates so. At this point in time it can, however, not be recommended to perform a manoeuvre which leads to decreasing miss distances at first. Further analyses on the accuracy of the predicted separation distances and evaluation of actually performed CAMs are necessary before such a manoeuvre might be reliably performed.

Another point was not addressed so far. For a secondary object in an orbit with a similar period to that of the *Flying Laptop* it is realistically possible for further encounters to happen several orbits before and after the predicted close encounters even though they might not be as close as the one covered in the CDM. It was so far not analysed, how an avoidance manoeuvre using aerodynamic drag affects previous or later encounters. This

is an important aspect of future research. Whether sgp4-propagation of TLEs is sufficient for a reliable simulation is difficult to assess. High-fidelity orbit propagations might lead to further insights.

9 Summary and outlook

9.1 Summary

In this thesis, a tool was developed which allows the operators' of the university satellite *Flying Laptop* to assess possible aerodynamic manoeuvres to avoid collisions. The different manoeuvres can be compared with respect to their resulting miss distance and collision probability.

During the development of the tool the *Flying Laptop*'s aerodynamic properties were determined making use of the ADBSat software. Look-up tables specifying the ballistic coefficient in the different attitudes depending on solar and geomagnetic activity could, hence, be created. These are used in the developed tool to calculate in-track separation distances relative to a trajectory specified in a collision warning. For this, atmospheric density models are implemented to estimate an average density the *Flying Laptop* encounters on its trajectory, which consider current and/or predicted space weather data. Further constraints regarding charging phases during the manoeuvre can be considered and uncertainties in the various parameters that are used as input to the tool can be accounted for, as well. At this point, the tool relies solely on CDM data and (publicly) available TLEs, which makes it simple to use. No further complex orbit determination and propagation processes are required to estimate the effect of a manoeuvre. The tool's predicted separation between two objects of different ballistic coefficients was further compared to a numerical propagation. It was found that neglecting orbital eccentricity and further perturbing forces in the derivation of the analytic equation leads to only small errors in the separation of the two trajectories.

Afterwards, further analyses were performed with the developed tool. The evaluation of historical position data of the *Flying Laptop* proved the general effectiveness of aerodynamic manoeuvres. While separation distances could be detected, the sgp4-propagation of reference trajectories does not provide sufficient accuracy to assess the precision of the tool. Here, further analyses with more refined techniques are necessary.

An analysis of the previously received warnings for close encounters of the *Flying Laptop* indicated that, in general, the warnings are issued early enough for the satellite operators to plan and implement a collision avoidance manoeuvre. The use of aerodynamic manoeuvres for collision avoidance was found to be feasible for the *Flying Laptop* for moderate and high solar and geomagnetic activity levels, whereas achievable separation distances for low activity were insufficient. Implementing charging phases of reasonable duration were

shown to not hinder the applicability of aforementioned manoeuvres. Additionally, an exemplary conjunction was studied to evaluate the influence of parameter uncertainties. For this example it was concluded that while the uncertainties may lead to slightly higher collision probabilities than when not accounting for them, the overall collision probability can be decreased with a manoeuvre. In general though, similar analyses must be performed individually for the assessment of future close encounters. Lastly, possible short-term and long-term manoeuvre strategies were presented based on the predicted conjunction geometry. While for short warning times a manoeuvre which monotonously increases the miss distance should be performed, for long-term manoeuvres higher miss distances might be achieved through opposite manoeuvres. So far however, this lacks proper in-orbit verification and it is generally recommended to perform conservative manoeuvres, which were shown to positively affect the collision risk.

9.2 Outlook

Probably the most important aspect of future research concerning the developed tool is further investigation of its prediction accuracy. The evaluation of position data gathered with a sophisticated orbit determination process could allow for the analysis of the effects of attitude changes on the trajectory. Similarly, the usage of the tool in a close encounter and the implementation of a simulated manoeuvre remains to be realised in the future. By looking at the predicted position at the time of closest encounter and GPS position data after performing a manoeuvre, further insights into the tool's performance can be gained. Possible error sources, besides the described assumptions of the analytic equation, might include potential discrepancies between the determined and real-world ballistic coefficient of the satellite. Further, the effect of potential manoeuvres on encounters which might happen multiples of the respective orbital periods before or after the analysed encounter should be studied intensively. This is especially important for encounters with objects in orbits with similar periods to that of the *Flying Laptop*.

A next step for the tool development might be the consideration of different mission timelines. As has been showed, certain phases in which the satellite's attitude differs from the minimum or maximum drag configuration, respectively, can be implemented as well given they are short relative to the manoeuvre duration. This could allow for the inclusion of certain Earth observation or other pointing requirements during an avoidance manoeuvre, granting more valuable payload mission time while still achieving a desired miss distance. Further, solar radiation pressure plays a non-negligible role in the orbital regimes of the *Flying Laptop*. To consider its influence in the respective estimations of a miss distance and making use of the perturbing force as a means of control could enhance the manoeuvring abilities. Additionally, the fundamental analytic equation might be further refined. So far, only one element, i.e., the mean anomaly, is considered. By employing Gaussian variational equations, for example, the effects on other orbital elements could be considered as well.

Although the tool was developed for the *Flying Laptop*, it is possible to use it for any satellite given that their aerodynamic properties are known or can be realistically modelled. The IRS plans further missions of small satellites and Cubesats in LEO, e.g., EIVE [57] and SOURCE [58], and it can be assumed that they will face frequent collision warnings just like the *Flying Laptop*. These missions but also others could potentially benefit of simulation capabilities for collision avoidance using aerodynamic drag.

A Exemplary Conjunction Data Message

The following Conjunction Data Message was issued by the JSpOC for a close encounter between the *Flying Laptop* and a OneWeb satellite on April 7, 2022.

```

-----
DLR                                                    German Space Operations Center
CDM Summary generated: 2022/04/06 04:12
-----

CCSDS_CDM_VERSION : 1.0
CREATION_DATE [UTC]: 2022/04/05 18:29:12
ORIGINATOR : JSpOC
MESSAGE_FOR : FLYING LAPTOP
MESSAGE_ID : 000042831_conj_000050503_2022097221149_09518360066890

TCA [UTC]: 2022/04/07 22:11:49.128
MISS_DISTANCE [m]: 761.0
RELATIVE_SPEED [m/s]: 1437.0
REL_POSITION_R [m]: 0.1
REL_POSITION_T [m]: -758.3
REL_POSITION_N [m]: -72.7
COLLISION_PROB : 1.23E-03
COLLISION_PROB_METHOD: FOSTER-1992

OBJECT : OBJECT1                                OBJECT2
-----
OBJECT_DESIGNATOR : 42831                                50503
OBJECT_NAME : FLYING LAPTOP                                ONEWEB-0440
ITN_DESIGNATOR : 2017-042G                                2021-132AL
OBJECT_TYPE : PAYLOAD                                PAYLOAD
OPERATOR_ORGANIZATION: University of Stuttgart                                OneWeb
EPHEMERIS_NAME : NONE                                NONE
MANEUVERABLE : NO                                YES
REF_FRAME : ITRF                                ITRF
GRAVITY_MODEL : EGM-96: 36D 36O                                EGM-96: 36D 36O
ATMOSPHERIC_MODEL : JBH09                                JBH09
N_BODY_PERTURBATIONS : MOON,SUN                                MOON,SUN
SOLAR_RAD_PRESSURE : YES                                NO
EARTH_TIDES : YES                                YES
INTRACK_THRUST : NO                                NO
TIME_LASTOB_STA [UTC]: 2022/04/04 18:29:12.075                                2022/04/04 18:29:12.702
TIME_LASTOB_END [UTC]: 2022/04/05 18:29:12.075                                2022/04/05 18:29:12.702
REC_OD_SPAN [d]: 3.480                                2.470
ACTUAL_OD_SPAN [d]: 3.480                                2.470
OBS_AVAILABLE : 568                                82
OBS_USED : 566                                81
RESIDUALS_ACCEPTED[%]: 99.300                                97.800
WEIGHTED_RMS : 1.297                                1.231
AREA_PC [m**2]: 0.622                                1.674
AREA_DRG [m**2]: 0.000                                0.000
AREA_SRP [m**2]: 0.000                                0.000
MASS [kg]: 0.000                                0.000
CD_A/M [m**2/kg]: 0.018                                0.028
CR_A/M [m**2/kg]: 0.016                                0.000
THRUST_ACC [m/s**2]: 0.000                                0.000
SEDR [W/kg]: 4.656E-04                                6.922E-04
X [km]: 5661.243828                                5661.028981
Y [km]: -3250.769679                                -3250.608598
Z [km]: 2441.373136                                2442.086013
X_DOT [km/s]: 1.519143                                2.262395
Y_DOT [km/s]: -2.625918                                -1.396497
Z_DOT [km/s]: -7.017917                                -7.071076

APOGEE [km]: 602.2                                605.5
PERIGEE [km]: 591.6                                583.8
ECCENTRICITY : 0.00076                                0.00156
INCLINATION [deg]: 97.4                                87.2

RTN_1SIGMA [m]: 6.6 882.1 3.8 21.9 2196.6 18.4

RTN_COVARIANCE [m**2]: 4.416E+01 4.815E+02
-4.677E+03 7.782E+05 -2.376E+04 4.825E+06
-2.611E-01 1.340E+02 1.453E+01 -8.856E-01 3.523E+03 3.387E+02

```

Figure A.1 – CDM 000042831_conj_000050503_2022097221149_09518360066890

B Aerodynamic analysis results of the *Flying Laptop* in nadir-pointing

Fig. B.1 shows the ballistic coefficient of the *Flying Laptop* in nadir-pointing attitude for different solar and geomagnetic activity as determined with ADBSat.

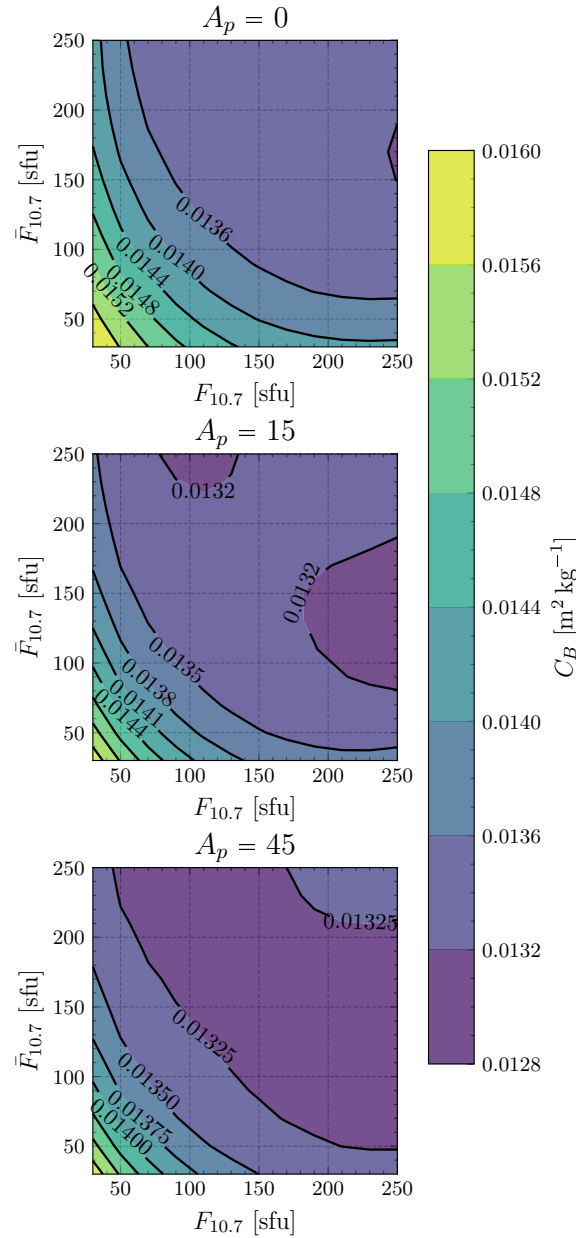


Figure B.1 – Ballistic coefficient of the *Flying Laptop* in nadir-pointing attitude.

C Digital appendix

The code for the developed tool is provided digitally as a `python` package. It may be obtained at:

- https://git.buggy.irs.uni-stuttgart.de/fabrizio.turco/CA-Aerodynamic_Drag
- https://github.com/fabrizioturco/CAM_aerodynamic_drag

Bibliography

- [1] Kessler, D. J. and Cour-Palais, B. G. “Collision Frequency of Artificial Satellites: The Creation of a Debris Belt”. In: *Journal of Geophysical Research* 83.A6 (1978), pp. 2637–2646. DOI: <http://dx.doi.org/10.2514/5.9781600865459.0707.0736>.
- [2] NASA Orbital Debris Program Office. “Orbital Debris Quarterly News September 1996”. In: *Orbital Debris Quarterly News*. Vol. 1. 2. 1996. URL: <https://orbitaldebris.jsc.nasa.gov/quarterly-news/pdfs/odqnv1i2.pdf>.
- [3] NASA Orbital Debris Program Office. “Orbital Debris Quarterly News April 2007”. In: *Orbital Debris Quarterly News*. Vol. 11. 2. 2007. URL: <https://orbitaldebris.jsc.nasa.gov/quarterly-news/pdfs/odqnv11i2.pdf>.
- [4] NASA Orbital Debris Program Office. “Orbital Debris Quarterly News April 2009”. In: *Orbital Debris Quarterly News*. Vol. 13. 2. 2009. URL: <https://orbitaldebris.jsc.nasa.gov/quarterly-news/pdfs/odqnv13i2.pdf>.
- [5] Kessler, D. J. “Collisional cascading: The limits of population growth in low earth orbit”. In: *Advances in Space Research* 11.12 (1991), pp. 63–66. ISSN: 02731177. DOI: [http://dx.doi.org/10.1016/0273-1177\(91\)90543-S](http://dx.doi.org/10.1016/0273-1177(91)90543-S).
- [6] Kessler, D. J. *Critical Density of Spacecraft in Low Earth Orbit: Using Fragmentation Data to Evaluate the Stability of the Orbital Debris Environment*. Houston, Texas, USA.
- [7] NASA Orbital Debris Program Office. “Orbital Debris Quarterly News June 2022”. In: *Orbital Debris Quarterly News*. Vol. 26. 2. 2022. URL: <https://orbitaldebris.jsc.nasa.gov/quarterly-news/pdfs/odqnv26i2.pdf>.
- [8] Eickhoff, J. *The FLP Microsatellite Platform: Flight Operations Manual*. Springer International Publishing, 2016. ISBN: 978-3-319-23502-8. DOI: [10.1007/978-3-319-23503-5](https://doi.org/10.1007/978-3-319-23503-5).
- [9] Institute of Space Systems, University of Stuttgart. *Project page: Flying Laptop: Nutzlasten*. URL: <https://www.irs.uni-stuttgart.de/forschung/satellitentechnik/kleinsatellitenprogramm/flying-laptop/nutzlast> (visited on August 25, 2022).
- [10] Institute of Space Systems, University of Stuttgart. *Project page: Flying Laptop*. URL: <https://www.irs.uni-stuttgart.de/forschung/satellitentechnik/~kleinsatellitenprogramm/flying-laptop> (visited on August 25, 2022).
- [11] Vallado, D. and McClain, W. *Fundamentals of Astrodynamics and Applications*. 4th ed. Hawthorne, CA, USA: Microcosm Press, 2013. ISBN: 978-1881883180.

- [12] Capitaine, N., Wallace, P. T., and Chapront, J. “Expressions for IAU 2000 precession quantities”. In: *Astronomy & Astrophysics* 412.2 (2003), pp. 567–586. ISSN: 0004-6361. DOI: <http://dx.doi.org/10.1051/0004-6361:20031539>.
- [13] Southard, J. *Introduction to Fluid Motions and Sediment Transport*. LibreTexts, 2022. URL: [https://geo.libretexts.org/Bookshelves/Sedimentology/Book%3A_Introduction_to_Fluid_Motions_and_Sediment_Transport_\(Southard\)](https://geo.libretexts.org/Bookshelves/Sedimentology/Book%3A_Introduction_to_Fluid_Motions_and_Sediment_Transport_(Southard)).
- [14] National Geospatial-Intelligence Agency, 2014. *Department of Defense World Geodetic System 1984: Its Definition and Relationships with Local Geodetic Systems: Standardization Document*. URL: <https://nsgreg.nga.mil/doc/view?i=4085&month=9&day=16&year=2022>.
- [15] The Consultative Committee for Space Data Systems, 2013. *CCSDS 508.0-B-1: Conjunction Data Message: Recommended Standard*. URL: <https://public.ccsds.org/Pubs/508x0b1e2c2.pdf>.
- [16] Messerschmid, E. and Fasoulas, S. *Raumfahrtsysteme*. 5th ed. Berlin, Heidelberg: Springer, 2017. ISBN: 978-3-662-49637-4. DOI: <http://dx.doi.org/10.1007/978-3-662-49638-1>.
- [17] Vallado, D. A. and Cefola, P. J. “Two-Line Element Sets - Practice and Use”. In: *63rd International Astronautical Congress*. Naples, Italy, 2012.
- [18] Doornbos, E. “Thermospheric Density and Wind Determination from Satellite Dynamics”. PhD thesis. Delft, Netherlands: Technische Universiteit Delft, 2011.
- [19] Traub, C. et al. “On the exploitation of differential aerodynamic lift and drag as a means to control satellite formation flight”. In: *CEAS Space Journal* 12.15–32 (2020).
- [20] Traub, C., Fasoulas, S., and Herdrich, G. H. *A planning tool for optimal three-dimensional formation flight maneuvers of satellites in VLEO using aerodynamic lift and drag via yaw angle deviations*. March 15, 2022. URL: <https://arxiv.org/pdf/2203.07899>.
- [21] Omar, S. *Using Differential Aerodynamic Forces for CubeSat Orbit Control*. Logan, Utah, United States, August 10–15, 2013.
- [22] Livadiotti, S. et al. “A Review of Gas-Surface Interaction Models for Orbital Aerodynamics Applications”. In: *Progress in Aerospace Sciences* 119.1 (2020). ISSN: 03760421. DOI: <http://dx.doi.org/10.1016/j.paerosci.2020.100675>.
- [23] Sinpetru, L. A. et al. “ADBSat: Methodology of a novel panel method tool for aerodynamic analysis of satellites”. In: *Computer Physics Communications* 275 (2022). ISSN: 0010-4655. DOI: <http://dx.doi.org/10.1016/j.cpc.2022.108326>.
- [24] Moe, K. and Moe, M. M. “Gas-surface interactions and satellite drag coefficients”. In: *Planetary and Space Science* 53.8 (2005), pp. 793–801. ISSN: 00320633. DOI: <http://dx.doi.org/10.1016/j.pss.2005.03.005>.

- [25] Sentman, L. H. *Free molecule flow theory and its application to the determination of aerodynamic forces*. Lockheed Aircraft Corporation, 1961.
- [26] Sinpetru, L. A. et al. “ADBSat: Verification and validation of a novel panel method for quick aerodynamic analysis of satellites”. In: *Computer Physics Communications* 275 (2022). ISSN: 0010-4655. DOI: <http://dx.doi.org/10.1016/j.cpc.2022.108327>.
- [27] National Oceanic and Atmospheric Administration, National Aeronautics and Space Administration, and United States Air Force. *U.S. Standard Atmosphere, 1976*. Washington, D.C., 1976.
- [28] Picone, J. M. et al. “NRLMSISE-00 empirical model of the atmosphere: Statistical comparisons and scientific issues”. In: *Journal of Geophysical Research: Space Physics* 107.A12 (2002), pp. S15-1-S15-16. ISSN: 0148-0227. DOI: <http://dx.doi.org/10.1029/2002JA009430>.
- [29] Bowman, B. et al. “A New Empirical Thermospheric Density Model JB2008 Using New Solar and Geomagnetic Indices”. In: *AIAA/AAS Astrodynamics Specialist Conference and Exhibit*. Vol. AIAA 2008-6438. Reston, Virginia: American Institute of Aeronautics and Astronautics, 2008. ISBN: 978-1-62410-001-7. DOI: <http://dx.doi.org/10.2514/6.2008-6438>.
- [30] International Organization for Standardization, 2022. *ISO 14222:2022(E): Space environment (natural and artificial) - Earth's atmosphere from ground level upward: International Standard*.
- [31] NASA. *NASA Spacecraft Conjunction Assessment and Collision Avoidance Best Practices Handbook*. 2020. URL: https://nodis3.gsfc.nasa.gov/OCE_docs/OCE_50.pdf.
- [32] 18th Space Control Squadron. *Spaceflight Safety Handbook for Satellite Operators: 18 SPCS Processes for On-Orbit Conjunction Assessment & Collision Avoidance*. August 2020. URL: https://www.space-track.org/documents/Spaceflight_Safety_Handbook_for_Operators.pdf.
- [33] Kiehling, R., Aida, S., and Kirschner, M. “Collision Avoidance Operations at DLR GSOC”. In: SpaceOps Workshop. Deutsches Zentrum für Luft- und Raumfahrt (DLR), German Space Operations Center (GSOC), June 14–16, 2011. URL: <https://core.ac.uk/download/pdf/11150013.pdf>.
- [34] Foster, J. L. *A Parametric Analysis of Orbital Debris Collision Probability and Maneuver Rate for Space Vehicles Mission Operations*. Houston, Texas, USA: National Aeronautics and Space Administration, 1992.
- [35] Klinkrad, H. *Space Debris: Models and Risk Analysis*. Springer-Praxis Books in Astronautical Engineering. Berlin et al.: Springer-Verlag and Praxis Publishing, 2006. ISBN: 3-540-25448-X.
- [36] Alfano, S. “A Numerical Implementation of Spherical Object Collision Probability”. In: *The Journal of the Astronautical Sciences* 53.1 (2005), pp. 103–109. ISSN: 0021-9142. DOI: <http://dx.doi.org/10.1007/BF03546397>.

- [37] Joint Space Operations Center. *Probability of Collision in the Joint Space Operations Center*. 2016. URL: https://www.space-track.org/documents/How_the_JSpOC_Calculates_Probability_of_Collision.pdf.
- [38] Astrodynamics Innovation Committee: Working Group on Covariance Realism. *Covariance and Uncertainty Realism in Space Surveillance and Tracking*. Ed. by Aubrey B. Poore, Jeffrey M. Aristoff, and Joshua T. Horwood. 2016. URL: <https://apps.dtic.mil/sti/pdfs/AD1020892.pdf>.
- [39] Chen, L. et al. *Orbital Data Applications for Space Objects*. Singapore: Springer Singapore, 2017. ISBN: 978-981-10-2962-2. DOI: <http://dx.doi.org/10.1007/978-981-10-2963-9>.
- [40] Alfano, S. “Relating Position Uncertainty to Maximum Conjunction Probability”. In: *The Journal of the Astronautical Sciences* 53.2 (2005), pp. 193–205. ISSN: 0021-9142. DOI: <http://dx.doi.org/10.1007/BF03546350>.
- [41] Leleux, D. et al. “Probability-Based Space Shuttle Collision Avoidance”. In: *SpaceOps 2002 Conference*. Reston, Virginia, USA: American Institute of Aeronautics and Astronautics, 2002. DOI: <http://dx.doi.org/10.2514/6.2002-T3-50>.
- [42] Bombardelli, C. “Analytical formulation of impulsive collision avoidance dynamics”. In: *Celestial Mechanics and Dynamical Astronomy* 118.2 (2014), pp. 99–114. ISSN: 0923-2958. DOI: <http://dx.doi.org/10.1007/s10569-013-9526-3>.
- [43] Omar, S. R. and Bevilacqua, R. “Spacecraft Collision Avoidance Using Aerodynamic Drag”. In: *Journal of Guidance, Control, and Dynamics* 43.3 (2020), pp. 567–573. DOI: <http://dx.doi.org/10.2514/1.G004518>.
- [44] Mishne, D. and Edlerman, E. “Collision-Avoidance Maneuver of Satellites Using Drag and Solar Radiation Pressure”. In: *Journal of Guidance, Control, and Dynamics* 40.5 (2017), pp. 1191–1205. DOI: <http://dx.doi.org/10.2514/1.G002376>.
- [45] David Mishne. “Collision Avoidance Maneuver of Propulsionless Satellite, using Solar Radiation Pressure”. In: *The 56th Israel Annual Conference on Aerospace Sciences*. Tel Aviv and Haifa, Israel, 2016.
- [46] Whiteside, D. T. “Henry Briggs: The Binomial Theorem Anticipated”. In: *The Mathematical Gazette* 45.351 (1961).
- [47] NASA. *Conjunction Assessment Risk Analysis (CARA) software*. URL: https://github.com/nasa/CARA_Analysis_Tools (visited on September 17, 2022).
- [48] Traub, C., Herdrich, G. H., and Fasoulas, S. “Influence of energy accommodation on a robust spacecraft rendezvous maneuver using differential aerodynamic forces”. In: *CEAS Space Journal* 12.1 (2020), pp. 43–63. ISSN: 1868-2502. DOI: <http://dx.doi.org/10.1007/s12567-019-00258-8>.
- [49] Pilinski, M. D. “Dynamic Gas-Surface Interaction Modeling for Satellite Aerodynamic Computations”. PhD thesis. University of Colorado, 2011.

-
- [50] Li, C. *pyatmos: Python package*. 2021. URL: <https://github.com/lcx366/ATMOS> (visited on September 12, 2022).
 - [51] Rhodes, B. *skyfield: Python package*. 2022. URL: <https://github.com/skyfielders/python-skyfield> (visited on September 12, 2022).
 - [52] Space Environment Technologies. *Advanced Space Weather Products and Services*. URL: <https://sol.spacenvironment.net> (visited on September 12, 2022).
 - [53] Papula, L. *Mathematik für Ingenieure und Naturwissenschaftler 3: Vektoranalysis, Wahrscheinlichkeitsrechnung, Mathematische Statistik, Fehler- und Ausgleichsrechnung*. 6th ed. Vol. 3. Vieweg+Teubner. ISBN: 978-3-8348-1227-8.
 - [54] ASTOS Solutions GmbH. *ASTOS: Analysis, Simulation and Trajectory Optimization Software for Space Applications*. URL: <https://www.astos.de/products/astos> (visited on September 21, 2022).
 - [55] Hathaway, D. H. “The Solar Cycle”. In: *Living reviews in solar physics* 12 (2015), p. 4. ISSN: 1614-4961. DOI: <http://dx.doi.org/10.1007/lrsp-2015-4>.
 - [56] Space Weather Prediction Center. *Solar Cycle 25 Forecast Update*. 2019. URL: <https://www.swpc.noaa.gov/news/solar-cycle-25-forecast-update> (visited on September 24, 2022).
 - [57] Institute of Robust Power Semiconductor Systems, University of Stuttgart. *Project page: EIVE (Exploratory In-Orbit Verification of an E/W-Band Satellite Communication Link)*. URL: <https://www.ilh.uni-stuttgart.de/en/research/mmw/EIVE/> (visited on September 27, 2022).
 - [58] Institute of Space Systems, University of Stuttgart. *Project page: SOURCE (Stuttgart Operated University Research Cubesat for Evaluation and Education)*. URL: <https://www.irs.uni-stuttgart.de/forschung/satellitentechnik/kleinsatellitenprogramm/source/set> (visited on September 27, 2022).